Tesis Doctoral

Estudio electroquímico y espectroelectroquímico de componentes de sales orgánicas conductoras.

Formación de películas delgadas organizadas de TCNQ, TTF y Viologenos.

Lorenzo Gómez Camacho

Departamento de Química Física y

Termodinámica Aplicada.

Universidad de Córdoba.

TITULO:Estudio Electróquímico de componentes de sales orgánicas conductoras. Formación de películas delgadas organizadas de TCNQ, TTF y viológenos

AUTOR: *Lorenzo Gómez Camacho*

ÍNDICE:

OBJETIVOS

Estudio electroquímico y espectroelectroquímico de componentes de sales orgánicas conductoras.

5

El trabajo presentado en esta tesis pretende profundizar en el estudio de determinados procesos electroquímicos relacionados con la formación, por electrocristalización, de ciertos materiales orgánicos con diversas propiedades conductoras. A tal fin, los objetivos globales que se han marcado son:

a) Obtención de estos materiales a partir de compuestos tales como el TCNQ, TTF y los viológenos, cuya principal importancia radica en que son potencialmente útiles para el desarrollo y formación de diversas sales orgánicas conductoras, así como por su empleo como mediadores electroquímicos.

b) Aportar nuevos conocimientos teóricos y experimentales que ayuden a explicar su comportamiento electroquímico, facilitando su posterior empleo como especies inmovilizadas sobre la superficie del electrodo.

c) Ahondar en el estudio de los procesos de nucleación y crecimiento, bidimensional y tridimensional, mediante modelos previamente descritos en la bibliografía, o bien mediante el desarrollo de otros nuevos.

d) Esclarecer los mecanismos subyacentes a estos procesos, mediante técnicas como la espectroelectroquímica UV-Vis, que suministra valiosa información acerca de la naturaleza de los procesos que ocurren sobre la superficie del electrodo, y sobre la aparición de posibles compuestos

intermedios que pueden formar parte del mecanismo.

El desarrollo del trabajo, incluyendo los avances experimentales en la técnica de espectroelectroquímica in-situ de reflexión sobre electrodos sólidos en disolución, se ha realizado dentro de la línea de investigación "Sales Orgánicas Conductoras. Formación y empleo como material electródico", la cual está apoyada en los proyectos CTQ2004-01677 y CTQ2007-60387 del Ministerio de Educación y Ciencia de España.

CAPÍTULO I.

INTRODUCCIÓN

1.1 Materiales orgánicos conductores

Hasta 1954, los compuestos orgánicos habían sido considerados tradicionalmente como aislantes. Sin embargo, en este año es descubierto un complejo de bromo-perileno con comportamiento de semiconductor inorgánico, pasando a ser el primer compuesto denominado como "metal orgánico". Este descubrimiento marca el punto de partida del estudio de los compuestos orgánicos conductores. La intensa actividad investigadora que ha venido siendo desarrollada en el campo de los "metales orgánicos" refleja el gran interés de estos materiales, lo que se ve plasmado en el gran número de publicaciones relacionadas con este nuevo campo [1-6]. De esta manera, las interesantes propiedades conductoras y ópticas que presenta esta nueva generación de materiales ha permitido su empleo en numerosas aplicaciones como componentes útiles para el desarrollo de baterías recargables, sensores (narices y lenguas electrónicas), dispositivos electrónicos (diodos, transistores...) o células fotovoltaicas [7-11], dispositivos electrocrómicos, diodos emisores de luz (OLEDs), dispositivos de óptica no lineal (NLO), para almacenamiento óptico de datos con alta densidad, holografía y limitadores ópticos [12], o en el área de los músculos artificiales [13,14], debido a sus propiedades electroquimiomecánicas. Además, el elevado desarrollo tecnológico de algunas de estas aplicaciones se refleja en su presencia en el mercado.

Clasificación.

En general, un sólido conductor orgánico requiere de la existencia de moléculas cargadas y de deslocalización de la carga entre las moléculas del sólido. Los denominados "metales orgánicos" se suelen clasificar en cuatro tipos fundamentales: polímeros conjugados, complejos y sales de transferencia de carga, metalomacrociclos y fullerenos.

a) Complejos y sales de transferencia de carga (CTC):

Abarca a los compuestos en los que existe una transferencia de carga de una molécula dadora a una aceptora, de manera que se obtiene un sólido de estructura iónica y con conductividad de tipo metálico. El arquetipo de complejo de transferencia de carga conductor es el que forman el potente aceptor de electrones tetraciano-p-quinodimetano (TCNQ) y el potente dador electrónico tetratiafulvaleno (TTF), que como resultado generan el TTF-TCNQ.
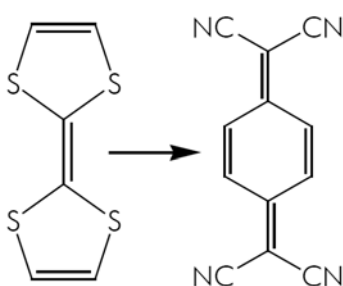
Figura 1.1. Estructura del complejo TTF-TCNQ

Descubierto en 1973, este complejo marcó un hito en el estudio de los "metales orgánicos" [15,16]. Su conductividad, similar a los metales tradicionales, crece al disminuir la temperatura, desde 500 S cm^{-1}, a temperatura ambiente, hasta 10^4 S cm^{-1} a 59 K. Dado que gran parte del presente trabajo tiene como objeto el estudio de las sales orgánicas conductoras, su descripción será tratada más ampliamente en posteriores apartados.

b) <u>Polímeros conjugados</u>:

En paralelo al estudio de los complejos de transferencia de carga, el estudio de los polímeros conductores fue desarrollándose a partir de cadenas poliméricas, de manera que se pueda disponer de unos materiales con la conductividad de un metal o semiconductor y las ventajosas propiedades mecánicas de los plásticos [17], a lo que se añade la versatilidad que proporciona la síntesis química sobre este tipo de materiales.

Estos polímeros son sistemas lineales ordenados, constituidos por monómeros que poseen electrones π, de manera que se obtenga una cadena conjugada a lo largo de toda su extensión. En sí misma, una cadena de estas características no es conductora; sin embargo, el dopado en las cadenas a través de la inyección de cargas positivas (huecos), o negativas (electrones) las transforma en conductoras. El primer compuesto sintetizado de estas características fue el poliacetileno dopado (Figura 1.2), al cual le han seguido

otros con mejores propiedades, como el polifenileno, polipirrol, polifurano o politiofeno dando lugar a conductividades en estado dopado del orden de 10^2 - 10^3 S cm^{-1}). [18]
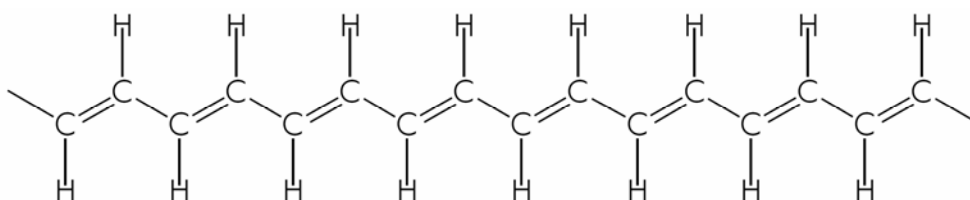
Figura 1.2. Estructura del trans-poli-acetileno

Esta deslocalización es la base tanto de conductores poliméricos como de superconductores orgánicos. El primer caso de superconductividad en compuestos orgánicos fue descrito en 1980 por Jérôme y col. para sales de tetrametiltetraselenofulvaleno (TMTSF), [(TMTSF)$_2$PF$_6$], a una temperatura de transición de 0.9 K a 12 kbar de presión [19]. Sin embargo, actualmente se conocen gran número de superconductores orgánicos con temperaturas de transición más elevadas a presión atmosférica.

c) *Fullerenos*:

Considerado material orgánico por ser una forma alotrópica del Carbono, son moléculas discretas formadas por un número definido de átomos. Una de ellas, el C$_{60}$ (Figura 1.3), constituida por 60 átomos de carbono situados sobre la superficie de una esfera, tiene cada átomo de C unido a tres vecinos mediante un enlace de tipo sp^2, lo que provoca la presencia de una nube

electrónica con electrón despareado de tipo π. La molécula de C_{60} en estado neutro se presenta como a un sólido molecular aislante con estructura cristalina. Sin embargo, al doparlo con metales alcalinos o alcalinotérreos obtenemos una estequiometría tipo M_3C_{60} (con M_3= K_3, Rb_3, Cs_2Rb, etc) [20], provocando el solapamiento entre moléculas vecinas cercanas la aparición de una banda de conducción, que hace que posean conductividad tridimensional. Dentro de esta nueva familia de conductores moleculares, las sales de fullereno C60 presentan superconductividad [21], con temperaturas de transición en el intervalo de 10 a 45 K. [22,23]
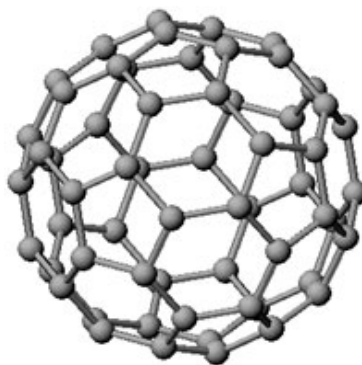
Figura 1.3. Estructura del fullereno C_{60}

d) <u>Metalomacrociclos:</u>

Conectando sistemas macrocíclicos, tales como ftalocianinas o tetrabenzoporfirinas, como ligandos de un metal de transición capaz de hexacoordinarse (Fe, Co, Cr o Ru) se obtienen complejos metálicos poliméricos que, tras el dopado con un aceptor electrónico, se transforman en polímeros conductores cuyas propiedades dependen de la naturaleza del

metalomacrociclo, del átomo metálico central y del ligando puente [24,25]. Se presentan como sólidos cristalinos formados por columnas en las que las moléculas se disponen paralelamente a lo largo del eje de apilamiento. Al solapar los orbitales de tipo π ocurre una deslocalización de los electrones a lo largo del apilamiento, obteniéndose materiales conductores quasi-unidimensionales.

1.2. Complejos de transferencia de carga (CTC)

Las propiedades eléctricas de estos compuestos orgánicos, dependiendo de los componentes que las formen, tienen un carácter muy variable, desde un aislante como el complejo pireno-TCNQ [26-27], el semiconductor del morfolinio-TCNQ [26-27], hasta el carácter conductor del N-Metilfenacinio -TCNQ [28].

En primer lugar, para obtener un compuesto con conductividad de tipo metálico es indispensable que la estructura cristalina consista en una ordenación de apilamientos segregados, formados por las moléculas dadoras y aceptoras, que componen el complejo o sal de transferencia. Como resultado de la transferencia de carga se forma un cristal de tipo iónico, en el que los aniones, los cationes, o ambos, son grupos químicos con estructura compleja.

La transferencia de carga entre las moléculas dadoras y aceptoras en el sólido ha de ser parcial, de manera que el resultado sea un compuesto de valencia mixta, en el que haya coexistencia entre moléculas cargadas y no

cargadas, para lo que es necesario que estas moléculas sean capaces de formar radicales estables.

Para conseguir conductividades elevadas es también un requisito fundamental que haya deslocalización electrónica, que permita la movilidad de los electrones π desapareados a través de los apilamientos. Para que esto ocurra, es necesario que los que los orbitales HOMO de las moléculas dadoras interaccionen por una parte, y los orbitales LUMO de las moléculas aceptoras lo hagan por otra, dando lugar a la formación de bandas electrónicas que permitan la deslocalización de los electrones y, en consecuencia, se pueda hablar de que las nubes electrónicas π están solapadas.
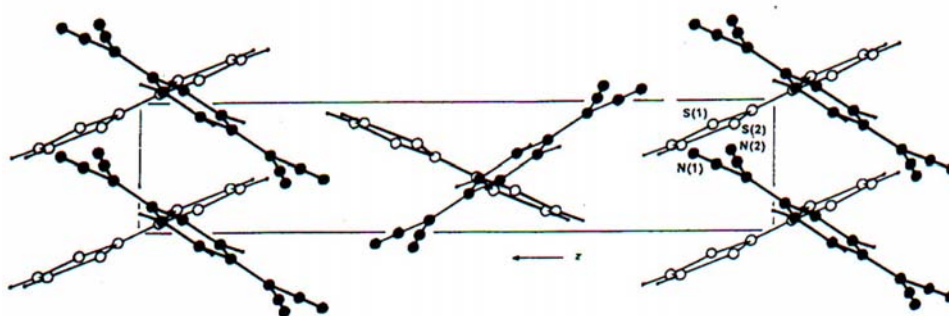
Figura 1.4.- Proyección de la estructura cristalina del complejo TTF-TCNQ a lo largo del eje x [20]. Los apilamientos separados de TTF y TCNQ se disponen a lo largo del eje y. Las moléculas de TCNQ (círculos negros) están en primer plano.

En el caso concreto del complejo TCNQ-TTF, puede observarse en la Figura 1.4 la estructura en forma de apilamientos paralelos separados de las moléculas de ambos componentes, dador y aceptor, situándose las moléculas

de TCNQ en primer plano (círculos negros) y las moléculas de TTF en un segundo plano [29]. Aunque la estequiometría dador/aceptor es 1:1, la transferencia de carga entre TTF y TCNQ no es completa (0.59 e⁻ por molécula), formándose, por tanto, el necesario complejo de valencia mixta.

1.2.1 Dadores de electrones π.

Los compuestos orgánicos que forman complejos de transferencia de carga, conductores y superconductores, son en su mayoría moléculas conjugadas planas, dadoras o aceptoras de electrones π. Ya sean dadoras o aceptoras, una característica común a ambos es la deslocalización electrónica por encima y por debajo del plano medio de la molécula, de forma que, en la estructura cristalina, las nubes π de moléculas contiguas solapen y proporcionen una vía para la movilidad de los electrones desapareados (electrones de conducción) a través de los apilamientos.

a) Tetratiafulvaleno (TTF)

Hay gran variedad de moléculas dadoras de electrones, aunque la mayoría de compuestos presentan una estructura análoga al TTF. Una propiedad fundamental, que le hace un candidato idóneo para formar un CTC, es su bajo potencial de oxidación. Así, se favorece la formación de su radical estable, estabilizada por la formación de una forma canónica aromática (de Hückel) y, por tanto, la transferencia de carga con el aceptor. Como se puede observar en la Figura 1.5, el TTF neutro presenta una estructura electrónica en

la que cada anillo alberga 7 electrones de tipo π [30,31].
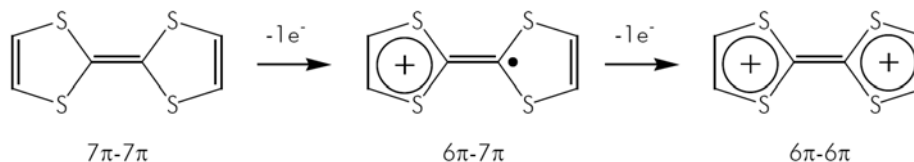
Figura 1.5.- Estabilización de los iones radicales por aromatización de los anillos para el TTF.

La primera oxidación produce un radical-catión TTF$^{+\bullet}$, en el que uno de los anillos pasa a ser aromático, mientras que la segunda oxidación da lugar al dicatión, con dos anillos aromáticos.

Mas ejemplos de moléculas electrodonadoras que dan lugar a complejos de transferencia de carga pueden verse en la Figura 1.6.
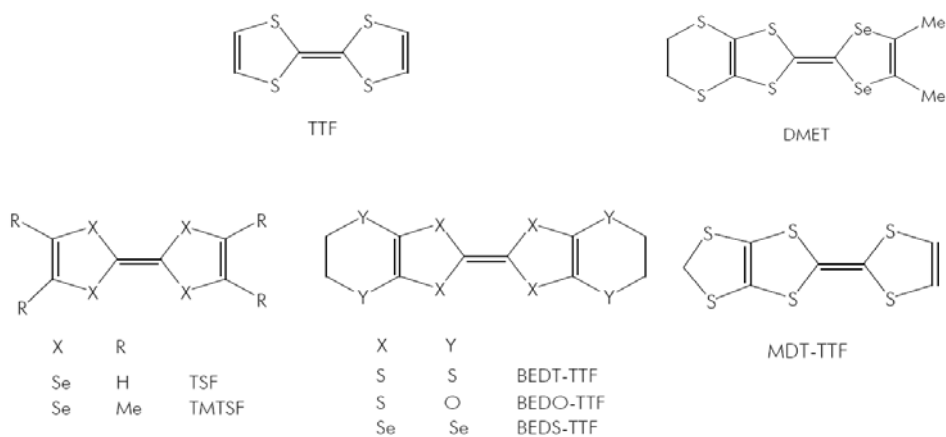
Figura 1.6. Estructura de varios compuestos dadores de electrones π.

b) Viológenos

La 4,4´-Bipiridina y sus alquilderivados, conocidos como "viológenos" constituyen un grupo de compuestos especialmente interesante debido a su alta capacidad redox como mediador, la cual está vinculada a la orientación de esta molécula en estado inmovilizado. Estas moléculas también dan lugar a transiciones de fase bidimensionales sobre electrodos, formando cristales líquidos sobre su superficie [32–35]. En la presente tesis será tratado el comportamiento electroquímico de dos compuestos del grupo de los viológenos, como son la bipiridina y el etilviológeno. Mientras que la primera no tiene ningún sustituyente en los anillos aromáticos de su estructura, el etilviológeno posee dos grupos etilo como sustituyentes en las posiciones en las que se encuentran los átomos de nitrógeno en los anillos aromáticos.

Los viológenos pueden presentar 3 estados diferentes de oxidación, el dicatión, el catión radical y la forma neutra, totalmente reducida. Los primeros estudios electroquímicos corresponden a Van Dam y col. [37-39], encontrando que, en medio acuoso, la reducción de los viológenos transcurre en dos etapas monoelectrónicas, dando la primera lugar al radical catión, de color púrpura, y la segunda al viológeno neutro, que se presenta como un sólido, implicando la reacción de desplazamiento en estado sólido (Figura 1.7.).
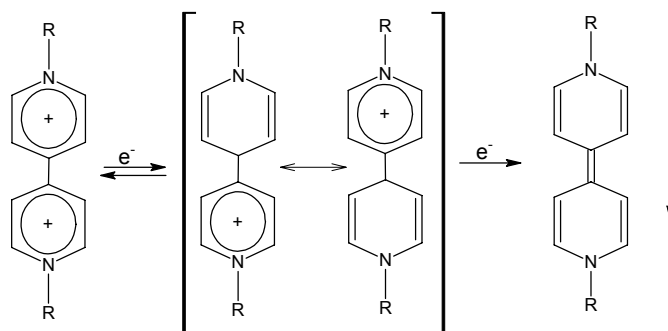
Figura 1.7. Estabilización de los iones radicales de los alquilviológenos por aromatización de los anillos.

La insolubilidad del radical catión es la que permite que éste quede adherido al sustrato. Este efecto hace que pueda ser oxidado de nuevo al estado original [40].

$$\left(RV^{2+}\right)_{disol} \xrightarrow{\ e^-\ } \left(RV^{+\cdot}\right)_{ads} \tag{1.1}$$
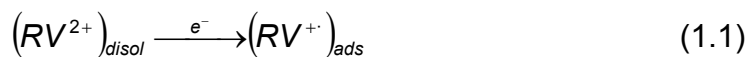
Este proceso superficial se ve influenciado tanto por el tipo de anión presente en disolución, como por el pH, la temperatura o el tipo de sustrato. Debido al interés de esta reacción, en la presente tesis se aplicarán modelos matemáticos capaces de explicar el comportamiento experimental de estos procesos, proporcionando datos de gran interés, como constantes de velocidad, monocapas implicadas, etc…

Su capacidad electrodonadora le hace un candidato idóneo para la formación de complejos de trasferencia de carga. Aunque hasta la fecha se ha conseguido obtener complejos de donador – Viológeno [41], aun no ha sido

sintetizado ninguno con propiedades conductoras adecuadas.

1.2.2 Aceptores de electrones π. TCNQ y Análogos.

A diferencia de lo que ocurre para los dadores, el número de sistemas aceptores que participan en los complejos de transferencia de carga es muy inferior. Los compuestos son, en su mayoría, de estructura análoga al TCNQ. (Figura 1.8).
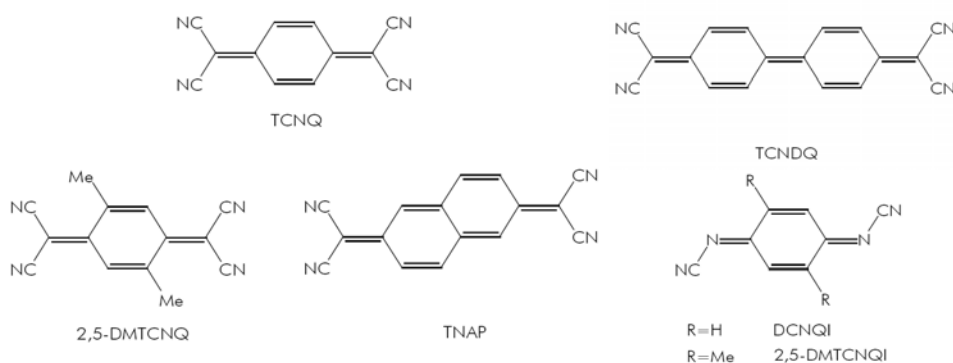
Figura 1.8. Estructura de diversos aceptores de electrones.

Su bajo potencial de reducción favorece una transferencia electrónica desde el dador y la formación de su radical-anion. Como puede verse en la Figura 1.9, la reducción del TCNQ da como resultado la aromatización del anillo central [42].
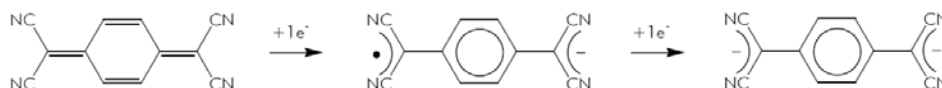
Figura 1.9.- Estabilización de los iones radicales del TCNQ por aromatización de los anillos.

Es fundamental que la afinidad electrónica de los sustituyentes en el esqueleto del TCNQ sea la adecuada, de manera que se estabilice la carga negativa al formar el radical-catión. Si es menor de la necesaria, se obtendrán moléculas con una capacidad aceptora insuficiente, y si es demasiado fuerte, la transferencia de carga será total, con la consiguiente pérdida del complejo de valencia mixta, como puede verse para el tetrafluoro – TCNQ, cuyas sales conductoras tienen baja conductividad, similar a la de aislantes o semiconductores [43].

Además del carácter electroatractor del sustituyente, también es importante su papel en la deslocalización de la carga. Como ejemplo, se puede ver el tetracianoetileno (TCNE), que con características electroatractoras similares al TCNQ da lugar a sales no conductoras.

1.3. Técnicas instrumentales.

La determinación de los mecanismos subyacentes a un proceso de oxidación o de reducción puede realizarse mediante una gran variedad de métodos electroquímicos. A continuación, se procederá a realizar una breve descripción de las diferentes técnicas usadas durante el desarrollo de la tesis, las cuales presentan acentuadas diferencias entre la respuesta de estas técnicas para los procesos con control difusivo, que suelen darse de manera general en disolución, y la respuesta observada en procesos de nucleación y crecimiento. En primer lugar, se comentarán las características generales de las técnicas, y posteriormente, en siguientes apartados, se verán sus aplicaciones concretas para el estudio de los fenómenos de nucleación y crecimiento.

1.3.1. Técnicas electroquímicas.

1.3.1.1. Voltametría Cíclica.

Es el más difundido, y quizás el más directo de todos los métodos electroquímicos utilizados [44]. La voltametría cíclica consiste en la aplicación de un barrido de potencial a la célula electroquímica en condiciones estacionarias, es decir, aquellas en las que, sin agitación, se varía el potencial aplicado desde un valor inicial (E_i) hasta un vértice de potencial (E_V), seguido de un barrido inverso hasta llegar a un potencial final (E_f), el cual es normalmente idéntico al inicial (ver Figura 1.10). La corriente resultante (I) es

monitorizada en función del potencial aplicado (E) para dar la curva i-E, la cual se denomina voltagrama cíclico.
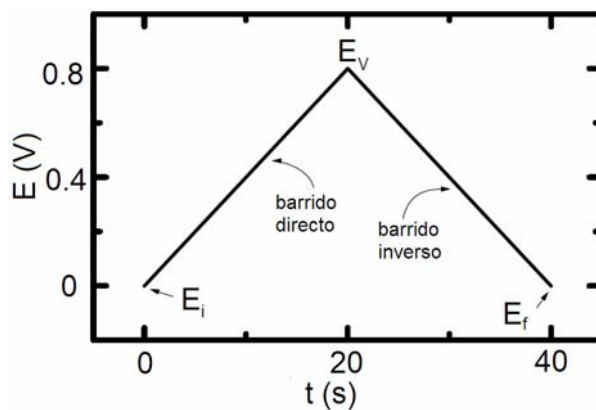
Figura 1.10. Barrido de potencial para voltametría cíclica a 0.08 V/s.

Los procesos voltamétricos en disolución están normalmente regidos por la difusión de las partículas hacia el electrodo. Éstos deben ser claramente diferenciados de los procesos debidos a fenómenos superficiales ocurridos sobre el electrodo. La Figura 1.11 muestra un voltagrama cíclico típico, como es el caso del obtenido para el ferroceno en disolvente acuoso. En este caso, tanto las formas reducida como oxidada son solubles en agua. El valor del potencial inicial es 0.2 V, en el que no tiene lugar ningún proceso electroquímico ni ningún otro tipo de corriente al comenzar el ciclo.
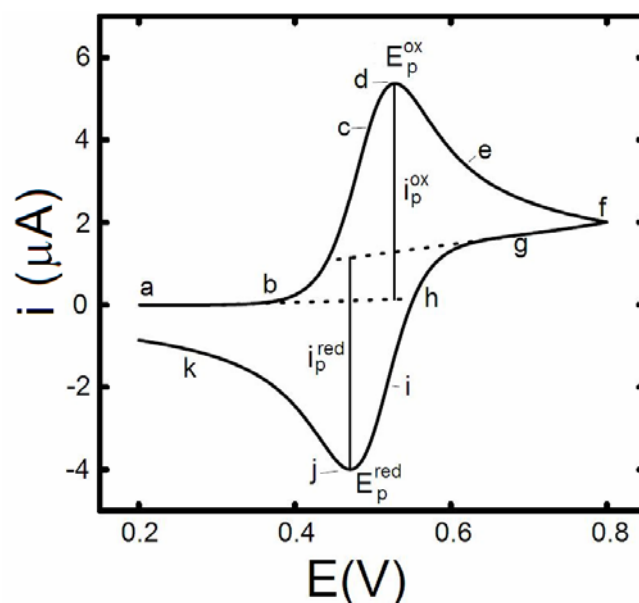
Figura 1.11. Voltagrama de una disolución 0.5 mM de $[Fe(C_5H_5)_2]$ en disolvente orgánico. Área del electrodo = 2.54 mm^2. Velocidad de barrido= 100 mVs^{-1}.

El barrido inicial se realiza hacia potenciales positivos, de manera que el compuesto presente en disolución sea oxidado:

$$Fe^{II}(C_5H_5)_2 \longrightarrow \left[Fe^{III}(C_5H_5)_2\right]^+ + e^-$$ (1.2)

La corriente de oxidación se incrementa rápidamente en el barrido anódico (b hasta d), hasta que la concentración de $Fe^{II}(C_5H_5)_2$ en la superficie del electrodo es significativamente menor. Este hecho da lugar a la aparición de un máximo de corriente en E_p^{ox}. Posteriormente, se produce una bajada (d hasta g), ya que el proceso pasa a estar controlado por la velocidad de difusión del ferroceno desde el seno de la disolución a la superficie del electrodo. Al

invertir la dirección del barrido, la corriente de oxidación todavía fluye, y al llegar al potencial necesario, la especie formada en la oxidación $[Fe^{III}(C_5H_5)_2]^+$, es reducida de nuevo con lo que se observan corrientes debidas a la reducción.

$$\left[Fe^{III}(C_5H_5)_2\right]^+ + e^- \longrightarrow Fe^{II}(C_5H_5)_2 \qquad (1.3)$$
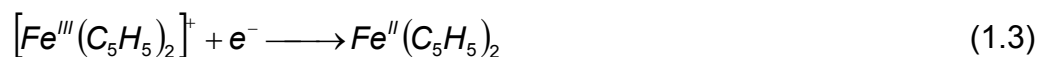
De nuevo, la corriente se incrementa rápidamente (i hasta k) para dar un valor máximo de E_p^{red} (pico de reducción). A medida que transcurre la reducción, la concentración de $[Fe^{III}(C_5H_5)_2]^+$ se agota en la superficie del electrodo, y otra vez tiene lugar una caída de intensidad, debida al control difusivo del proceso (j hasta k).

Para los procesos reversibles (el equilibrio se establece en la escala de tiempos del experimento), el potencial formal de reducción E_0' tiene un valor aproximado al del valor medio de los dos potenciales de pico:

$$E^{0'} = \frac{E_p^{ox} + E_p^{red}}{2} \qquad (1.4)$$

La separación entre los picos de potencial (E_p^{ox} y E_p^{red}) está relacionada con el número de electrones (n) transferidos en la reacción electrónica [44]:

$$\Delta E_p = E_p^{ox} - E_p^{red} \cong \frac{0.059}{n} \qquad \text{a 25°C} \qquad (1.5)$$

La transferencia de electrones lenta (irreversibilidad) o la resistencia no

compensada (caída óhmica), provocan que ΔE_p aumente. Los valores de i_p^{ox} y

i_p^{red} deberían ser idénticos para un par reversible. La irreversibilidad química,

en la que una reacción química es acoplada al proceso electródico, causa

desviaciones de la unidad respecto a la relación i_{pox} / i_{pred}, lo que puede servir

como valiosa información a la hora de caracterizar un proceso electroquímico.

Cuanto más irreversible se presenta un sistema, mayor es esta desviación,

llegando a desaparecer el pico inverso en el proceso para los casos totalmente

irreversibles.

Finalmente, para un sistema reversible, E_p es independiente de la

velocidad de barrido. Sin embargo, la corriente de pico sí depende de este

parámetro, a través de la ecuación de Randles- Sevcik [44]:

$$i_p = 2.69 \cdot 10^5 \cdot n^{3/2} \cdot A \cdot D^{1/2} \cdot c \cdot v^{1/2} \qquad \text{a } 25^\circ\,C \qquad\qquad (1.6)$$

Donde i_p es la corriente de pico (A), n es el número de electrones

intercambiados, A es el área del electrodo (cm^2), D es el coeficiente de difusión

($cm^2\ s^{-1}$), C es la concentración ($mol\ cm^{-3}$), y v es la velocidad de barrido ($V\ s^{-1}$).

Teniendo en cuenta la ecuación de Randles-Sevcik, y realizando una adecuada

calibración, puede deducirse importante información de un proceso a partir de

su voltagrama cíclico, como el número de electrones intercambiados, el área de

electrodo, coeficiente de difusión o concentración de especie electroactiva.

1.3.1.2 - Cronoamperometría.

Esta técnica lleva consigo, primero, la aplicación de un potencial inicial E_i, en el que no ocurre ninguna reacción de tipo faradaico. Una vez se alcanza el equilibrio, se produce un pulso de potencial hasta un potencial final, E_r, el cual provoca que se lleve a cabo la reacción redox del compuesto de interés. El potencial se mantiene durante un tiempo, t_r, determinado (Figura 1.12). Simultáneamente se registra la intensidad generada en función del tiempo, dando lugar a una curva I-t como la que se muestra en la figura 1.12B. Generalmente, el estudio del proceso inverso también suele ser interesante, en tal caso se realiza de manera consecutiva, aplicando un potencial E_{r2}, al cual la reacción inversa tiene lugar.
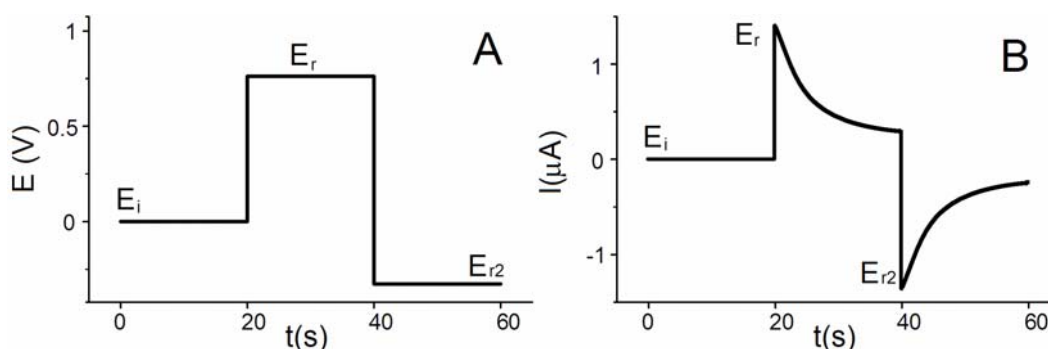
Figura 1.12. A) Forma de la onda de potencial para la cronoamperometría de doble pulso. B) Curva i-t resultante de la aplicación de la onda de potencial.

Cuando se consideran reacciones en disolución, la caída de la corriente faradaica tras el salto hasta E_r es descrita por la ecuación de Cottrell [44]

$$I_f(t) = \frac{nFAD^{1/2}c_0}{\pi^{1/2}t^{1/2}}$$ (1.7)

Donde n es el número de electrones, F es la constante de Faraday (C mol^{-1}), A es el área de electrodo (cm^2), D el coeficiente de difusión (cm^2 s^{-1}), c_o la concentración de analito en el seno de la disolución (mol cm^{-3}), y t es el tiempo (s) transcurrido desde la aplicación del pulso de potencial.

La corriente registrada contiene también una componente capacitativa. Ésta decae muy rápidamente, por lo que sólo será significativa a tiempos muy cortos. Además, lo hace de manera exponencial con el tiempo de acuerdo con la siguiente ecuación [44]:

$$I_c(t) = \frac{\Delta E}{R}\, e^{\frac{-t}{RC}}$$ (1.8)

Donde R = resistencia (ohm) y C = capacidad (F).

1.3.1.4. Medidas de capacidad vs Potencial.

Un condensador se forma cuando dos superficies conductoras están separadas por un medio no conductor, llamado dieléctrico. En los sistemas electroquímicos formados por películas superficiales adheridas sobre electrodos, las dos superficies conductoras son el electrodo y la disolución, y el medio no conductor es la película que recubre el electrodo. El valor de la capacidad (C) depende de la superficie del electrodo (A), el grosor del

recubrimiento (d) y la constante dieléctrica de éste (ε_r). La relación entre todos estos parámetros viene dada por [44] :

$$C = \frac{\varepsilon_0 \varepsilon_r A}{d} \qquad (1.9)$$

Donde ε_0 es la permitividad en el vacío, que es una constante física, mientras que la constante dieléctrica, ε_r, depende del material. Así, $\varepsilon_r=1$ en el vacío, para el agua su valor es 80 y para un recubrimiento orgánico su valor oscila de 4 a 8 [46].

Para obtener valores de capacidad de una película orgánica se requiere hacer medidas de impedancia electroquímica (electroquímica AC). La principal diferencia con la electroquímica de corriente continua es que la señal de excitación pasa de ser un potencial real a un potencial complejo, con lo que en lugar de medir resistencias se miden impedancias. En medidas de impedancia se superpone a la señal de potencial continua una onda con frecuencia y amplitud definidas, de manera que:

$$E = E_0 sen(\omega t) \qquad (1.10)$$

la intensidad obtenida también tendrá una forma sinusoidal:

$$I = I_0 sen(\omega t + \varphi) \qquad (1.11)$$

Aplicando la relación de Euler a (1.10) y (1.11) se obtiene:

$$E(\omega t) = E_0 \exp(j \cdot \omega t) \qquad y \qquad I(\omega t) = I_0 \exp(j \cdot \omega t - \varphi) \qquad (1.12) \text{ y } (1.13)$$

Pudiéndose expresar la impedancia como una función compleja:

$$Z(\omega) = \frac{E(\omega t)}{I(\omega t)} = Z_0 \exp (j\varphi) = Z_0(\cos \varphi + j \sin \varphi) \qquad (1.14)$$

Normalmente, un electrodo conductor recubierto por un compuesto orgánico tiene una alta impedancia. En estos casos, el comportamiento del sistema puede explicarse mediante el empleo de un circuito equivalente, en el que sólo será necesario tener en cuenta una resistencia y un condensador, lo que está ampliamente descrito en la bibliografía [44-47]. La relación entre la capacidad y la parte compleja de la impedancia viene dada por:

$$C = \frac{1}{j\omega Z} \qquad (1.15)$$

Por tanto, la medida de la impedancia resultante a cada potencial, y trabajando a una frecuencia constante, podremos obtener el valor de capacidad resultante en función del potencial.

1.5.4 Espectroelectroquímica UV-Vis.

La espectroelectroquímica consiste en la obtención y el análisis de la respuesta espectral originada sobre la superficie del electrodo durante la realización de cualquier experiencia electroquímica. Esta técnica relativamente reciente se presenta como un método potencialmente muy útil para seguir las reacciones electródicas a través de reactivos, productos o intermedios que absorban luz a alguna longitud de onda transmitida por el electrodo. Cuando el rango espectral en el que se trabaja está en el Ultravioleta – Visible, se le denomina "Espectroelectroquímica UV-Vis". Datan de mediados de la década de los sesenta las primeras experiencias espectroelectroquímicas [48], y desde entonces, el creciente interés que suscita esta técnica es patente, lo que se pone de manifiesto en el elevado número de publicaciones que hacen uso de las medidas espectroelectroquímicas, y que representan el constante desarrollo desde sus comienzos hasta nuestros días, tanto en el aspecto teórico como en el experimental. El desarrollo de los electrodos de vidrio recubiertos por óxido de estaño (ITO) [48], y de otros electrodos óptimamente transparentes (OTTLE), como la minirrejilla de oro [49], resultó fundamental en la expansión de la espectroelectroquímica, por su facilidad de adecuación a las medidas por transmisión realizadas hasta el momento. Estas primeras medidas, denominadas "Espectroelectroquímica de transmisión normal con difusión semiinfinita" [44], consisten en que el haz de luz incide perpendicularmente sobre el electrodo. Partiendo desde fuera de la celda, atraviesa la capa de difusión y la disolución antes de salir de nuevo de la celda y ser detectado. La

intensidad luminosa se atenúa por la concentración de las especies absorbentes, ya sean reactivos, productos o intermedios.

Debido en parte a la falta de celdas espectroelectroquímicas comerciales, la gran diversidad existente en dispositivos experimentales válidos ha condicionado por una parte el desarrollo conceptual, y por otra, el contenido de las revisiones bibliográficas referidas a este tema, siendo parte importante de esta investigación la fabricación de electrodos y celdas electroquímicas. Los diferentes tipos de celdas electroquímicas, en los que actualmente es aplicada la espectroelectroquímica UV-Vis, pueden clasificarse en:

1.   Celdas con electrodos ópticamente transparentes.

2.   Celdas con electrodos de capa fina ópticamente transparentes.

3.   Celdas donde el haz de luz pasa rozando la superficie activa del electrodo (LOP).

4.   Celdas de capa fina con largo camino óptico (LOPTLC).

5.   Celdas de reflectancia.

1.5.4.1. Aspectos experimentales.

La mayoría de espectrofotómetros UV-Vis existentes en el mercado pueden adaptarse para realizar medidas espectroelectroquímicas, aunque hay ciertas características especiales, como la posibilidad de sincronización a un potenciostato o una adecuada velocidad de adquisición de espectros, entre otras, que facilitan la aplicación y posibilitan la obtención de datos, los cuales pueden suministrar información muy útil.

La correcta sincronización entre el potenciostato y el espectrofotómetro se convierte en un factor determinante, en función del tipo de proceso que se estudia y de las condiciones experimentales. Es fundamental para saber en todo momento a qué potencial y en qué momento del pulso de potencial se están tomando las medidas. Si los saltos de potencial son breves, o la cinética del proceso es muy rápida, es necesario que el tiempo de respuesta del disparador sea lo suficientemente rápido para que no se cometan errores de sincronización apreciables. Sin embargo, si se trata de una cinética no muy rápida, la velocidad de adquisición y la sincronización toman un papel secundario, siendo sólo necesario un control muy básico de este factor. Este último es el caso de los procesos estudiados en la presente tesis, para la cual simplemente ha sido necesario empezar ambos registros, espectroscópico y potenciostático al mismo tiempo, y realizar un registro detallado tanto del potencial como de los espectros generados en función del tiempo. De esta forma, es posible asignar un potencial a cada espectro registrado.

El hecho de que la composición sobre el electrodo o en la disolución esté cambiando, como consecuencia de la reacción ocurrida en el electrodo, obliga a que la medida de absorbancia sea tomada en el menor tiempo posible, y a la vez para todas las longitudes de onda. Se consigue así un espectro que capture el instante preciso presente en la disolución. Por tanto, el tiempo de respuesta del detector debe ser el adecuado para poder tomar espectros a velocidad suficientemente elevada a lo largo de una experiencia. Para este fin, conviene que el detector sea una batería de diodos, ya que este sistema permite tomar espectros completos para un mismo tiempo. Aunque en muchos casos basta conocer la respuesta espectroscópica a una sola longitud de onda, la información de un espectro completo resulta imprescindible cuando se pretende elucidar mecanismos de reacción complicados.

1.4 BIBLIOGRAFÍA.

[1] J.P. Farges (ed.), Organic Conductors: Fundamentals and Application, Marcel Dekker, 1994;

[2] H.S. Nalwa (ed.), Handbook of Organic Conductive Molecules and Polymers, vols. 1-4, Wiley, 1997;

[3] T.A. Skotheim, R.L. Elsenbaumer, J.R. Reynolds (eds.), Handbook of Conducting Polymers, Marcel Dekker, Inc., 1998.

[4] G. Saito, S. Kagosima (eds.), The Physics and Chemistry of Organic Superconductors, Springer-Verlag, 1990;

[5] J.M. Williams, J.R. Ferraro, R.J. Thorn, K.D. Carlson, U. Geiser, H.H. Wang, A.M. Kini, M.H. Whangbo, Organic Superconductors (Including Fullerenes), Prentice Hall, 1992.

[6] J.H. Burroughes, D.D.C. Bradley, A.R. Brown, R.N. Marks, K. Mackay, R.H. Friend, P.L. Burns, A.B. Holmes, Nature, 347 (1990) 539.

[7] R.S. Potember, R.C. Hoffman, H.S. Hu, J.E. Cocchiaro, C.A. Viands, R.A. Murphy, T.O. Poehler, Polymer, 28 (1987) 574;

[8] T.C. Pearce, S.S. Schiffman, H.T. Nagle, J.W. Gardner, Handbook of machine olfaction: Electronic nose technology, John Wiley & Sons, 2003;

[9] R.H. Friend, R.W. Gymer, A.B. Holmes, J.H. Burroughes, R.N. Marks, C. Taliani, D.D.C. Bradley, D.A Dos Santos, J.L. Brédas, M. Lögdlund, W.R. Salaneck, Nature, 397 (1999) 121;

[10] C.D. Dimitrakopoulos, P.R.L. Malenfant, Adv. Mater., 14 (2002) 99;

[11] G. Yu, J. Gao, J.C. Hummelen, F. Wudl, A.J. Heeger, Science, 270 (1995) 1789.

[12] G. de la Torre, L. Sánchez, N. Martín, Anales de la Real Sociedad Española de Química, segunda época, octubre-diciembre, (2002) 5.

[13] T. Fernández-Otero, J.M. Sansiñena, Adv. Mater., 10 (1998) 491;

[14] T. Fernández-Otero, M.T. Cortés, Adv. Mater., 15 (2003) 279.

[15] J. Ferraris, D.O. Cowan, V.V. Walatka, J.H. Perlstein, J. Am. Chem. Soc., 95 (1973) 948;

[16] L.B. Coleman, M.J. Cohen, D.J. Sandman, F.G. Yamagishi, A.F. Garito, A.J. Heeger, Solid State Commun., 12 (1973) 1125.

[17] A.K. Bakhshi, Y. Yamaguchi, H. Ago, T. Yamabe, Mol. Eng., 6 (1996) 239.

[18] a) N. Martin, C. Seoane, Mundo Científico, 11 (1991) 820; b) M.R. Bryce, Chem. Soc. Rev., 20 (1991) 355;

[19] D. Jérôme, A. Mazaud, M. Ribault, K. Bechgaard, J. Phys. Lett.-Paris, 41 (1980) L-95.

[20] R.C. Haddon, Acc. Chem. Res., 25 (1992) 127.

[21] W. Krätschmer L.D. Lamb, K. Fostiropoulos, D.R. Huffman, Nature, 347 (1990) 354.

[22] A.F. Hebard, M.J. Rosseinsky, R.C. Haddon, D.W. Murphy, S.H. Glarum, T.T. Palstra, A.P. Ramirez, A.R. Kortan, Nature, 350 (1991) 600;

[23] Z. Iqbal, R.H. Baughman, B.L. Ramakrishna, S. Khare, N.S. Murthy, H.J. Bornemann, D.E. Morris, Science, 254 (1991) 826.

[24] T.J. Marks, Science, 227 (1985) 881; M. Hanack, M. Lang, Adv. Mater., 6 (1994) 819;

[25] H. Schultz, H. Lehmann, M. Rein, M. Hanack, Struct. Bond., 74 (1991) 41.

[26] a) L.R. Melby, R.J. Harder, W.R. Hertler, W. Mahler, R.E. Benson, W.E. Mochel, J. Am. Chem. Soc., 84 (1962) 3374;

[27]   L.R. Melby, Can. J. Chem., 43 (1965) 1448.

[28] A.J. Epstein, S. Etemad, A.F. Garito, A.J. Heeger, Phys. Rev. B, 5 (1972) 952.

[29] T.J. Kistenmacher, T.E. Phillips, D.O. Cowan, Acta Crystallogr. B, 30 (1974) 763.

[30] C. Katan, J. Phys. Chem. A 1999, 103, 1407;

[31] I. Hargittai, J. Brunvoll, M. Kolonits, V. Khodorkovsky, J. Mol. Struct. 1994, 317, 273.

[32] Lee C.; Bard, A. J. J. Electroanal. Chem. 1988, 239, 441.

[33] Sánchez-Maestre, M.; Rodríguez-Amaro, R.; Muñoz, E.; Ruiz, J. J.; Camacho, L. J. Electroanal. Chem. 1993, 359, 325.

[34] Millán, J. I.; Sánchez-Maestre, M.; Camacho, L.; Ruiz, J. J.; Rodríguez-Amaro, R. Langmuir 1997, 13, 3860.

[35] Arihara, K.; Kitamura, F.; Ohsaka, T.; Tokuda, K. J. Electroanal. Chem. 2000, 488, 117.

[37] C. Shoot, J. J. Ponjeé, H. T. van Dam, R A vanDoom y P. T. Bolwijn; Appl. Phys. Letter., 23 (1973) 64.

[38] H. T. van Dam y J. J. Poonjeé; J. Electrochem. Soc., 121 (1974) 1555.

[39] H. T. van Dam; J. Electrochem. Soc., 123 (1976) 1181.

[40] R. J. Jasinski; J. Electrochem. Soc., 124 (1977) 637.

[41] C.D. Jaeger, A.J. Bard ; J. Am. Chem. Soc. 102 (1980) 5435

[42] E. Ortí, R. Viruela, P.M. Viruela, en Los Materiales Moleculares en España en el Umbral del Siglo XXI, (P. Vázquez, T. Torres, N. Martín, eds.), UAM Ediciones, 2001, 271.

[43] M.E. Hawley, T.O. Poehler, T.F. Carruthers, A.N. Bloch, D.O. Cowan, Bull. Am. Phys. Soc., 23 (1978) 424.

[44] Bard, A.J., Faulkner, L.R.; Electrochemical Methods: Fundamentals and Applications. New York: Wiley Interscience Publications 2000.

[45] Park SM, Yoo JS ; Anal. Chem. 75 (2003) 455A.

[46] D. Loveday, P. Peterson, R. Rodgers, JCT CoatingsTech, 46-52, August 2004.

[47] Scully, J.R., Silverman, D.C., and Kendig, M.W. (Ed.), Electrochemical Impedance: Analysis and Interpretation, ASTM, West Conshohocken, PA, 1993.

[48] Kuwana, T.; Darlington, R.K.; Leedy, D.W., *Analytical Chemistry* 1964, 36, 2023 -2025.

[49] Piljac, I.; Tkalcec, M.; Grabaric, B., *Analytical Chemistry* 1975, 47, 1369 - 1372.

42

CAPÍTULO II.

TRANSICIONES DE FASE. NUCLEACIÓN Y CRECIMIENTO EN PELÍCULAS DELGADAS ORGANIZADAS.

2.1. Introducción. Teoría de Nucleación – Crecimiento – Colisión.

El ejemplo más simple de cambio de fase electroquímico consiste en la deposición de metales sobre electrodos (electrocristalización) a partir de iones en disolución [1-5]. El primer caso de transición de fase de una molécula orgánica sobre electrodos, descrito como tal, data de 1969. Así, Armstrong [6] observó que la adsorción-desorción de una monocapa de piridina en la interfase H_2O-Hg se adaptaba a un mecanismo de nucleación y crecimiento, semejante a los procesos de electrocristalización de metales. Por tanto, la deposición o condensación de metales en estado vapor sobre una superficie plana sirve como punto de partida para la interpretación de los fenómenos de cambio de fase electroquímico de moléculas orgánicas sobre la superficie electródica.

Hay gran variedad de modelos para describir estos procesos, en función del átomo o la molécula involucrada. Se pueden dividir en bidimensionales (2D), con un posible crecimiento posterior capa a capa, y tridimensionales (3D). En el caso de moléculas orgánicas, la transición de fase sobre la superficie del electrodo consiste, básicamente, en el paso desde un estado con moléculas al azar y una mínima interacción entre ellas, hasta un estado donde las moléculas están adsorbidas en posiciones fijas, formando una película ordenada por fuerzas cohesivas más fuertes.

Existen diversas teorías cinéticas de formación de fases 2D ó 3D, [7]. Sin embargo, las únicas aplicadas en un contexto electroquímico son las que tratan de interpretar estos fenómenos en base a la formación de un núcleo crítico. De especial interés en electroquímica son las teorías de Nucleación-Crecimiento-Colisión (NCC). En ellas se considera que, a partir de una alteración del potencial electródico, sobre la superficie de un electrodo se forma un agregado o cluster, el cual se disolverá si su tamaño es menor que el del núcleo crítico. Sin embargo, este cluster será estable si su tamaño es mayor que dicho valor crítico. Estos embriones, o núcleos estables, permitirían un posterior crecimiento de la nueva fase formada. De esta manera, la teoría NCC es capaz de explicar el comportamiento electroquímico de estos procesos y, en algunos casos, suministrar criterios de diagnóstico específicos.

La estabilidad y crecimiento de los núcleos para dar lugar a la nueva fase condensada está regida por dos factores de signos opuestos: la energía Gibbs ganada por la formación del cluster, y el trabajo gastado en expandir la frontera periférica del núcleo [8,9]. Suponiendo núcleos esféricos, la expresión correspondiente a la variación de energía Gibbs sería:

$$\Delta G = G_v \frac{4}{3}\pi r^3 + \gamma 4\pi r^2 \qquad (2.1)$$

Donde G_v es la energía Gibbs por unidad de volumen asociada a la formación de la fase, r es el radio de la esfera y "γ" es la superficie libre por unidad de área. En la Figura 2.1 puede verse la representación del

comportamiento de ΔG, en el que el valor máximo corresponde a un radio igual al radio crítico, que es el necesario para que la formación del núcleo esté energéticamente favorecida. El primer término, proporcional a r^3, es un término energético para el trabajo de formación del volumen del cristal. Esta energía es negativa y, por tanto, favorece la formación. Sin embargo, el segundo término de la ecuación, proporcional a r^2 es positivo, y se refiere al coste energético de formar una nueva superficie. Inicialmente domina el segundo término, lo que significa que un cristal de radio crítico tiene que ser formado antes de que su crecimiento sea favorable.
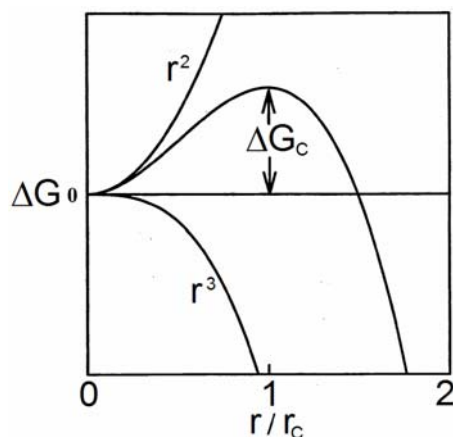
Figura 2.1. Curvas esquemáticas de energía Gibbs asociadas a la nucleación y crecimiento de un cristal. La curva resultante pasa por un máximo cuando el radio alcanza el radio crítico.

Aunque estas teorías son capaces de explicar numerosos fenómenos de cambios de fase de moléculas orgánicas, en ocasiones incluso de forma cuantitativa, hay que tener en cuenta una serie de limitaciones en su posible

aplicación:

1- Se asume que no hay influencia por parte del disolvente o de las moléculas del electrolito soporte, que recubren el electrodo, antes de la formación de los núcleos.

2- No se considera la posible heterogeneidad de la superficie electródica, obviándose así los posibles sitios preferentes de nucleación en función de la estructura cristalina.

3- En el caso de moléculas orgánicas, no se tiene en cuenta la estructura de la molécula que forma los núcleos, ya que se consideran de simetría esférica.

2.2. Transiciones de fase bidimensionales.

El estudio de las monocapas condensadas sobre un electrodo presenta un amplio interés, debido a que intervienen en gran variedad de procesos electroquímicos como son la electrocatálisis o la inhibición de la corrosión, así como en dispositivos electrocrómicos, biosensores, etc.

Inicialmente considerados como procesos de adsorción "anómalos" [10], los procesos de transición de fase fueron la primera evidencia experimental de un comportamiento de adsorción no ideal. En una adsorción "normal", aunque la molécula en disolución está en contacto con la superficie del electrodo, se

encuentra mayoritariamente rodeada por el disolvente. Por el contrario, las moléculas orgánicas en la película 2D están, en su mayor parte rodeadas de moléculas similares, quedando solo una pequeña parte en contacto con la disolución.

Ciertas moléculas tienden a acumularse espontáneamente en las interfases y formar monocapas o multicapas organizadas. La interacción ocurre mediante la acción de fuerzas atractivas de corto alcance, como las dipolo-dipolo o enlaces de hidrógeno, por lo que, bajo una adecuada polarización local, las moléculas anfifílicas son las más propicias a favorecer este tipo de interacciones, obteniéndose un empaquetamiento compacto, como en el caso de derivados de piridina y bipiridina [6,11-15], de purina y pirimidina [17-20].

La naturaleza de estos fenómenos es aún más compleja, ya que además de la formación de monocapas 2D, la fase 2D condensada puede sufrir gran variedad de modificaciones interfaciales [21] como, entre otros, la reorientación del surfactante, la sustitución de un adsorbato por otro diferente, o procesos de formación de capas condensadas mixtas, resultantes de fenómenos de coadsorción energéticamente favorables.

Transición de fase a potencial constante

Según la teoría NCC, el fenómeno de nucleación y crecimiento se divide, idealmente, en cuatro procesos independientes: velocidad de nucleación, crecimiento de núcleos, coalescencia de los núcleos formados y corriente eléctrica intercambiada. Los tres primeros factores serán tratados en este apartado. Sin embargo, la respuesta a las técnicas electroquímicas, en las que se analiza la corriente intercambiada, será tratada posteriormente con mayor detalle, analizando pormenorizadamente el tipo de respuesta originado en cada tipo de técnica utilizada.

a) Velocidad de nucleación.

Sea el proceso electródico reversible:

$$Ox + ne^- \longrightarrow Red \tag{2.2}$$

donde *Ox* y *Red* son especies adsorbidas sobre el electrodo. En el caso genérico en el que la especie *Red* se adsorbe mucho más fuertemente que la *Ox*, aparecería una preonda de adsorción [22,23] si hay ausencia de condensación, lo que no debe confundirse con un fenómeno de transiciones de fase.

En la práctica, los núcleos de una superficie tienen diferentes velocidades de nucleación entre sí (nucleación policinética). Sin embargo, hay

superficies cuasi-ideales en el que todos los sitios activos poseen la misma velocidad de nucleación (nucleación monocinética). En éstas últimas, es posible hacer un tratamiento matemático considerando, únicamente, la variación del número de núcleos formados sobre el electrodo (N), y el número de sitios disponibles para la formación de núcleos (N_d) que serán iguales pero con distinto signo:

$$\frac{dN}{dt} = -\frac{dN_d}{dt}$$

(2.3)

Suponiendo que Red se encuentra en exceso, se puede obviar el fenómeno de difusión en el proceso global [2,24], lo que permite considerar una cinética de primer orden para la desaparición de N_d [24]

$$N_d = N_0 e^{-At}$$

(2.4)

donde A es la constante de velocidad de nucleación y N_0 es el número de sitios disponibles para la nucleación a tiempo cero. Evidentemente, la velocidad de formación de núcleos, según las ecuaciones (3) y (4) será:

$$\frac{dN}{dt} = AN_0 e^{-At}$$

(2.5)

b) Crecimiento de los núcleos

Una vez formado el núcleo de tamaño crítico de radio *r*, éste comienza a crecer. Suponiendo una velocidad radial de expansión del núcleo bidimensional independiente de su radio y del solapamiento, la superficie ocupada por los núcleos, S_{exp}, se describe por la convolución de la nucleación y su proceso de crecimiento [25-27], que para el caso en el que todos los núcleos se forman a la vez (nucleación instantánea) da lugar a que $S_{exp} = N_0 \pi r^2$

c) Solapamiento o coalescencia

Al crecer los núcleos, crecen y solapan entre ellos, lo que reduce el área efectiva (*S*) de recubrimiento del electrodo. Estadísticamente, Avrami representó este fenómeno mediante la expresión [28-30]:

$$S = 1 - e^{-S_{exp}} \qquad (2.6)$$

La cual se ha demostrado válida por métodos de simulación como el de Monte Carlo para recubrimientos del electrodo inferiores al 95%. Si el recubrimiento es mayor, se presentan desviaciones que afectan principalmente a la parte final o cola de la transición de fase.

2.2.1 Respuesta Electroquímica.

Para abordar el estudio de los procesos de transición de fase se pueden usar diferentes técnicas electroquímicas. Se ha observado que la aparición de la capa condensada provoca que los valores de capacidad diferencial, densidad de carga y exceso superficial, permanezcan estables en el rango de potenciales donde existe la fase. Cualquiera que sea el proceso interfacial responsable, la transición de fase va asociada a un cambio de pendiente de la curva electrocapilar, o a una repentina variación del exceso superficial. Sin embargo, la reproducibilidad de estas medidas es escasa en la región donde existe la película, lo que hace que no sean de gran utilidad. Por consiguiente, el estudio de las transiciones de fase se ha abordado, principalmente, mediante técnicas como voltametría, cronoamperometría (curvas i-t) o medidas de capacidad frente al potencial.

Es importante indicar que las fases condensadas pueden producirse sin intercambio de corriente faradaica [6,8,9,31-37] (proceso puramente capacitativo, debido exclusivamente a la corriente de carga), o con intercambio de corriente faradaica [14,15,38-41], en cuyo caso la fase es formada por un intermediato o producto de reducción u oxidación. Cuando no hay intercambio de corriente faradaica, las técnicas principales de estudio son la medida de la capacidad diferencial en función del potencial (curvas C-E) o del tiempo (curvas C-t), mientras que cuando hay intercambio de corriente se emplea principalmente la cronoamperometría. En ambos casos, puede observarse

mediante la voltametría cíclica la formación de la fase bidimensional a través de la aparición de picos muy estrechos y puntiagudos sin cola de difusión [42]. Los potenciales a los que aparecen estos picos coinciden con los correspondientes a los de formación de la película. En el caso de ausencia de intercambio de corriente faradaica, estos picos suelen ser tener un area del orden de 1-2 $\mu C/cm^2$ [13,42]. Sin embargo, con intercambio la carga, el área suele ser mucho mayor, como ocurre para los viológenos, de unos 20 $\mu C/cm^2$ [14,15,43].

2.2.1.1. *Voltametría.*

A partir de la teoría NCC, y considerando la aproximación de que la velocidad de nucleación del proceso es estacionaria, lo cual sólo se cumple a bajas velocidades de barrido, se llega a la conclusión de que la velocidad de nucleación es independiente de que la nucleación sea instantánea, progresiva o, incluso, de que se adapte a otros modelos cinéticos. La expresión final que se obtiene es [44]:

$$i = \pm \frac{q_m b}{fv} \eta^4 c^{\pm \frac{b\eta^5}{5v^2}} \qquad\qquad (2.7)$$

Siendo el sobrepotencial aplicado $\eta = \dfrac{E - E^0 - vt}{f}$ para el barrido catódico y $\eta = \dfrac{E - E^0 - v(t - t_m)}{f}$ para el barrido anódico, $f = RT/nF$, q_m la carga

total intercambiada, v la velocidad de barrido y t_m el tiempo empleado en el barrido de ida para el barrido anódico. El signo + se usa en procesos de reducción (sobrepotencial negativo), y el signo – para procesos de oxidación (sobrepotencial negativo). b es una constante relacionada con la cinética de nucleación, que al ser diferente para la reducción y la oxidación tiene valores independientes en ambos casos.

Si se analiza detenidamente la ecuación (2.7), se deduce fácilmente que para $E=E^0$, es decir $\eta=0$, la corriente debe ser cero, tanto para la reducción como para la oxidación. Por tanto, debe existir una zona de potenciales entre ambos picos en donde la corriente sea cero. Esto conlleva que la cinética de nucleación debe estar sometida a un fenómeno de histéresis, de forma que es necesario un cierto sobrepotencial para que tenga lugar la formación o destrucción de la fase 2D.

Los picos obtenidos son semejantes a los resultantes en la oxido-reducción reversible de moléculas inmovilizadas en el electrodo que presentan entre ellas fuertes interacciónes atractivas [7,45,46]. Sin embargo, entre ambos se presenta una diferencia notable respecto al comportamiento de los picos con la velocidad de barrido. Así, para los procesos de transición de fase 2D, la anchura a mitad de altura, W (V), la histéresis entre los procesos de reducción y de oxidación, ΔE_p (V), así como la intensidad de pico, i_p (A) disminuyen al disminuir la velocidad de barrido (v). A partir de la ecuación (2.7) se pueden obtener varias expresiones, que sirven como criterio de diagnóstico para este

tipo de procesos y ayudan a diferenciarlos de otros [44]:

$$i_p = cte \cdot v^x \quad \Delta E_p = cte \cdot v^{(1-x)} \quad W = cte \cdot v^{(1-x)} \quad \text{Con } x \geq 0.6 \tag{2.8}$$

2.2.1.2. Cronoamperometría

Aunque el estudio voltamétrico proporciona información valiosa acerca de este tipo de procesos, sin embargo, para caracterizarlos es fundamental el estudio de la forma de las curvas i-t generadas en cronoamperometría [2,5]. Tras el salto cronoamperométrico se registran curvas i-t con un máximo de intensidad a tiempo diferente de cero, lo que no es atribuible a ningún proceso en el que la etapa controlante sea de tipo cinético, de transferencia eléctrica o de difusión [47,48].

Para explicar el comportamiento y la forma de las curvas de los procesos de nucleación y crecimiento bidimensionales, suele utilizarse el modelo de Bewick- Fleischmann- Thirsk (BFT), desarrollado inicialmente para la formación de películas anódicas sobre mercurio [1,49]. La ecuación general prevista por este modelo es:

$$i_{BFT} = \left(t - \frac{1}{A} + \frac{e^{-At}}{A} \right) \exp\left[-b\left(\frac{t^2}{2} + \frac{1}{A^2} - \frac{t}{A} + \frac{e^{-At}}{A^2} \right) \right] \tag{2.9}$$

donde q_m es la carga total del proceso de formación de la fase, b (s^{-2}) es un

parámetro relacionado con la velocidad de crecimiento de los núcleos, y A (s^{-1}) es la constante de velocidad de formación de los núcleos, analizada en las ecuaciones (4) y (5).

Independientemente de que el proceso transcurra con intercambio de corriente faradaica o sin él, se pueden definir dos casos extremos en función de la velocidad de nucleación:

a) Nucleación instantánea [2,5]. Se da cuando la constante de la velocidad de nucleación tiende a infinito (A→∞), por lo que la fase se forma a partir de pocos núcleos que se forman a la misma vez y desarrollan muy deprisa. En este caso se cumple la relación:

$$\frac{i_m t_m}{q_m} = \frac{1}{\sqrt{e}} = 0.606 \tag{2.10}$$

donde i_m es la corriente máxima, t_m el tiempo para el que $i=i_m$ y q_m la carga total intercambiada. La ecuación que rige el proceso es:

$$\frac{i}{i_m} = \left(\frac{t}{t_m}\right) e^{-\frac{1}{2}\left[\left(\frac{t}{t_m}\right)^2 - 1\right]} \tag{2.11}$$

b) Nucleación progresiva: Se da cuando la constante de velocidad es pequeña (A→0). En este caso, la fase 2D se forma a partir del solapamiento de numerosos núcleos que se van formando y crecen poco a poco. Las ecuaciones correspondientes son:

$$\frac{i_m t_m}{q_m} = 2e^{-\frac{2}{3}} = 1.027 \tag{2.12}$$

$$\frac{i}{i_m} = \left(\frac{t}{t_m}\right)^2 e^{-\frac{2}{3}\left[\left(\frac{t}{t_m}\right)^3 - 1\right]} \tag{2.13}$$

Los criterios dados en las ecuaciones anteriores, así como el ajuste numérico de los datos experimentales a las ecuaciones mostradas, han sido utilizados para distinguir estos dos casos límite de nucleación. En la siguiente Figura pueden observarse la forma típica de las curvas para estos dos casos extremos.
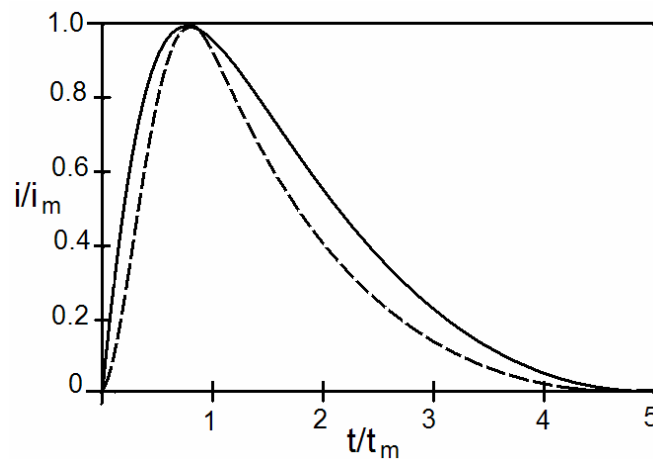
Figura 2.2. Imagen representativa de las curvas cronoamperométricas en los casos de nucleación instantánea (continua) y progresiva (discontinua).

2.2.1.3. Medidas de Capacidad frente al Potencial.

Además de la voltametría y la cronoamperometría, las medidas de capacidad diferencial, a potenciales anteriores y posteriores a la aparición de los procesos de nucleación, permiten analizar la estructura de la interfase [13,42].

Una característica particular de las transiciones de fase es la aparición de un cambio muy brusco de capacidad [50,51] cuando se produce la transición de fase, lo que diferencia claramente estos procesos de los característicos picos de adsorción-desorción sobre electrodos [32, 50]. Al igual que los picos voltamétricos a los que están asociados, estos saltos de capacidad presentan histéresis [33,51] entre el barrido catódico y el anódico. En las transiciones de fase bidimensionales ocurre la aparición de un pozo de capacidad constante dentro de un determinado rango de potenciales. Esta región está delimitada, en la mayoría de los casos, por dos escalones que corresponden a la formación y destrucción de la fase. El valor de capacidad en este pozo es independiente del potencial, temperatura y concentración; sin embargo, el rango de potencial al que aparece sí depende de estos factores a través de su influencia sobre la capa de difusión de la doble capa. Esta dependencia es debida a la alteración del proceso de adsorción [21], y por tanto, de las interacciones entre moléculas adsorbidas o en la densidad de carga del electrodo dando lugar a diversas modificaciones.
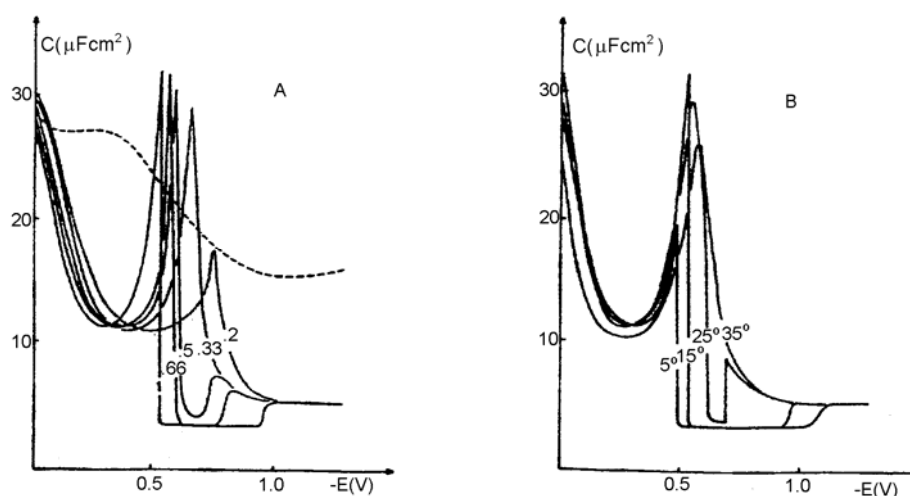
Figura 2.3. Curvas de capacidad para isoquinoleina obtenidas a diferentes concentraciones (A) y a diferentes temperaturas (B)

En la Figura 2.3, la parte A muestra las curvas C-E obtenidas en ausencia y presencia de isoquinoleína a diferentes concentraciones, mientras que en la parte B se observa el comportamiento de la cumarina a distintas temperaturas [52]. La consecuencia, tanto del aumento de la concentración como de la disminución de la temperatura, es el ensanchamiento del pozo de capacidad.

Este hecho, típico de un control cinético del proceso interfacial, es debido a que la conversión a un estado más ordenado (fase 2D) requiere, normalmente, una energía de activación que puede ralentizar la transición, de forma que la escala de tiempo en que se realiza dicha transición, la hace experimentalmente accesible [21,53].

La explicación de este comportamiento se ha abordado desde dos perspectivas diferentes, el modelo basado en las isotermas de Frumkin desarrollado por Damaskin [54], y el del gas reticular desarrollado por Ising [55-58]. En ambos casos, se considera que la discontinuidad separa dos estados o películas que compiten por recubrir la superficie del electrodo; la primera, la fase 2D condensada y la segunda, el surfactante junto con el disolvente y el electrolito adsorbidos de manera normal. Posteriormente, como demuestran numerosos estudios, han sido desarrollados y perfeccionados tanto el modelo de Damaskin [55-61], como el de Ising [55,58].

La principal diferencia entre ambos consiste en que, mientras Damaskin basa su modelo en las diferentes energías de adsorción y coeficientes de interacción intermolecular de los dos estados involucrados, lo que implica una isoterma de Frumkin para cada estado, Ising se basa en la razonable suposición de que, bajo condiciones de equilibrio, las moléculas adsorbidas están heterogéneamente distribuidas sobre la superficie. Cada sitio de la red 2D puede estar vacío u ocupado por una molécula, de manera que las únicas interacciones de energía que se consideran son las existentes entre las moléculas más próximas, asumiendo que las fuerzas son de suficiente corto alcance.

Independientemente del modelo utilizado para describir las características de este pozo, basado en la isoterma de Frumkin o en el de Ising del gas reticular, experimentalmente se ha comprobado que el cuadrado de la

anchura de dicho pozo de capacidad cumple la siguiente relación [18,34,62,63]:

$$(\Delta E)^2 = ART \ln c + BT + C \tag{2.15}$$

Donde c es la concentración de adsorbato, T la temperatura, R la constante de los gases, A, B y C constantes experimentales y M se define siguiendo el tratamiento de Sridharan y col. [58] como $\Delta E = E_t^+ - E_t^-$, siendo E_t^+ y E_t^- los potenciales que delimitan la región en la que existe la fase condensada. La ecuación anterior es de carácter aproximado [58,62,63], sin embargo, son numerosos los ejemplos experimentales que se adaptan.

En pricipio, esta ecuación sólo es aplicable en el caso de que sea una única especie la que dé lugar a la fase condensada. No obstante, Wandlowski ha encontrado que la misma ecuación es aplicable para la formación de una fase 2D de sales del tipo M_bX_a, como el nitrato de guanidina [64] y la metilguanidina [65] en relación 1:1.

2.3. Electrocristalización de compuestos orgánicos sobre un electrodo sólido.

La electroquímica de sólidos moleculares, es un campo de estudio en creciente interés, ya que estos materiales son usados en la síntesis de otros nuevos, sobre todo respecto a sus posibles aplicaciones en dispositivos electrónicos. Los sólidos moleculares están formados por moléculas discretas, y suelen tener gran facilidad para ser pegados sobre los electrodos, por lo que representan una forma muy interesante y accesible de estudiar materiales.

A la hora de estudiar electroquímicamente los sólidos moleculares es necesario evitar "a priori" dos problemas principalmente:

El primero, a diferencia de lo que ocurre en la electroquímica de disoluciones diluidas, consiste en que el estudio de estos procesos genera elevadas cantidades de carga intercambiada, debido a que un gran número de compuestos electroquímicamente activos se encuentran en un volumen muy reducido. Como consecuencia, aparece una alta resistencia (iR), que provoca distorsiones de la señal y una mala resolución. El segundo problema puede presentarse cuando el carácter del sólido a estudiar sea aislante, lo que complica aun más el estudio. Para solucionar estos problemas se requiere una técnica que emplee poca materia, y consiga tener en íntimo contacto el sólido con el electrodo. Una técnica que se plantea como muy útil a la hora de estudiar los sólidos moleculares es la electroquímica de partículas

inmovilizadas sobre el electrodo. Hay diversas técnicas para conseguir partículas inmovilizadas, de las cuales, las más comunes son el frotado del electrodo contra el sólido o la técnica de casting, que consiste en dejar un residuo sólido de material orgánico sobre el electrodo tras la evaporación del disolvente que lo contiene. Este método será comentado más ampliamente en posteriores apartados, al ser el que principalmente se ha usado durante la presente tesis.

Un ejemplo típico de reacción en estado sólido sobre un electrodo externo es:

$$M(solido) + Cl^- \longrightarrow MCl(solido) + e^- \tag{2.16}$$
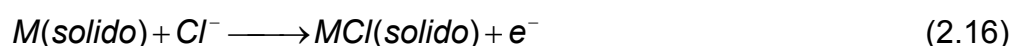
Donde M es el compuesto oxidado, y se une al Cl$^-$ para formar el par iónico. Generalmente, este tipo de procesos presenta mecanismos reversibles, ya que la transferencia electrónica suele estar acompañada de una transferencia iónica a través de una inserción de especies cargadas, presentes en disolución, que entran o salen de manera que se mantenga la condición de electroneutralidad en todo momento [66,67]. En el caso de la ecuación (2.16), el Cl$^-$ es el anión que entra dentro de la estructura de M. A diferencia de los procesos de intercalación [68], en los que los iones entran en el sólido laminado y se alojan en los espacios interlaminares, los procesos de inserción necesitan que el sólido tenga huecos y cavidades para alojar los iones que se introducen en su estructura. La inserción lleva consigo una reorganización de la

estructura del sólido, ya que el ion que ingresa en el sólido necesita hacerse un hueco. Esta transferencia electrónica es parte fundamental del interés en el estudio de estos sistemas, ya que se pueden formar y estudiar electroquímicamente compuestos que, de otra manera, serían muy complejos de obtener. Sin embargo, es condición indispensable que los compuestos que intervienen sean insolubles en el medio de estudio, tanto antes como después del proceso de inserción.

2.3.1. Respuesta electroquímica.

La electroquímica convencional solo mide propiedades relacionadas con los electrones intercambiados en el proceso, pero no da ninguna información de otros mecanismos de los procesos relacionados con la superficie electródica. La mayoría de las técnicas electroquímicas son usadas para confirmar, de manera empírica, la estructura de un compuesto; pero hasta el momento, no es capaz de dar lugar a conclusiones teóricas por sí misma.

Los procesos de electrocristalización comentados en el apartado anterior suelen tener lugar a través de mecanismos regidos por una cinética de nucleación y crecimiento. En este contexto, la electroquímica se ha manifestado como una herramienta de estudio de estos procesos muy poderosa, siendo la respuesta observada para estos sistemas muy diferente a la descrita para la voltametría en disolución, ya que ocurren transiciones de fase, en este caso, tridimensionales en el sólido depositado [69].

Como resultado de su aplicación a las reacciones de transición de fase sobre un electrodo sólido que se encuentra inmerso en la disolución, la señal electroquímica se ve altamente influida por la difusión de iones a través del sólido, llevando consigo la deformación de los picos o curvas obtenidas en las diferentes técnicas. Con objeto de evitar, en la medida de lo posible, la contribución a la señal electroquímica de esta difusión a través del sólido, todas las técnicas electroquímicas deben trabajar a bajo sobrepotencial. Así, el sistema puede ser tratado en algunos aspectos como semejante a una capa delgada, cuyo tratamiento es similar al descrito para las transiciones de fase bidimensionales [69].

2.3.1.1 Voltametría.

El empleo de bajas velocidades de barrido contribuye a minimizar el control difusivo de las partículas dentro del sólido. Una respuesta típica en el estado sólido se muestra en la Figura 2.4 para la reducción de TCNQ (sólido) a $TCNQ^-$ (sólido) [70,71], sobre un electrodo de carbón vitrificado en contacto con una disolución 0.5 M de KCl (aq). Se observa la presencia de picos estrechos y puntiagudos, entre los cuales existe una región de potencial en la que no tiene lugar ninguna reacción electrónica. Esta región se denomina "zona inerte", y su anchura depende del catión presente en la disolución. Su origen, al igual que las transiciones 2D se debe a que es necesario aplicar un sobrepotencial de manera que se suministre la energía necesaria para formar del núcleo crítico y el posterior crecimiento del cristal.
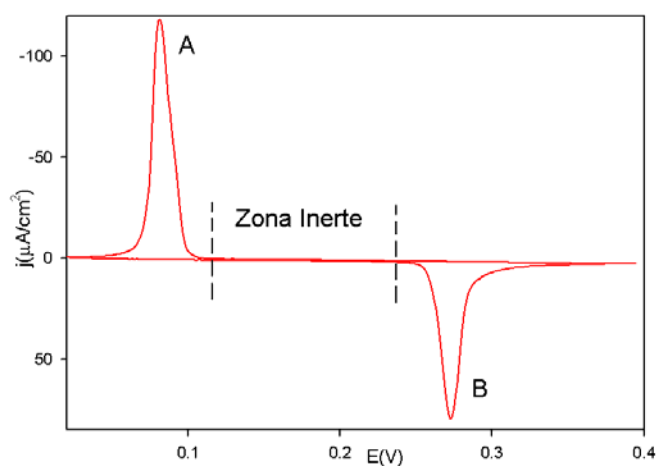
Figure 2.4. Voltagrama de una película delgada de TCNQ sobre carbón vitrificado en una disolución 0.5 M de KCl (aq) a una velocidad de barrido de 1mV/s.

Otra de las características más comunes en las cinéticas regidas por nucleación y crecimiento es que, cambiando el sentido del barrido al pie del pico de reducción o de oxidación, puede verse que, aunque la fuerza conductora (el sobrepotencial) está siendo disminuida, la corriente sigue aumentando, lo que se conoce como "bucle inductivo" [72]. Este incremento en la corriente ocurre porque el área superficial del cristal se incrementa a más velocidad que la disminución del potencial aplicado. En consecuencia, este test puede emplearse como indicativo de una cinética de nucleación y crecimiento.

2.3.1.2 Cronoamperometría

Similarmente a los procesos bidimensionales, las transiciones de fase de

una capa delgada de material orgánico depositada sobre un electrodo sólido presentan una curva cronoamperométrica con un máximo a un tiempo mayor que cero, caracteristico de una cinética dominada por fenómenos de nucleación y crecimiento.

La electrocristalización de una nueva fase sobre un sustrato puede llevar consigo, en los primeros pasos, la formación de núcleos tridimensionales que posteriormente solaparán para dar lugar a la etapa de crecimiento, hasta la completa formación de la nueva fase.

FIGURA 2.5. Curvas cronoamperométricas de TCNQ sobre carbón vitrificado en KCl 0.5M.

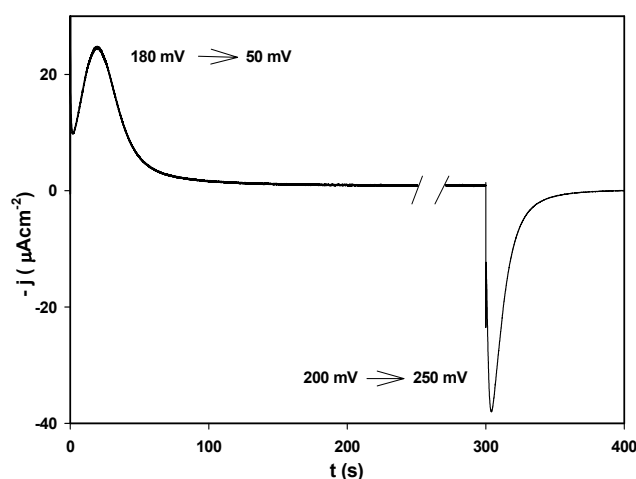Como ejemplo, la Figura 2.5 muestra las curvas obtenidas para el TCNQ en medio KCl [70]. Al aplicar el potencial necesario se produce una supersaturación de la disolución de $K^+[TCNQ]^-$(aq) cerca de la superficie del

electrodo. Como consecuencia de dicha superpersaturacion, precipitan pequeñas cantidades de sólido, que constituyen lo que serán los núcleos para la formación del nuevo sólido. Tras esto, un rápido crecimiento de los núcleos ocurre para minimizar la energía Gibbs del sistema.

Los detalles del origen de la supersaturación están todavía por determinar, sin embargo pueden estar asociados al efecto Gibbs-Thompson [73] según el cual, la solubilidad de una partícula es inversamente proporcional a su radio.

$$kT \ln\left(\frac{c_I}{c_{I_\infty}}\right) = \frac{2\sigma v_{II}}{r} \qquad (2.17)$$

Siendo c_I la solubilidad del cristal de radio r en la disolución, c_{I_∞} la solubilidad de los cristales grandes, σ la tensión interfacial v_{II} el volumen de una molécula en el cristal, y k la constante de Boltzmann.

De acuerdo con esta relación, una pequeña partícula podría producir una concentración que esté supersaturada respecto de otras partículas más grandes. Esta es la base de lo que se llama "la maduración de Ostwald" [74-76], en la que los cristales mas pequeños se disuelven a expensas del crecimiento de cristales más grandes. Así que, por una parte, los cristales pequeños buscan formar cristales más grandes para minimizar la energía Gibbs, mientras que por otra, son más solubles y propensos a disolverse.

La geometría de los núcleos sólidos es sensible a la interacción entre el sustrato y el material depositado. Uno de los modelos más empleados es el que supone un núcleo de forma cónica caracterizado por dos velocidades de crecimiento, k_3^l, de crecimiento radial, y k_3, de crecimiento perpendicular, ambas con unidades de mol·cm^{-2} s^{-1}. Una representación puede verse en la Figura 2.6.
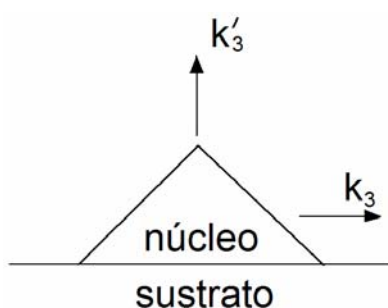
Figura 2.6: Crecimiento de núcleos tridimensionales con geometría cónica.

La corriente total puede ser obtenida a partir de la integración de la contribución de un apilamiento de discos. Aunque hay modelos que consideran geometrías más complejas, como las de Bosco y Rangarajan [77] o Abyaneb y Fleischmann [78], para el objeto de esta tesis es más indicado el tratamiento de geometrías simples, como la cónica, la cual permite deducir expresiones analíticas para la intensidad de corriente generada en estos procesos a potencial constante. En cualquier caso, la solución del problema debe tener en cuenta el solapamiento de los núcleos, ya sea en el caso de nucleación

instantánea, donde el número de núcleos es igual al inicial (N_0) o progresiva, en el que depende del tiempo (A_3t). Las expresiones obtenidas para ambos casos son:

$$I = nFk_3^I\left[1 - \exp\left(-\frac{\pi M^2 k_3 N_0 t^2}{\rho^2}\right)\right] \text{ Para nucleación instantánea} \qquad (2.18)$$

$$I = nFk_3^I\left[1 - \exp\left(-\frac{\pi M^2 k_3 N_0 A_3 t^3}{\rho^2}\right)\right] \text{ Para nucleación progresiva.} \qquad (2.19)$$

Donde n es el número de electrones intercambiados, M es el peso molecular y ρ es la densidad del depósito.

El paso determinante de velocidad en el crecimiento de los núcleos suele ser la etapa de difusión a través del sólido. Sin embargo, si la capa es lo suficientemente delgada y el sobrepotencial aplicado lo suficientemente bajo, esta etapa minimiza su influencia de una manera significativa hasta poder ser despreciada en determinados casos.

Hay varios modelos que simulan el modo en el que la nucleación y crecimiento sobre un sustrato externo tiene lugar, trayendo consigo la formación de un sólido con una morfología y orientación distintas para cada caso. Estas propiedades son primordiales a la hora de estudiar un material, cuya estructura depende de muchos parámetros que aun no están apropiadamente definidos.

En muchas ocasiones, el crecimiento de estos sólidos tiene lugar mediante un mecanismo de capa a capa (layer by layer) [79]. En estos casos, la expansión de los núcleos tridimensionales se ve inhibida por alguna razón, y el crecimiento paralelo a la superficie cesa hasta que no se forman nuevos núcleos. Estos procesos han sido ampliamente discutidos por Abyaneb y Fleischmann [78].
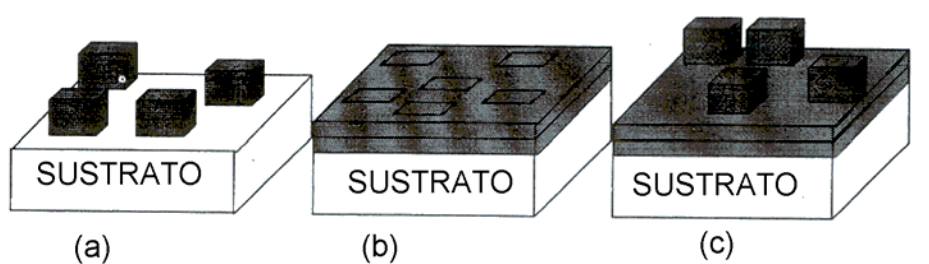
Figura 2.7. Modos de crecimiento sobre un sustrato externo. (a) modelo de Volver-Weber (b) modelo de Frank Van der Merwe (c) modelo de Stranski-Krastanov.

Un aspecto fundamental a estudiar es la dependencia de la sobresaturación y de la energía de adhesión del material a la superficie electródica. Cuando se produce una adhesión débil sólo podrán formarse núcleos tridimensionales, como está predicho por Volver –Weber [80] en el modelo que lleva su mismo nombre. Por el contrario, cuando tiene lugar una adhesión fuerte, se pueden producir dos casos, uno en el que haya pocas diferencias entre las constantes de red del soporte y del sólido depositado, y otra, en la que sea muy significativa esta diferencia.

El primero de estos supuestos, en el que existe baja diferencia, es explicado por el modelo de Frank Van der Merwe [81], con la formación de núcleos bidimensionales seguidos de un crecimiento capa a capa durante toda la evolución del sólido. Sin embargo, en el segundo caso, cuando la diferencia es alta, solo se forman núcleos bidimensionales para las primeras capas, estando las siguientes capas regidas por un crecimiento tridimensional. Este último comportamiento es explicado mediante el modelo de Stranski – Krastanov [82].

2.3.1.2 Medidas de Capacidad frente al Potencial.

El valor de la capacidad de una capa delgada depende tanto de la compactación del material, que influye directamente en el grosor de la misma, como con la constante dieléctrica del sólido depositado. Al igual que para los procesos de transición de fase bidimensionales, en los procesos de nucleación y crecimiento para una capa delgada de material orgánico depositada sobre un electrodo externo se obtienen cambios bruscos de capacidad cuando tiene lugar el proceso electródico.
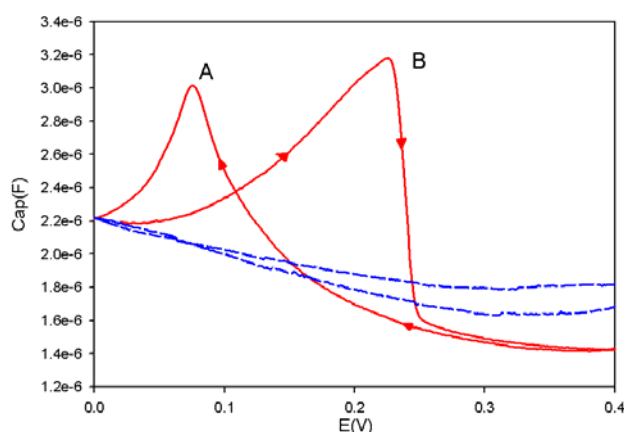
Figura 2.8. Curvas de capacidad para TCNQ sobre Carbón vitrificado (continua) en medio 0.5M de KCl y sin TCNQ depositado sobre el carbón vitrificado (discontinua). El proceso A representa la reducción del TCNQ y el B la oxidación del TCNQ$^-$.

Como puede verse en la Figura 2.8 para el TCNQ depositado sobre carbón vitrificado, se obtienen unas curvas de capacidad en las que se ve que en la oxidación de TCNQ$^-$ a TCNQ hay un cambio muy abrupto, lo que es característico de un proceso de transición de fase. Este tipo de cambios de capacidad están relacionados con cambios pronunciados, tanto de la compactación como de la naturaleza conductora del material. De acuerdo con la ecuación (1.9), un aumento de la capacidad puede deberse a un cambio en la estructura del material depositado sobre el electrodo, que como consecuencia puede afectar tanto a un mayor grado de compactación del material depositado como a las propiedades eléctricas, ya que si la constante dieléctrica del material orgánico aumenta, lo mismo le ocurrirá a la capacidad.

2.4 BIBLIOGRAFÍA.

[1] M. Fleischmann, H.R. Thirsk; Advances in Electrochemistry and Electrochemical Engineering, vol 3 Ed. P. Delahay, Wiley 1963.

[2] J.A. Harrison, H. R. Thirsk; Electroanal. Chem. Vol 5, A.J. Bard Ed. 1972.

[3] K.J. Vetter; Electrochemical Kinetics, Academic Press, 1967.

[4] J.O'M. Bockris, A.R. Despic; The mechanisrn of Deposition; in Physical Chemistry an Advanced Treatise, Adademic Press 1970.

[5] Southampton Electrochemistry Group. Instrumental Methods in Electrochemistry. Cap. 9 Ed. Ellis Horwood. 1990.

[6] R.D. Armstrong; J. Electroanal. Chem. 20 (1969) 168.

[7] S. Flecher; J. Electroanal. Chem. 118 (1981) 419.

[8] Cl. Buess-Herman; J. Electroanal. Chem. 186 (1985) 27

[9] Cl. Buess-Herman; J. Electroanal. Chem. 349 (1993) 93

[10] W. Lorenz; Z.Elektrochem 62 (1958) 192

[11] C. Lee, A. J. Bard; J. Electroanal. Chem., 239 (1988) 441.

[12] A Díaz,A E. Kaifer; J. Electroanal. Chem., 249 (1988) 333.

[13] M. Sánchez-Maestre, R. Rodríguez-Amaro, E. Muñoz, J. J. Ruiz, L. Camacho; J. Electroanal. Chem., 359 (1993) 325.

[14] M. Sánchez-Maestre, R. Rodríguez-Amaro, E. Muñoz, J. J. Ruiz, L. Camacho; Langmuir, 10 (1994) 723.

[15] R. Salas, M. Sánchez-Maestre, R. Rodríguez-Amaro, E. Muñoz, J. J. Ruiz y L. Camacho; Langmuir, 11 (1995) 1791.

[16] N. K. Akherntov, R. I. Kaganovich, B. B. Darnaskin, E. A. Marnbetkaziev; Electrokhimiya, 14 (1978) 1761.

[17] U. Retter, H. Jehring, V. Vetterl; J. Electroanal. Chem., 57 (1974) 391.

[18] U. Retter, H. Lohse; J. Electroanal. Chem., 134 (1982) 243.

[19] R. Sridharan, R de Levie; J. Phys. Chem., 86 (1982) 4489.

[20] T. Wandlowski, E, Kretchmer, E. Müller, F. Kuschel, S. Hoffmann y J. von Lipinski; J. Electroanal. Chem., 213 (1986) 339.

[21] C. Buess-Hermann; Progress in Surface Science, 46 (1994) 335.

[22] R. Guidelli; J. Phys. Chem. 74 (1970) 95.

[23] R.H. Wopschall, I. Shain; Anal. Chem. 39 (1967) 1514, 1527 y 1535.

[24] B. Scharifker, J. Mostany, J. Electroanal. Chem. 177(1984)12 y 25

[25]. E. Bosco, S.K. Rangarajan; J. Chem. Soc. Faraday Trans. 77(1981) 8 y J. Electroanal. Chem. 129(1981)25.

[26] M.Noel, S. Chandrasekaran, C.A Basha, J. Electroanal. Chem. 225 (1987) 93.

[27] A.N. Kolmogoroff; Izn. Akad. Nauk SSSR, Otd. Matem. Estestv. Nauk, 9(1937)355,

[28] M. Avrami, J. Chem. Phys. 7(1939)1103.

[29] M. Avrami, J. Chem. Phys. 8(1940)2l2.

[30] M. Avrami, J. Chem. Phys. 9(1941)177.

[31] S. Sathyanarayana y K. G. Baikerikar; J. Electroanal. Chern., 21 (1969) 449.

[32] T. Wandlowski, R. de Levie; J. Electroanal. Chem., 349 (1993) 15.

[33] T. Wandlowski, B. J. Geoffrey, R. deLevie; J. Phys. Chem., 97 (1993) 10119.

[34] T. Wandlowski; J. Electroanal. Chem., 302 (1991) 233.

[35] R. Philipp, U. Retter, J. Dittrich, E. Muller, F. Kuschel; Electrochim. Acta, 32 (1987) 1671.

[36] R. Srinavasan, R. De Levie; J. Electroanal. Chem., 249 (1988) 321.

[37] T. Wandlowski, L. Pospisil; J. Electroanal. Chem., 270 (1989) 319.

[38] B. Scharifker, C. Werhmann; J. Electroanal. Chem., 185 (1985) 93.

[39] S. Flecher, L. Duff, R. G. Barradas; J. Electroanal. Chem., 100 (1979) 759.

[40] M. D. Ward, Electroanalytical Chemistry; Ed. A. J. Bard, Marcel Dekker; New York.

[41] F. Li, J. Albery; Langmuir, 8 (1992) 1645.

[42] L.M. Peter, J.D. Reid, B.R. Scharifker, J. Electroanal. Chem. 119 (1981) 73.

[43] H. O. Finkleay, D. D. Hanshew; J. Am. Chem. Soc., 114 (1992) 3173.

[44] M. Sánchez-Maestre, R Rodríguez-Arnaro, E. Muñoz, J. J. Ruiz, L. Camacho; J. Electroanal. Chem., 373 (1994) 31.

[45] S. Flecher, L. Duff, R. G. Barradas, J. Electroanal. Chem. 100 (1979) 759.

[46] S. Flecher, C.S. Halliday, D. Gates, M. Westcott, T. Lwin, G. Nelson, J. Electroanal. Chem. 159 (1983) 267.

[47] E. Laviron, Electroanalytical Chemistry Ed. A.J. Bard, Marcel Dekker; New York, 1982; Vol. 12, p. 53.

[48] H. Matsuda, K. Aoki, K. Tozuda; J. Electroanal. Chem., 217(1981) 1 y 15.

[49] A. Bewick, M. Fleischmann, H.R. Thirsk; Trans. Faraday Soc., 58 (1962) 2200.

[50] S. Sathyanarayana, K. G. Baikerikar J. Electroanal. Chem. 21 (1969) 449.

[51] E.V. Stenina, B.B. Damaskin, J. Electroanal. Chem., 349 (1993) 31.

[52] F. G. Thomas, C. Buess-Herrnan y L. Gierst; J. Electroanal. Chern., 214 (1986) 597.

[53] C, Buess-Hermann, Adsorption of molecules at metal electrodes, J. Lipkowski y P. N. Ross Eds., Cap. 2. VCH, New York (1992).

[54] B. B. Damaskin; J. Electroanal. Chem., 21 (1969) 149.

[55] U. Retter; J. Electroanal. Chem., 236 (1987) 21.

[56] T. Wandlowski; J. Electroanal. Chem., 302 (1991) 233.

[57] Y. Kharkats y U. Retter; J. Electroanal. Chem., 287 (1990) 363.

[58] R. Sridharan, R. de Levie, y S. K. Rangarajan; Chem. Phys. Lett., 142 (1987) 43.

[59] B. B. Damaskin, N. K. Akhmetov; Electrokhimiya 15 (1979) 1691.

[60] Y. Kharkats; J. Electroanal. Chem., 115 (1980) 75.

[61] Y. Gurevich, Y. Kharkats; J. Electroanal. Chem. 86(1978) 245.

[62] P. Nikitas y S. Andoniou; J. Electroanal. Chem., 375 (1994) 339.

[63] K. Pushpalatha y M. V. Sangaranarayan; J. Electroanal. Chem., 425 (1997) 39.

[64] T. Wandlowski, G. B. Jameson y R. de Levie; J. Phys. Chem., 97 (1993) 10119.

[65] T. Wandlowski, G. B. Jameson y R. de Levie; J. Electroanal. Chem., 379 (1994) 215.

[66] R. Schöllhorn; Angew Chem. 92(1980) 1015

[67] R. Schöllhorn; W. Schramm; D. Fenske; Angew Chem. Int. Ed. Engl. 19 (1980) 983

[68] R. Schöllhorn; Physica B & C 99 (1980) 89

[69] F. Scholz, B. Meyer; Voltammetry of solid microparticles inmovilized on electrode surfaces. Electroanalytical Chemistry. Vol 20 (1998) A. J. Bard, Marcel Dekker. New York.

[70] A.M. Bond, S. Fletcher, P.G. Symons; Analyst 123 (1998) 1891.

[71] A.M. Bond, S. Fletcher, F. Marken, S.J. Shaw, P.G. Symons; J. Chem. Soc. Faraday Trans., 92 (1996) 3925

[72] S. Fletcher, C.S. Halliday, D. Gates, M. Westcott, T. Lwin, G.Nelson; J Electroanal. Chem., 159 (1983) 267

[73] A.L. Smith; "Particle Growth in Suspensions", Academic Press, London, 1972, 3-28

[74] A.S. Myerson; *"Handbook of Industrial Crystallization"*, Butterworth-Heinemann, Sydney, 1993, 60-61

[75] A. Mersmann; *"Crystallization Technology Handbook"*, Marcel Dekker, Inc, New York, 1995, 374-375

[76] J.W. Mullin; *"Crystallisation"*, Butterworths, Melbourne, 1972, 222-224

[77] E. Bosco, S. K. Rangarajan, *J. Electroanal. Chem.,* 134 (1982) 213.

[78] M. Y. Abyaneh, M. Fleischmann, *J. Electroanal. Chem.,* 119 (1981) 187

[79] A. Milchev; Electrocrystallization. Fundamentals of Nucleation and Growth. Kluwer Academic Publishers 2002.

[80] M.Volmer, A.Weber; Z.Physik.Chem. 119 (1926) 277.

[81] F.C. Frank, J.H. Van der Merwe; *Proc.Roy.Soc* 205 (1949) A198.

[82] E. Budevski, G. Staikov, W.J. Lorenz; *Electrochemical Phase Formation–*

An Introduction to the Initial Stages of Metal Deposition, VCH, Weinheim, 1996.

82

CAPÍTULO III.

EXPERIMENTAL.

84

Reactivos:

Todos los reactivos utilizados durante los ensayos de esta tesis presentaban pureza analítica y fueron usados tal y como fueron recibidos, sin ninguna purificación posterior. Las firmas comerciales que los suministraron son detalladas en el apartado experimental de cada uno de los estudios correspondientes. Para la preparación de las disoluciones acuosas usadas durante esta tesis se usó en todo momento agua ultrapura como disolvente.

Las medidas electroquímicas han sido realizadas con un potenciostato, AUTOLAB PGSTAT30. El electrodo de referencia (Ag/AgCl 3M) y el auxiliar(Pt) han sido suministrados por METHROM. Como electrodos de trabajo se han empleado un estativo de Mercurio (METHROM), para las medidas con electrodo de mercurio y un electrodo de carbón vitrificado. Este último electrodo fue fabricado a mano en el laboratorio ya que el diseño de los electrodos comerciales no se adecuaba a la celda espectroelectroquímica. En este sentido, se adquirieron discos de glassy carbon SIGRADUR de diversos diámetros, los cuales fueron acoplados a diferentes carcasas de teflón para su uso. El pulido de los discos de carbón vitrificado se realizó en primera instancia con papeles de tamaño de grano decreciente. Posteriormente se usó pasta de diamante METKOM para un mayor pulido, y finalmente, se empleó polvo de alúmina de tamaño decreciente desde 1µm hasta 0.025µm para conseguir un

pulido del mayor grado posible. Para limpiar el electrodo tras el pulido se le introdujo en un baño de ultrasonidos durante 5 minutos. Solo el pulido con alúmina de 0.025µm y el baño ultrasónico fueron considerados necesarios entre sucesivos experimentos.

El potenciostato está equipado con un módulo FRA que le permite hacer medidas de impedancia y se ha trabajado a frecuencias variables entre 77 y 477 Hz y una amplitud de 5mV en todos los casos. El registro de las curvas de Capacidad vs Potencial se obtiene mediante el software correspondiente. Se programan pequeños saltos de potencial (1 mV) y, tras esperar a que el sistema alcance el equilibrio, de manera que se eliminen otras componentes capacitativas como la influencia de la doble capa, se realiza la medida de impedancia. Posteriormente, esta medida de impedancia es convertida a datos de capacidad.

Medidas espectroelectroquímicas.

Se ha empleado un montaje de espectroelectroquímica por reflectancia similar al representado en la Figura 3.1:

La celda electroquímica, además de alojar el sistema de tres electrodos debe ser adecuada para la incorporación del componente que permita la medida espectroscópica. En este sentido, ha resultado fundamental el empleo de una sonda de fibra óptica. Ésta consiste en múltiples fibras ópticas bifurcadas que permiten la obtención de medidas espectroelectroquímicas de

reflexión, con incidencia normal sobre el electrodo de trabajo, así como otro conjunto de fibras ópticas que permitan llevar de vuelta la luz reflejada al detector. La gran ventaja de estas celdas reside en la posibilidad de utilizar electrodos de muy diferente naturaleza, incluyendo el electrodo de mercurio y el de carbón, que son de los más usados en electroquímica. Así, emplazando la sonda de manera que incida de manera normal a la superficie del electrodo, se consigue una celda de espectroelectroquímica de una manera simple y con bajo costo, permitiendo capturar los espectros de las especies que se encuentran, bien sobre la superficie del electrodo, o bien en el camino entre la sonda y el electrodo.
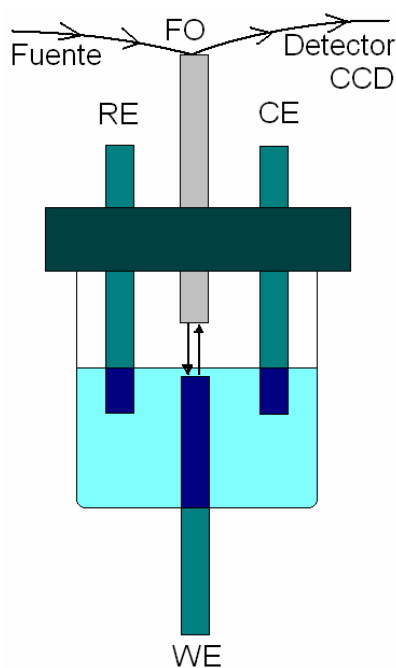

Figura 3.1: Esquema del dispositivo experimental para las medidas espectroelectroquímica por reflectancia.

El control del potencial en las medidas espectroelectroquímicas es idéntico al usado para las medidas electroquímicas. La única técnica electroquímica acoplada a la espectroscopia UV-Vis durante la realización de esta tesis ha sido la cronoamperometría. El objeto de acoplar estas dos técnicas, cronoamperometría con espectroscopia UV-Vis, ha sido obtener un espectro correspondiente debido a los cambios de potencial sobre el electrodo de carbón vitrificado, de manera que tras el salto potenciostático, los espectros pudieran ser recogidos periódicamente, y así poder analizar su evolución temporal, y no solamente en los instantes inmediatamente posteriores al salto. Estos datos permitirán buscar posibles cambios en el transcurso de la escala de tiempo, con el objeto de conseguir evidencias que indiquen la presencia de especies que se comporten como intermedios de reacción durante el salto potenciostático. En todo caso, la espectroelectroquímica ha sido usada únicamente con carácter cualitativo, y nunca cuantitativo, debido a la irreproducibilidad de los electrodos usados a lo largo de las experiencias.

El espectrofotómetro utilizado para realizar las medidas espectroscópicas es un equipo modular fabricado por Ocean Optics Europe, Inc. Éste consta de una fuente de luz DH-2000 que combina dos lámparas, una halógena y otra de deuterio, abarcando la zona espectral entre los 250 y los 860 nm. Una sonda de fibra óptica de 200 μm de diámetro interno conduce la luz hasta la superficie del electrodo de carbón vitrificado, donde el rayo de luz incidente es reflejado y vuelve a través de la misma sonda para ser transmitida hasta el detector, sin que sea necesario el uso de ningún tipo de elemento

óptico entre la sonda y la muestra. El detector, un AVS-SD2000, Ocean Optics Europe Inc. consta de una red de difracción de 600 líneas/mm y una batería lineal CCD con 2048 elementos. El control del instrumento fue realizado mediante el programa AVASPEC suministrado con el equipo.

Debido a la incidencia de la luz UV-Vis sobre el electrodo durante la medidas, es posible un calentamiento de las inmediaciones del electrodo alojado en la celda electroquímica. Para evitar fluctuaciones en la temperatura es imprescindible en el sistema una correcta termostatización, para lo que se ha contado con una celda electroquímica termostatizada mediante un termostato SELECTA con una oscilación de temperatura de ±0.1ºC. Igualmente, este termostato fue usado durante las medidas electroquímicas cuando el ensayo lo requirió como necesario.

Preparación de películas delgadas.

Para la inmovilización de partículas sobre el electrodo, con el objetivo de preparar una película delgada, se ha usado la la técnica de casting. Ésta consiste en depositar un volumen conocido de disolución del material en estudio en un disolvente volátil adecuado, el cual, al evaporarse deja como residuo el compuesto previamente disuelto. Se obtiene, así, una película delgada de varios μm de espesor, adherida a la superficie del electrodo. Una condición necesaria para poder utilizar esta técnica es que la sustancia en estudio tenga buena adherencia con el material empleado como soporte. Una

vez inmovilizadas la micropartículas, el electrodo es introducido en la disolución, y su modo de empleo es similar al de un electrodo modificado, por lo que su manejo es tan simple como eficaz. La ventaja de esta técnica, frente a otras descritas, es el conocimiento exacto de la cantidad de materia depositada, con el simple control de la concentración del volumen de disolución preparado, y del volumen depositado.

Tratamiento de Datos.

Todos los datos obtenidos a partir de las experiencias electroquímicas y espectroelectroquímicas fueron adquiridos de manera digital. Para el tratamiento de estos datos fueron usados tanto el software propio del instrumento como los programas Sigma Plot 10 [1] y Mathcad 2001i [2]. Sigmaplot fue usado principalmente para la representación gráfica y para el tratamiento de datos de electroquímica y espectroelectroquímica; mientras que Mathcad fue empleado para el desarrollo de los modelos matemáticos de nucleación y crecimiento presentados en siguientes apartados.

Bibliografía:

[1] SigmaPlot 10.0. Copyright © 2006 Systat Software

[2] Mathcad 2001i Professional. Mathsoft. Cambridge. MA 02142. USA.

CAPÍTULO IV. TRANSICIONES DE FASE BIDIMENSIONALES DE VIOLÓGENOS SOBRE ELECTRODO DE MERCURIO.

Capitulo V   Transiciones de fase bidimensionales sobre electrodo de carbón vitrificado.

92

4.1 FORMATION OF A 2D PHASE IN THE ELECTROCHEMICAL REDUCTION OF 4,4′-BIPYRIDINE ON MERCURY IN THE PRESENCE OF IODIDE IONS VIA A DESORPTION–NUCLEATION, REORIENTATION–NUCLEATION MECHANISM

Abstract

This paper reports new experimental evidence of the electrochemical formation of a 2D phase which, based on a recently developed model, takes place via a desorption–nucleation mechanism that includes the incorporation of adsorbed molecules into the condensed phase.

1. Introduction

Two-dimensional (2D) phase transitions on electrode surfaces have been widely investigated in recent years [1–3] on account of the fact that the compact monolayers they form can take part in a large number of major electrochemical processes including electrocatalysis, corrosion inhibition, biosensing or the construction of electro-optical devices.

Chronoamperometry has proved the most suitable technique for characterizing electrochemical 2D nucleation processes; also, special mathematical models have been developed that account accurately for the behaviour of a wide variety of real systems [2,4–7]. In recent work [8], we reported a new mathematical model based on a desorption–nucleation, reorientation–nucleation mechanism that was successfully applied to the 2D nucleation of heptyl viologen in the presence of adsorbed anions on a mercury electrode.

In this work, we examined a new real system (*viz.* the electrochemical reduction of 4,4′-bipyridine on mercury in the presence of iodide ions) that is also accurately explained by the proposed mathematical model.

2. Experimental

4,4′-Bipyridine (Bpy) was supplied by Lancaster and its solutions made in IH (Fluka) at pH 1.5. The final iodide concentration was adjusted to 0.1 M with KI (Merck r.a. grade). All solutions were prepared in Milli-Q water.

Electrochemical recordings were obtained by using a PGSTAT 30 potentiostat/galvanostat from Autolab equipped with a scan-gen module and an FI20 integration module. The working electrode was a Metrohm 663 V Stand HMDE with a surface area of 0.384 ± 0.005 mm^2, the auxiliary electrode Pt and the reference electrode Ag|AgCl. All measurements were made in a nitrogen atmosphere and the temperature was measured to within $\pm$ 0.1 ºC in all instances.

3. Results and discussion

Fig.1 shows a cyclic voltammogram obtained for 1 mM Bpy on an Hg electrode in the presence of 0.1 M I$^-$ at pH 1.5; a scan rate of 50 mV s^{-1}, a temperature of 15 ºC and potentials over the range -500 to -600 mV were used. As can be seen, the cathodic scan exhibits three narrow peaks designated A_1, B_1 and D_1, and the reverse (anodic) scan the corresponding oxidation peaks (A_2, B_2 and D_2). These peaks are only observed below pH 3 and above a 0.3 mM concentration of Bpy; also, their shape is consistent with an electrode process involving immobilized molecules at an electrode. The nature of these peaks, including the influence of the scan rate, temperature and Bpy concentration on their properties [*viz.* peak potential (E_p), peak current (I_p) and peak half-width (W)], was analyzed elsewhere [9]]. In this work, we only examined the *j–t* curves corresponding to process A_1. The charge exchanged with the electrode, which was obtained by integrating peak A_1 or A_2, was *ca.* 10 $\pm$ 1 µC cm^{-2}.
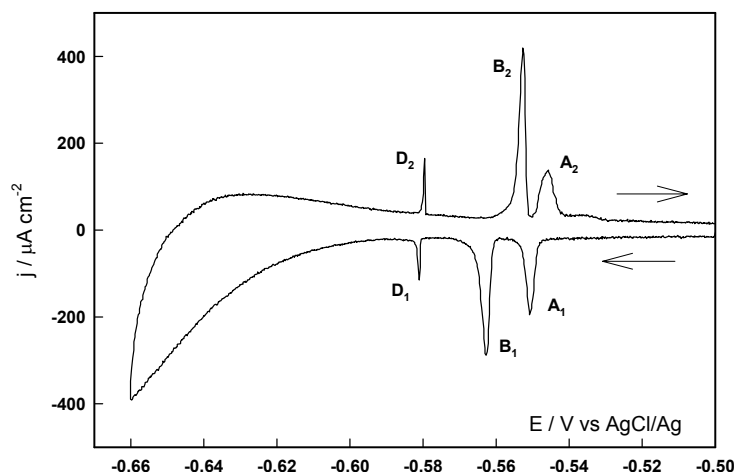
Figure 1. Voltammograms obtained for 1 mM $BpyH_2^{2+}$ in the presence of 0.1 M I^- at pH 1.5. v = 50 mV s^{-1}; T = 15 ºC

Fig. 2 (circles) shows the *j–t* curves recorded under the same experimental conditions as in Fig. 1. The curves were experimentally obtained by applying an initial potential E_0 = –500 mV, followed by a potential pulse up to a potential immediately following that of appearance of peak A_1. The final potential of each potentiostatic jump is shown in the figure. The experimental data fit no straightforward mathematical nucleation–growth–collision (NGC) model [4,10,11] owing to the presence of strongly adsorbed I^- anions, which hinder the adsorption of Bpy molecules, so such anions must be at least partly displaced from the electrode. Other attempts at fitting the experimental *j-t* curves to various treatments such as that of Retter et al. [12], which considers a nucleation process following an exponential law in combination with a surface diffusion controlled growth, and reported models for nucleation and adsorption mixed processes such as those of Rangarajan et al. [13, 14] and Guidelli et al [6], yielded poor results in all cases.
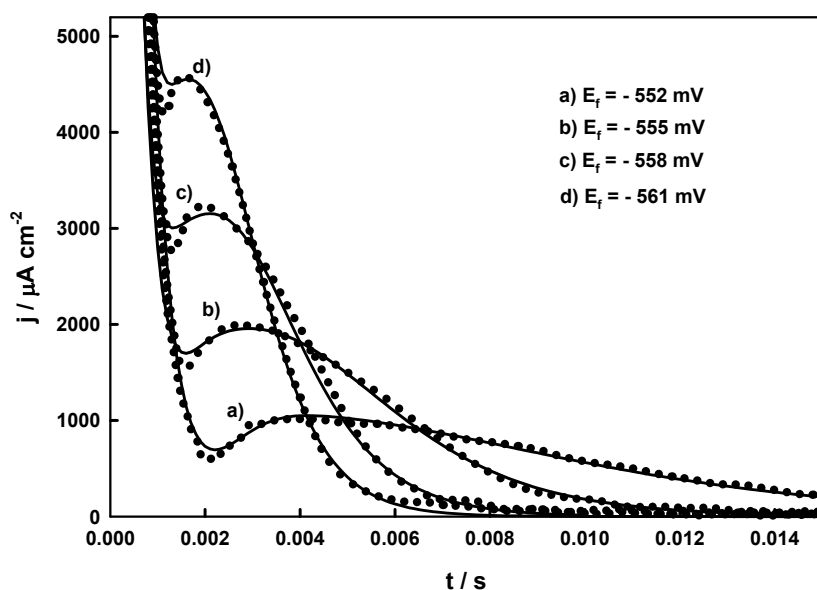
Figure 2. Experimental j–t curves recorded at T = 15 °C (circles). The potential applied before the jump was 500 mV. The final potential for each curve is shown in the figure. Solid lines correspond to the simulations done with the model based on Eq. (10).

The shape of the j–t curves in Fig. 2 resembles that of the curves for heptyl viologen (HV) in the presence of Br⁻ and SO_4^{2-} ions, which were examined in recent work [8]. With HV, the formation of condensed phases by salts of its cation radical on a mercury electrode under potentiostatic conditions was found to be explained by a mathematical model based on a desorption–reorientation–nucleation mechanism.

A preliminary test can be performed by assuming that, based on the well-known Bewick–Fleischmann–Thirsk (BTF) model [4,10], the current density $j_{2D}(t)$ for such a process can be expressed in simple mathematical terms:

$$j_{2D}(t) = n\beta q_m t^{n-1} \exp(-\beta t^n) = q_m \frac{dS}{dt} \qquad (1)$$

where q_m is the total charge involved in the phase transition and usually corresponds to a monolayer, β is a parameter related to the nucleus growth rate and n is a constant dependent on the nature of the nucleation process.

Application of the Avrami theorem [15–17] in this situation yields

$$S = \frac{1}{q_m}\int_0^t j_{2D}dt = 1 - \exp(-S_x) = 1 - \exp(-\beta t^n) \tag{2}$$

where S_x is the expanded area (*i.e.* excluding overlap).

S_x can be calculated by integrating the experimental j–t curves at each intermediate t value used in the experiment. Equation (2) can be rewritten as

$$\ln(\beta) + n\ln(t) = \ln\left[-\ln(1-S)\right] \tag{3}$$

so

$$n = \frac{\partial \ln\left[-\ln(1-S)\right]}{\partial \ln(t)} \tag{4}$$

By way of example, Fig. 3 shows the plot of n *vs* t obtained from the experimental j–t curve (a) in Fig. 2. As can be seen, n is *ca.* 2 at short times and gradually tends to unity at longer times.
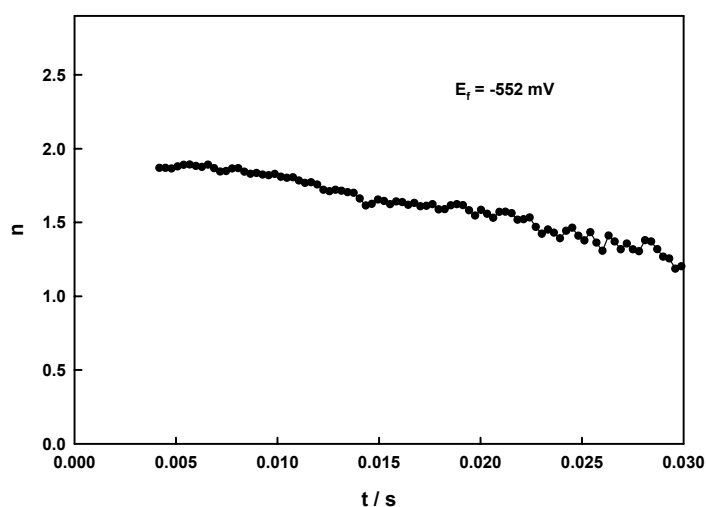
Figure 3. Plot of n against t obtained from the experimental j–t curve (a) in Fig. 2.

Non-integer n values ranging between 1 and 2 have been justified [18, 19] using the treatment of Retter et al. [12]; however, as noted earlier, our j-t curves do not fit this model closely. Therefore, we analyzed the experimental data using the mathematical model based on a desorption–reorientation–nucleation mechanism reported in previous work [8]. This mathematical model relies on the following assumptions: (*i*) Initially, a potential E_0 prior to the nucleation at which adsorption occurs is applied to the electrode. The initial electrode coverage is thus given by θ_0, which can be non-zero. In the studied system, the initially adsorbed material on the electrode surface may be formed by specific adsorption of anions from the background electrolyte, or by $BpyH^{2+}$-counterion pairs. This latter possibility seems to be the more likely. (*ii*) An adsorption–desorption kinetics is established upon application of the potential pulse $E_0 \rightarrow E_f$ before equilibrium is restored. (*iii*) Molecules randomly adsorbed on the

electrode surface forming ion-pairs cannot be electroactive. (*iv*) Molecules can be incorporated into the nuclei via two possible mechanisms, *viz.* desorption of previously adsorbed material and/or reorientation of the molecules on the periphery of the previously formed nuclei.

Therefore, if $\theta(t)$ is the time-dependent surface coverage by $BpyH^{2+}$–counterion pairs (or by anions from the background electrolyte) randomly adsorbed, and $S(t)$ is the time-dependent surface coverage by molecules involved in the nucleation and growth (NG) process, then the corresponding adsorption–desorption kinetics will conform to the following expression:

$$\frac{d\theta}{dt} = k_d(1 - S_1 - \theta) - k_i\theta - k_r\theta(1 - \theta) \tag{5}$$

where k_d and k_i are the rate constants for the adsorption and desorption of I^- and/or $BpyH^{2+}$–counterion pairs, and k_r is the rate constant for the reorientation of $BpyH^{2+}$.

If overlap between neighbouring sites is considered using the Avrami theorem [15–17], then, according to Noel *et al.* [20], surface coverage by randomly adsorbed molecules will be given by

$$S_1 = (1 - \theta)(1 - \exp(-S_x)) \tag{6}$$

In previous work [9], we obtained experimental *C–E* curves which revealed that adsorption was high ($\theta_0 \approx 1$) prior to nucleation (*viz.* at a high E_0 potential value prior to the ΔE jump) (see fig. 4 in Ref. [9]). Accordingly, $k_d \gg k_i$. In the discussion that follows, this assumption (*viz.* that desorption would not occur if

previously formed nuclei did not displace adsorbed material) is assumed to hold

beyond the potential jump. Under this assumption, one can expect $S + \theta \approx 1$,

so

$$\frac{j_{2D}}{q_m} = \frac{dS}{dt} = (1-\theta)\frac{dS_x}{dt}e^{-S_x} - \frac{d\theta}{dt}(1-e^{-S_x}) \approx -\frac{d\theta}{dt} \tag{7}$$

The relation on the right-hand side does not hold at very short times as a

result of the overall process being controlled by nucleation rather than by

desorption; as can be seen from Fig. 3, $n \approx 2$ under these conditions, so one

can write

$$S_x = \beta t^2 \tag{8}$$

This approximation was previously utilized by Rangarajan et al. [14] under

competitive nucleation–adsorption conditions. Although, as suggested by

Guidelli et al. [6], the nucleation kinetics of real systems must change over time,

this will have no appreciable effect on the final shape of our j–t curves as the

relation on the right-hand side of Eq. (7) will hold during must of the process.

The differential Eq. (5) can be readily solved numerically by using the

fourth-order Runga–Kutta method in conjunction with Eqs. (6) and (8). The

results, θ (t), are substituted into Eq. (7) to obtain $j_{2D}(t)$.

The initial decay in the j–t curves of Fig. 2 is due to the double layer

current, which can be expressed as

$$j_{dl}(t) = k_1 \exp(-k_2 t) \tag{9}$$

so the total transient current can be obtained by adding up the two terms:

$$j(t) = j_{dl}(t) + j_{2D}(t) \qquad\qquad (10)$$

Fig. 2 (solid lines) shows the results of the non-linear analysis of Eq. (10) made by fitting the experimental transient (circles). As can be seen, the fit is quite good. Table 1 shows the figures of merit for the fitting at each E_f value. In all cases, $k_d \gg k_i$, so the electrode is virtually completely covered initially (*i.e.* $\theta_0 \approx 1$). It should be noted that k_d values are not significant as one can obtain good fits provided $k_d \gg k_i$, whichever the absolute value of k_d. We chose to use a constant k_d value for all transients in each test series. Also, β is dependent on k_d, so the greater is the latter the greater will be β. Therefore, the absolute value of β is also insubstantial.

By way of example, Fig. 4 shows the contributions of the two terms of *j(t)* given in Eq. (10) for the experimental curve (a) in Fig. 2. As can be seen, the term due to the double layer is fast. A potential appreciable influence of the desorption step on this term can be excluded as the amount of charge exchanged in the nucleation process, q_m, was virtually constant (10.5 ± 0.1 μC cm^{-2}) at any E_f value and very similar to that obtained by integrating voltammetric peak A_1.
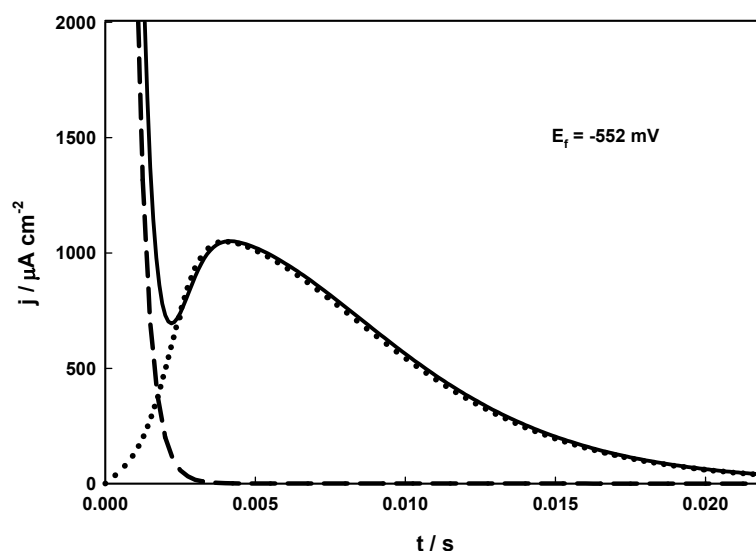
Figure 4. Simulation (solid line) of the experimental *j-t* curve (a) in Fig. 2 done with the model based on Eq. (10). The individual contributions of the double layer (dashed line) and nucleation (dotted line) are also shown.

Such a q_m value is much greater than the theoretical value for a full monolayer of $BpyH_2^{\cdot+}$ lying parallel to the electrode (such species would take *ca.* 72 $\mathring{A}^2$ molecule^{-1}). So, as noted in our previous paper [9], a mixed phase might be formed after the appearance of voltammetric peak A_1 (potential zone II in ref [9]). In such a phase, a $BpyH_2^{\cdot+}$- $BpyH_2^{2+}$ mixed valency complex should be formed that would be in direct contact with the electrode, I^- acting as the counter-ion. In this way, the mixed 2D phase would have an area of *ca.* 140 $\mathring{A}^2$ per $BpyH_2^{\cdot+}$ molecule, which would be equivalent to a charge density of *ca.* 11 C cm^{-2} (*i.e.* similar to that obtained from voltammetric peak A_1).

The contribution of the reorientation term can be estimated from λ, which is defined as [8]:

$$\lambda = \frac{k_r}{k_i + k_r} \tag{11}$$

As can be seen from Table 1, the reorientation rate constant is higher than the desorption rate constant, so $\lambda > 0.5$ (*i.e.* the reorientation term contributes significantly to the formation of the condensed phase). This λ value appears to confirm that the more strongly the counter-ion is adsorbed on the electrode surface, the lower is k_i relative to k_r and the higher is λ as a result. Thus, for heptyl viologen [8], $\lambda < 0.5$ in a sulphate medium and $\lambda \approx 0.5$ in a bromide medium; for Bpy in an iodide medium (*i.e.* in this work), $\lambda > 0.5$, which is consistent with the higher tendency of the anion to be adsorbed on the electrode surface in the sequence iodide > bromide > sulphate [21].

Table 1. Figures of merit of the mathematical fitting of the experimental curves of Fig. 2 to the proposed model, based on Eq. (11). k_d was fixed at 9000 s^{-1}.

E_f / V	$k_1 \cdot 10^{-4}$ / µAcm^{-2}	k_2 / s^{-1}	k_i /s^{-1}	k_r /s^{-1}	ß·10^{-5} / s^{-2}
−0.552	3.0	2500	110	140	4.5
−0.555	3.5	2750	150	380	10.0
−0.558	4.1	3050	200	700	17.0
−0.561	4.7	3300	270	910	22.0

Fig. 5 shows the variation of constant k_r with the final potential of the potentiostatic pulse. This plot is interesting as its extrapolation to $k_r = 0$ allows one to obtain the standard potential for the phase formation, E^0 [8]. As can be seen, $E^0 \approx -551$ mV.
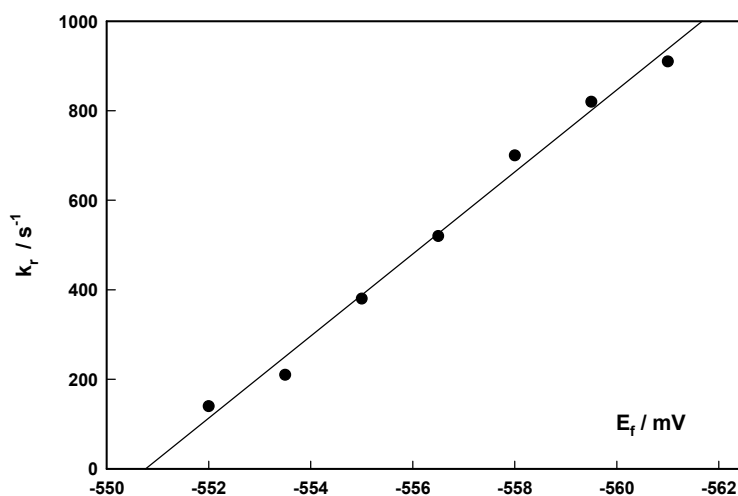
Figure 5. Plot of k_r against the final potential of the potentiostatic jump obtained from the simulated curves in Fig. 2.

4. Conclusions

The first step in the reduction of Bpy on mercury in the presence of iodide as counter-ion in an acid medium at 15 ºC, which involves the $BpyH_2^{2+}/BpyH_2^+$ couple, leads to the formation of a 2D phase the chronoamperometric behaviour of which can be explained in the light of a recently developed mathematical model that assumes a desorption–nucleation mechanism involving molecular reorientation. The results obtained in this work are consistent with an increase in the contribution of the reorientation term to the formation of the condensed phase with increase in the strength with which the anion is adsorbed on the electrode surface.

Acknowledgements

References

[1] E. Budevski, G. Staikov, W.J. Lorenz, Electrochemical Phase Formation and Growth, VCH, Weinheim, 1996.

[2] R. Rodríguez-Amaro, J.J. Ruiz, In: H.S. Nalwa (Ed.), Handbook of Surfaces and Interfaces of Materials, Vol. 1, Academic Press, 2001, p. 660.

[3] Th. Wandlowski, Encyclopedia of Electrochemistry, VCH–Wiley, Weinheim, 2002

[4] M. Fleischmann, H.R. Thirst, In: P. Delahay, (Ed.), Advances in Electrochemistry and Electrochemical Engineering, Vol. 3, Interscience, New York, 1963.

[5] J.A. Harrison, H.R. Thirst, In: A.J. Bard, (Ed.), Electroanalytical Chemistry, Vol. 5, Marcel Dekker, New York, 1977.

[6] R. Guidelli, M.L. Foresti, M. Innocenti, J. Phys. Chem. 100 (1996) 18491.

[7] M. Innocenti, M.L. Foresti, A. Fernández, F. Forni, R. Guidelli, J. Phys. Chem. 102 (1998) 9667.

[8] J.I. Millán, J.J. Ruiz, L. Camacho, R. Rodríguez-Amaro, Langmuir 19 (2003) 2338.

[9] M. Sánchez-Maestre, R. Rodríguez-Amaro, E. Muñoz, J.J. Ruiz, L. Camacho, Langmuir 10 (1994) 723.

[10] A. Bewick, M. Fleischmann, H.R. Thirsk, Trans. Faraday Soc., 58 (1962) 2200.

[11] W. Obretenov, I. Petrov, I. Nachev, G. Staikov, J. Electroanal. Chem., 109 (1980) 195.

[12] R. Philipp, J. Dittrich, U. Retter, E. Muller, J. Electroanal. Chem., 250 (1988) 159.

[13] E. Bosco, S.K. Rangarajan,. *J. Chem. Soc., Faraday Trans. I*, 77 (1981) 1673.

[14] B. Bhattacharjee, S.K. Rangarajan, *J. Electroanal. Chem.*, 302 (1991) 207.

[15] M. Avrami, J. Chem. Phys., 7 (1939) 1103.

[16] M. Avrami, J. Chem. Phys., 8 (1940) 212.

[17] M. Avrami, J. Chem. Phys., 9 (1941) 177.

[18] Th. Wandlowski, J.X. Wang, O.M. Magnussen, B.M. Ocko, *J. Phys. Chem.*, 100 (1996) 10277

[19] M. Van Krieken, C. Buess-Herman, *Electrochim. Acta*, 43 (1998) 2831.

[20] M. Noel, S. Chandrasekaran, C. Ahmed Basha, *J. Electroanal. Chem.*, 225 (1987) 93.

[21] B.E. Conway, *Electrochim. Acta*, 40 (1995) 1501

4.2. CHRONOAMPEROMETRIC STUDY OF THE FILMS FORMED BY 4,4′-BIPYRIDYL CATION RADICAL SALTS ON MERCURY IN THE PRESENCE OF IODIDE IONS: CONSECUTIVE TWO-DIMENSIONAL PHASE TRANSITIONS

Abstract

This paper reports a new mathematical model for consecutive two-dimensional phase transitions that accounts for the chronoamperometric behaviour observed in the formation of electrochemical phases by 4,4′-bipyridyl cation radical ($BpyH_2^{.+}$) on mercury in aqueous iodide solutions. Also, a new interpretation for the *induction time* is proposed.

Introduction

The formation of two-dimensional (2D) phases on electrode surfaces has been the subject of much research in recent years. [1–3] Interest in this topic has been aroused by the fact that the resulting compact monolayers can take part in a number of consequential electrochemical processes such as electrocatalysis, corrosion inhibition, biosensing or electrooptical detection. Two-dimensional nucleation processes can be characterized using various techniques of which chronoamperometry has proved the most suitable [2].

4,4′-Bipyridine (Bpy) and its alkyl derivatives, known as "viologens", constitute an interesting group of substances capable of forming condensed 2D phases under different conditions [4–19]. In previous work [12], our group found the electrochemical reduction of 4,4′-bipyridine on mercury in the presence of iodide ions to result in the formation of 2D phases involving the cation radical $BpyH_2^{\cdot+}$. The cyclic voltammograms obtained exhibited up to three different peaks depending on the particular temperature and reactant concentration. However, the chronoamperometric study exposed a complex behaviour that cannot be accurately described by available models. Recently, our group developed a mathematical model [20] based on a desorption–nucleation, reorientation–nucleation mechanism that accounts for the behaviour of this system provided the phase formation processes involved are well resolved (below 18 ºC) [21].

In this work, a new mathematical model was developed that accounts for the experimental current transients observed when the phase formation

111

processes are strongly overlapped (above 18 ºC). Based on the results provided by the model, a general mechanism for the phase formation process is proposed.

Experimental Section

4,4′-Bipyridine was supplied by Lancaster and its solutions made in HI (Fluka) at pH 1.5. The final iodide concentration was adjusted to 0.1 M with KI (Merck r.a. grade). All solutions were made in bidistilled water from a Millipore Milli-Q system and de aerated by bubbling gaseous nitrogen through them.

Electrochemical recordings were obtained by using a PGSTAT 30 potentiostat/galvanostat from Autolab equipped with a Scan-Gen module and an FI20 integration module. The working electrode was a Metrohm 663 V Stand HMDE with a surface area of 0.384 ± 0.005 mm^2, the auxiliary electrode Pt and the reference electrode Ag|AgCl. All measurements were made in a nitrogen atmosphere and the temperature was measured to within± 0.1 ºC in all instances.

Simulations were done using Mathcad 2001i software.

Results and Discussion

Figure 1*a* shows a selected cyclic voltammogram obtained for 1 mM Bpy on an Hg electrode in the presence of 0.1 M I⁻ at pH 1.5, using a scan rate of 50 mV/s, a temperature of 15 ºC and potentials over the range –500 to –660 mV.

As can be seen, the cathodic (forward) scan provided three narrow peaks (A_1, B_1 and D_1), and the anodic (reverse) scan the corresponding oxidation peaks (A_2, B_2 and D_2). These peaks are only observed at pH < 3 and Bpy concentrations above 0.3 mM; also, their shape is typical of electrode processes involving immobilized molecules at an electrode. The increased current density observed at the most negative potentials corresponds to the electrode process controlled by reagent diffusion. This is consistent with a one-electron process, and like peak D_1, is not analyzed in this work. Above 18 °C, peaks A and B merge into a single one, C, in both the cathodic and anodic scans (see Fig. 1*b*, obtained at *T* = 25 °C).
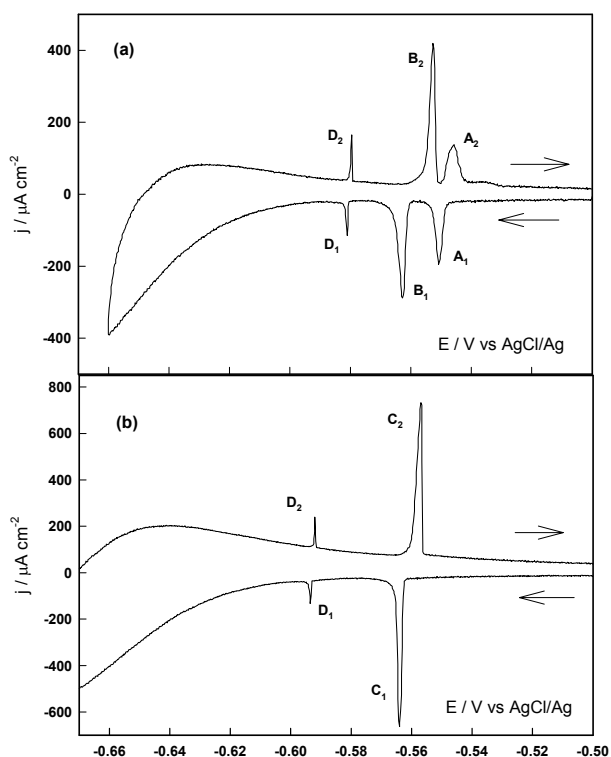

Figure 1. Voltammograms obtained for a 1 mM solution of $BpyH_2^{2+}$ in 0.1 M I^- at pH 1.5, using a scan rate of 50 mV/s and a temperature of (*a*) 15 °C and (*b*) 25 °C.

The amount of charge exchanged with the electrode, calculated by integrating the peaks, was *ca.* 10 ± 1 and 15 ± 1 µC cm^{-2} for peak A_1 and B_1, respectively, below 18ºC, and 24 ± 1 µC cm^{-2} for peak C_1 above 18 ºC. These peaks have been assigned to the formation of 2D phases. The way they are influenced by the scan rate, temperature and Bpy concentration was examined elsewhere [12].

The chronoamperometric study was started by recording *j–t* curves under the conditions of Fig. 1*a* (*i.e. T* < 18 ºC). Tests were performed using the double potential step technique. In the first step (jump), the potential was raised from E_0 = –500 mV (*i.e.* a more positive value than that of appearance of voltammetric peak A_1) to E_1 (a value in between those for peaks A_1 and B_1) and the system was allowed to a stand for a time τ long enough for the current to drop to zero. Then, a new (second) step from E_1 to E_2 (a more negative value than the offset of peak B_1) was performed.

By way of example, Fig. 2 shows the experimental results (circles) obtained with E_0 = –500 mV, E_1 = –552 mV, τ = 15 ms and E_2 = –564 mV. As can be seen, each transition clearly exhibits the typical current peaks for 2D phases.
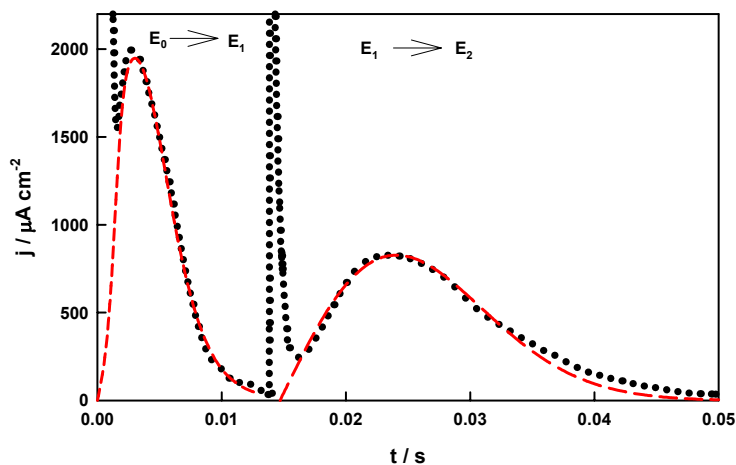
Figure 2. Experimental double-potential step j–t curves obtained at T = 15 ºC (circles). A potential E_0 = –500 mV was applied before the first step. E_1 was –552 mV and E_2 –564 mV. The dashed lines represent the simulated results provided by the model based on eq. (13) for the first step and on eq. (1) for the second.

The j–t curves for the first step were analyzed in previous work [21]. The chronoamperometric behaviour of this system can be explained in the light of a mathematical model that assumes a desorption–nucleation mechanism involving molecular reorientation and is described later on.

The j–t curves for the second step (process B$_1$) closely conform to the well-known Bewick–Fleischman–Thirsk (BFT) classical model for 2D nucleation and growth [22,23] for an instantaneous case:

$$j_{2D}(t) = 2k_3 q_m t \exp\left[- k_3 t^2\right] \tag{1}$$

where k_3 is a coefficient combining the rates of nucleation and growth and q_m the amount of charge involved in the phase transition. The dashed lines in Fig. 2 show the results of the simulations for the two steps.

Figure 3 (circles) shows selected single-potential step j–t curves obtained under the same experimental conditions as Fig. 1b (T = 25 ºC). The curves were recorded by applying an initial potential E_0 = –500 mV that was followed by a pulse up to a value immediately above that of appearance of peak C_1. The final potential of each potentiostatic step is shown in the figure. As can be seen, the initial falling portion, which corresponded to the double layer current, is followed by a maximum typical of a nucleation process; however, the shape of the curves is complex as a result of the two simultaneous nucleation phenomena.
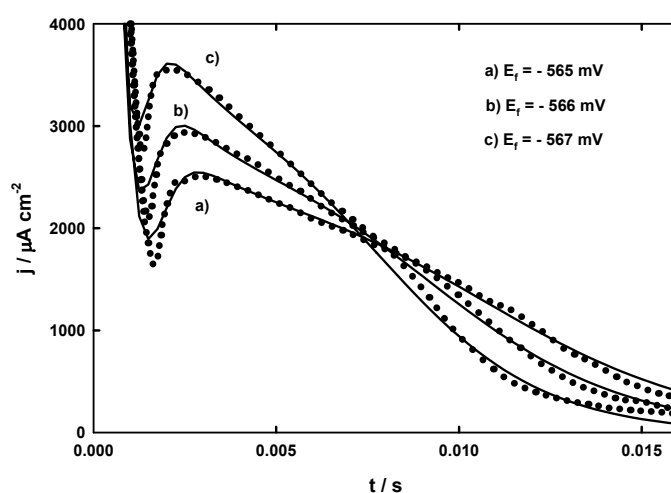
Figure 3. Experimental single-potential step j–t curves obtained at T = 25 ºC (circles). A potential E_0 = –500 mV was applied before the jump. The final potential for each curve is shown. The solid lines represent the simulated results provided by the model based on eq. (10).

One can reasonably assume the processes occurring above 18 ºC to be closely related to those described for the previous cases (T < 18 ºC). Thus, process C_1 results from the overlap of A_1 and B_1. If the phase formation

processes that give peaks A_1 and B_1 were independent, then the current density of peak C_1 should coincide with the combined current densities for the two individual processes. This procedure was previously employed by authors such as Palomar-Pardavé *et al.* [24] and Randriamahazaka *et al.* [25], who assumed the total transient to be a combination of several (2 or 3) types of nucleation processes taking place in a simultaneous manner. Our data, however, do not fit such a simple model; this makes it impossible to simulate peak C_1 by combining the current densities for processes A_1 and B_1. In order to be able to interpret our experimental results, we assumed phase B_1 to form consecutively to A_1 and developed a mathematical model for its chronoamperometric study.

The proposed model

The current density for a 2D transition on a homogeneous (Hg) electrode can be expressed as

$$j(t) = q \cdot F(t) \tag{2}$$

where q is the amount of Faradaic or capacitive charge involved in the transition and $F(t)$ a time function the explicit form of which will depend on the nature of the nucleation and growth mechanism. Thus, for the BFT model [22,23],

$$F(t) = n\beta t^{n-1} \exp(-\beta t^n) \tag{3}$$

where β is a parameter related to the nucleus growth rate, and n is 2 and 3 for instantaneous and progressive nucleation, respectively.

With surface diffusion-controlled growth [26,27],

$$F(t) = K_n \exp\left[-K_g t - \frac{1}{K_n}\left[1 - \exp(-K_n t)\right]\right] \cdot \left[1 - \exp(-K_n t)\right] \qquad (4)$$

K_n and K_g being two constants related to the nucleation and growth process, respectively.

Other nucleation mechanisms do not allow an analytical expression for $F(t)$ to be obtained. Such is the case with the mechanisms reported by Guidelli *et al.* [28] and our group [20], where phase transitions are controlled by the desorption of the adsorbed material and also, possibly, by its reorientation. Using a numerical method to compute electrode coverage, S, $F(t)$ can be expressed as:

$$F(t) = \frac{dS}{dt} \qquad (5)$$

Let us explore the possibility of the phase transition taking place in two consecutive steps differing in their kinetics. The current density j_1 for the first process will be given by

$$j_1(t) = q_1 \cdot F_1(t) \qquad (6)$$

where q_1 is the amount of charge exchanged and $F_1(t)$ the function describing the nucleation mechanism for the process (see the previous equations). We shall use S_1 to denote the surface fraction covered by domains of the phase in question. Once the initial domains have formed, the second nucleation process, with a different kinetics, can start; the surface area available for growth will be

S_1. We shall use S_2 to denote the surface fraction covered by the new phase. This phenomenon is mathematically equivalent to layer-by-layer 3D nucleation, [29,30] so its current density can be expressed as

$$j_2(t) = q_2 \int_0^t F_1(u) F_2(t-u) du \tag{7}$$

where q_2 is the amount of charge exchanged in the second process. As a rule, q_2 will be different from q_1 since each process may be Faradaic or capacitive — even if both are Faradaic, they may exchange a different number of electrons or exhibit a different electrode coverage per molecule. Also, functions F_1 and F_2 may be formally different (*e.g.* the former kinetic may be instantaneous nucleation and the latter progressive nucleation, or take place via a mechanism other than those described above). The possibility of the two kinetics differing is the one feature of the mechanism modelled in this work that distinguishes it from that for layer-by-layer nucleation [29], where, obviously, all layers grow via the same nucleation mechanism. The feasibility of the two kinetics differing can be easily demonstrated for the above-described example of peaks A_1 and B_2 for bipyridine.

As a rule, if more than two consecutive nucleation steps are involved, the current density for the *n*-th step can be expressed as

$$j_n(t) = q_n \int_0^t F_{n-1}(u) F_n(t-u) du \tag{8}$$

and the total current due to the serial phase transitions as

$$j_{2D}(t) = \sum_n j_n(t) \tag{9}$$

The total current for the overall chronoamperometric process will be

$$j(t) = j_{dl}(t) + j_{2D}(t) = j_{dl}(t) + \sum_n j_n(t) \tag{10}$$

where $j_{dl}(t)$ is the current due to the double layer charge, which, for simplicity, can be expressed as an exponential law:

$$j_{dl}(t) = k_1 e^{-k_2 t} \tag{11}$$

It should be noted that the inclusion of $j_{dl}(t)$ in eq. (10) is only an approximation. Strictly, it is only applicable when the contribution of the double layer does not appreciably overlap with that of the nucleation processes [31,32].

Table 1. Mathematical fitting of the experimental curves of Fig. 3 to the proposed model, based on eq. (10). For details, see text. k_d was assumed to be 9000 s^{-1} throughout.

E_1 / V	k_1 10^{-4} / $\mu A cm^{-2}$	k_2 / s^{-1}	k_i / s^{-1}	k_r / s^{-1}	$\text{ß}_1 \cdot 10^{-5}$ / s^{-2}	$k_3 \cdot 10^{-4}$ / s^{-2}	q_1 $\mu C cm^{-2}$	q_2 $\mu C\ cm^{-2}$
−0.564	3.6	2580	200	185	4.9	1.7	10.7	12.8
−0.565	3.7	2820	260	225	7.5	2.8	10.8	12.8
−0.566	3.8	3020	300	269	8.7	3.6	10.9	12.9
−0.567	3.9	3190	369	362	10.3	5.2	10.8	13.0

Application of the proposed model to the *j–t* transient for voltammetric peak C₁.

The solid line in Fig. 3 shows the simulated experimental data for selected curves obtained using the proposed model, which is described mathematically by eq. (9), for the total 2D density current:

$$j_{2D}(t) = j_1(t) + j_2(t) \tag{12}$$

$j_1(t)$ was obtained as described in a previous paper [21], in the light of the model based on the desorption–nucleation–reorientation mechanism [20], using to the following expression:

$$\frac{d\theta}{dt} = k_d(1 - S_1 - \theta) - k_i\theta - k_r\theta(1 - \theta) \tag{13}$$

where $\theta(t)$ is the time-dependent surface coverage by randomly adsorbed $BpyH_2^{2+}$–counterion pairs; $S_1(t)$ is the time-dependent surface coverage by molecules involved in the nucleation and growth (NG) process; k_d and k_i are the rate constants of adsorption and desorption, respectively, of $BpyH_2^{2+}$ —counterion pairs—; and k_r is the reorientation rate constant for $BpyH_2^{2+}$.

If overlap between neighbouring sites is assumed in accordance with the Avrami theorem [33–35], and the surface to be covered by randomly adsorbed molecules, $BpyH_2^{2+}$, as defined by Noel *et al.* [36], then

$$S_1 = (1 - \theta)(1 - \exp(-S_x)) \tag{14}$$

where S_x is the expanded area (*i.e.* excluding overlap).

The current density can be expressed as

$$\frac{j_1}{q_m} = \frac{dS_1}{dt} = (1 - \theta)\frac{dS_x}{dt}e^{-S_x} - \frac{d\theta}{dt}(1 - e^{-S_x}) \tag{15}$$

At very short times, nucleation prevails over diffusion. This allows one to obtain an approximate analytical expression for S_x as shown in ref. 21 (see also Fig. 3 therein). Thus,

$$S_x = \beta t^2 \tag{16}$$

$j_1(t)$ can be obtained by simultaneously solving eqs (13) and (15) numerically.

These conditions are the same as those used to obtain the simulated data for the first step (process A_1) below 18 ºC [21].

On the other hand, $j_2(t)$ was calculated from eq. (7), where $F_2(t)$ was obtained from eq. (3) for the instantaneous nucleation case ($n = 2$), and $j_{dl}(t)$ from eq. (11).

The solid lines in Fig. 3 show the results obtained by applying this consecutive phase formation model. As can be seen, fitting was almost perfect; at very short times, however, the model is not strictly applicable owing to the overlap between $j_{dl}(t)$ and $j_1(t)$. Table 1 lists the parameter values obtained in the simulations. As shown in previous work [21], k_d is not so significant as one can achieve good fitting provided $k_d \gg k_i$. In addition, β is also dependent on k_d, so the greater the latter is, the greater will be β.

By way of example, Fig. 4 shows the contributions of $j_{dl}(t)$, $j_1(t)$ and $j_2(t)$ to the total current density for the experimental curve obtained at $E_f = -565$ mV. Note that the shape of the curve for $j_2(t)$ (the dash–dot–dot line in Fig. 4) is inconsistent with simple instantaneous nucleation; as noted earlier, this accounts for the non-additive nature of the current densities for processes A_1 and B_1.

The total charge density exchanged in the process as calculated by integrating the previous curves was 24.5 ± 0.5 μC cm^{-2}, which is quite similar to the value obtained by integrating the corresponding voltammetric peak (C_1).
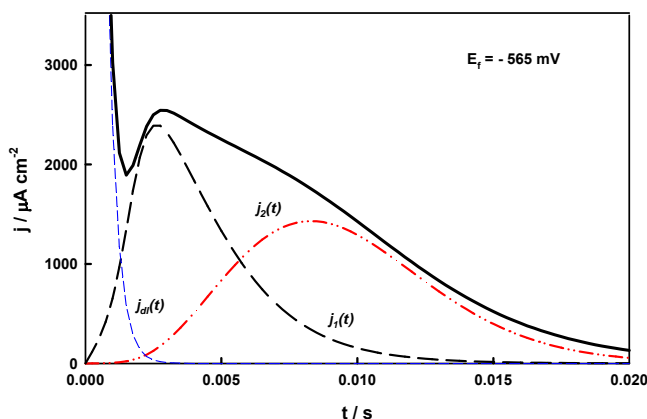

Figure 4. Individual contributions of $j_{dl}(t)$, $j_1(t)$ and $j_2(t)$ to the total current density for the experimental curve of Fig. 3*a*, obtained at E_f = –565 mV.

The proposed mathematical model was validated by conducting tests under the same conditions as in Fig. 1*a* —where peaks A_1 and B_1 are well resolved—, but using a single potential step in this case. Figure 5 shows selected curves obtained in potential-step tests performed at 15 ºC by raising the potential from an initial value E_0 = –500 mV below that of appearance of peak A_1 to an E_f value above that of appearance of B_1. As can be seen, after an initial falling portion corresponding to the double layer current, the curve exhibits two relative maxima typical of 2D nucleation processes that can thus be reasonably assigned to the corresponding voltammetric peaks (A_1 and B_1). This led us to apply eq. (12), under the same assumptions, to $j_1(t)$ and $j_2(t)$. By way of example, Fig. 6 shows the individual contributions of $j_{dl}(t)$, $j_1(t)$ and $j_2(t)$ to the

total current density for the experimental curve obtained at E_f = −564 mV as determined by using this mathematical treatment. As can be seen in Fig. 5, the simulated (solid) and experimental curves (circles) are quite consistent. Table 2 lists the parameter values obtained in the simulations.
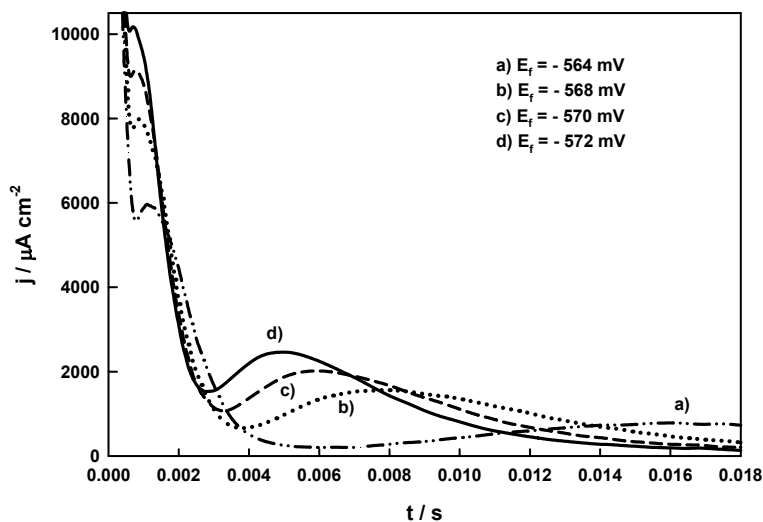

Figure 5. Experimental single-potential step j–t curves obtained at T = 25 ºC. A potential E_0 = −500 mV was applied before the jump. The final potential for each curve is shown.
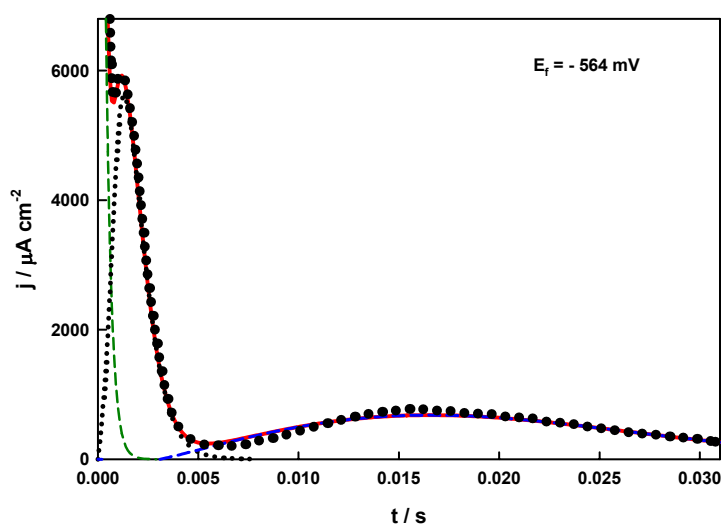

Figure 6. Individual contributions of $j_{dl}(t)$, $j_1(t)$ and $j_2(t)$ to the total current density for the experimental curve (circles) of Fig. 5a, obtained at E_f = −564 mV.

Table 2. Mathematical fitting of the experimental curves of Fig. 5 to the proposed model, based on eq. (10). For details, see text. k_d was assumed to be 9000 s^{-1} throughout

E_1 / V	k_1 10^{-4} / μAcm^{-2}	k_2 / s^{-1}	k_i /s^{-1}	k_r /s^{-1}	$\text{ß}_1 \cdot 10^{-5}$ / s^{-2}	$k_3 \cdot 10^{-3}$ / s^{-2}	q_1 μCcm^{-2}	q_2 μCcm^{-2}
−0.564	2.8	3500	450	930	29.0	2.9	11.3	14.6
−0.568	4.7	4200	700	930	33.0	14	11.7	14.7
−0.570	4.7	4200	860	990	35.5	22	11.5	15.5
−0.572	4.7	4600	990	1000	40.0	31	11.7	15.5

The values for the parameters defining $j_{dl}(t)$ and $j_1(t)$ should be taken reservedly owing to the substantial overlap between both contributions. In any case, our interest lies in $j_2(t)$.

Let us now deal with the borderline situation where the kinetics of processes A$_1$ and B$_1$ differ so markedly in their rates that the corresponding curves, $j_1(t)$ and $j_2(t)$, will be completely resolved. These conditions are reasonably closely met by the experimental curve of Fig 6. In this situation, the curves can also be simulated on the assumption that the nucleation processes A$_1$ and B$_1$ are independent. This, however, entails introducing an induction time, t_r, for $j_2(t)$ into eq. (1):

$$j_2(t) = 2k_3 q_m (t - t_r) \exp\left[- k_3 (t - t_r)^2\right] \tag{17}$$

Figure 7 shows the fitting of the experimental results of Fig. 5*a* (dotted line) to eq.(17) (dashed line), using k_3 = 3000 s^{-1} and t_r = 4·10^{-4} s.
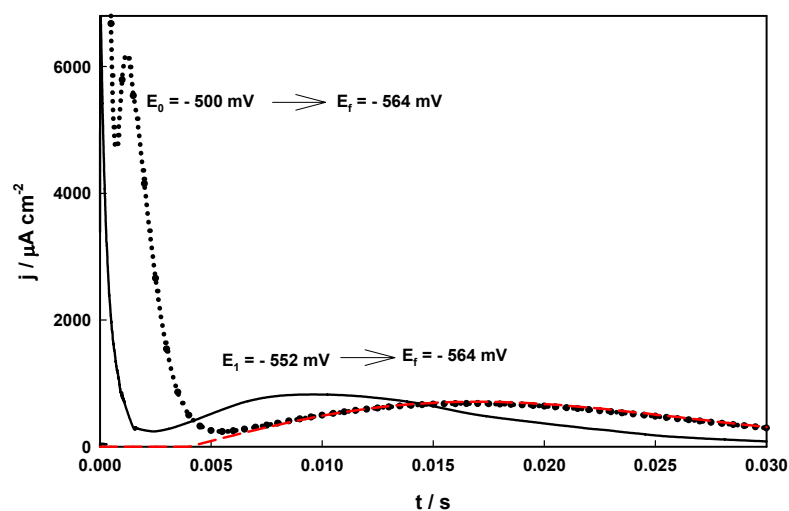
Figure 7. Experimental double-potential step j-t curve shown in Fig. 2 (solid line). For clarity, only the second jump is shown and the onset has been shifted to t = 0. The dotted line corresponds to the experimental single-potential step j-t curve of Fig. 6. The dashed line represents the simulated results provided by the model based on eq. (17).

If the phase transitions corresponding to processes A_1 and B_1 were completely independent, then $j_2(t)$ should be the same whether the experiment is conducted in a single step (Fig. 6) or in two (Fig. 2). However, as can be seen in Fig 7, which shows the results of both experiments at E_f = -564 mV (for clarity, only the second step of Fig. 2 is shown and its onset has been shifted to t = 0), $j_2(t)$ appeared at longer times with a single potential step. This was so in spite of the fact that the growth rate constant for the second process, k_3, was similar in both cases. The slower kinetics of $j_2(t)$ in the double-potential step experiment was a result of the second phase starting to form immediately after the second pulse was applied as the electrode was by then completely covered by the first phase (A_1). In the single-potential step experiment, however, the

second phase only started to form in the region where the first phase had previously formed; this delayed its appearance by an amount of time known as the *induction time*.

This provides an alternative interpretation for the induction time. Traditionally [37], this quantity has been associated to the delay required for critical nuclei in a 2D phase to grow. Based on the proposed consecutive 2D phase formation model, however, the induction time is the time required for the first phase to form. The current density of such a phase can occasionally be concealed by the double layer charge —as is indeed the case in the examples of Figs 5 and 6— or be low —of the capacitive type. This phenomenon will be examined in greater detail in future work.

Based on the above-described results and, as noted in previous papers [12,21], a mixed phase may be formed after peak A$_1$ (*viz.* in potential region II in ref. 12) below 18 ºC. Such a phase is formed by BpyH$_2^{2+}$ molecules initially adsorbed on the electrode surface, via either a prior desorption–nucleation process or direct incorporation into the condensed phase following slow reorientation. A BpyH$_2^{\cdot+}$–BpyH$_2^{2+}$ mixed valency complex must be formed in such a phase that will be in direct contact with the electrode, I$^-$ acting as the counterion. Taking into account that the theoretical value for a configuration with the 4,4´-Bpy rings parallel to the electrode surface is *ca.* 72 Å^2 [11], we believe that both species, BpyH$_2^{\cdot+}$ and BpyH$_2^{2+}$, must have face-on geometries in the complex. Accordingly, the mixed 2D phase must cover a surface area of *ca.* 140 Å^2 per BpyH$_2^{\cdot+}$ molecule, which is equivalent to a charge density of 11 µC

cm^{-2} and thus similar to that obtained for voltammetric peak A_1. Such a structure may subsequently break at potentials corresponding to the appearance of peak B_1, $BpyH_2^{2+}$ molecules being reduced and the electrode covered by a new 2D phase consisting solely of the salt of Bpy cation radical and iodide and forming through instantaneous nucleation. Based on the experimental value of *ca.* 60 $Å^2$ obtained for the overall 2D phase formation, A+B or C processes, we propose a tilted orientation for the $BpyH_2^{.+}$ molecules (with an angle between the principal molecular axis and the electrode plane), even though we cannot be more specific about it.

Conclusions

Below 18 ºC, the first reduction process of bipy (*viz.* the $BpyH_2^{2+}$/$BpyH_2^{.+}$ redox couple) on mercury in an acid medium containing iodide as counterion gives three pairs of narrow cyclic voltammetric peaks (*viz.* A_1/A_2, B_1/B_2 and D_1/D_2) due to the formation/destruction of condensed phases. The chronoamperometric behaviour observed at more positive potentials is accurately described by a mathematical model based on an adsorption–nucleation mechanism involving a molecular reorientation term. A new, more compact 2D phase is formed at more negative potentials via instantaneous nucleation and growth. The overall process is strongly temperature-dependent. Thus, although the second phase is always formed in the region where the first has previously formed, the rate of formation of both is comparable —a single voltammetric peak is observed— above 18 ºC; therefore, the mathematical

treatment of the corresponding experimental *j–t* curves must include provisions for growth of the second phase as a function of the first (*i.e.* for consecutive 2D phases). Below 18 ºC, however, the second phase is formed much more slowly than the first —two voltammetric peaks are observed—, so the two processes can be analysed in a virtually independent manner.

Acknowledgements

References

[1] Budevski, E.; Staikov, G.; Lorenz, W.J.   In: Electrochemical Phase Formation and Growth, VCH, Weinheim, 1996.

[2] Rodríguez-Amaro, R.; Ruiz, J.J. In: *Handbook of Surfaces and Interfaces of Materials*, H.S. Nalwa (Ed.), vol 1, p. 660, Academic Press, 2001.

[3] Wandlowski, Th. In: Encyclopedia of Electrochemistry, VCH–Wiley, Weinheim, 2002.

[4] Lee C.; Bard, A.J. *J. Electroanal. Chem*., **1988**, 239, 441.

[5] Díaz, A.; Kaifer, E. *J. Electroanal. Chem*., **1988**, 249, 333.

[6] Sánchez-Maestre, M.; Rodríguez-Amaro, R.; Muñoz, E.; Ruiz, J.J.; Camacho, L. *J. Electroanal. Chem*., **1993**, 359, 325.

[7] Salas, R.; Sánchez-Maestre, M.; Rodríguez-Amaro, R.; Muñoz, E.; Ruiz, J.J.; Camacho, L. *Langmuir*, **1995**, 11, 1791.

[8] Millán, J.I.; Sánchez-Maestre, M.; Camacho, L.; Ruiz, J.J.; Rodríguez-Amaro, R. *Langmuir*, **1997**, 13, 3860.

[9] Millán, J.I.; Rodríguez-Amaro, R.; Ruiz, J.J.; Camacho, L. *Langmuir*, **1999**, 15, 618.

[10] Millán, J.I.; Rodríguez-Amaro, R.; Ruiz, J.J.; Camacho, L. *J.Phys. Chem. B*, **1999**, 103, 3669.

[11] Millán, J.I.; Ruiz, J.J.; Camacho, L.; Rodríguez-Amaro, R. *J. Electroanal. Chem*., **2001**, 497, 168.

[12] Sánchez-Maestre, M.; Rodríguez-Amaro, R.; Muñoz, E.; Ruiz, J.J.; Camacho, L. *Langmuir* **1994**, 10, 723.

[13] Arihara, K.; Kitamura, F.; Nukanobu, K.; Ohsaka, T.; Tokuda, K. *J. Electroanal. Chem*., **1999**, 473, 138.

[14] Arihara, K.; Kitamura, F.; Ohsaka, T.; Tokuda, K. *J. Electroanal. Chem*., **2000**, 488, 117.

[15] Wandlowski, Th.; Ataka, K.; Mayer, D. *Langmuir*, **2002**, 18, 4331.

[16] Mayer, D.; Dretschkow, Th.; Ataka, K; Wandlowski, Th. *J. Electroanal. Chem*., **2002**, 524, 20.

[17] Sagara, T.; Tanaka, S.; Fukuoka, Y.; Nakashima, N. *Langmuir*, **2001**, 17, 1620.

[18]   Sagara, T.; Tanaka, S.; Miuchi, K.; Nakashima, N. *J. Electroanal. Chem*., **2002**, 524, 68.

[19] Sagara, T.; Miuchi, K. *J. Electroanal. Chem*., **2004**, 567, 193.

[20] Millán, J.I.; Ruiz, J.J.; Camacho, L.; Rodríguez-Amaro, R. *Langmuir* **2003**, 19, 2338.

[21] Gómez, L.; Ruiz, J.J.; Camacho, L.; Rodríguez-Amaro, R. *J. Electroanal. Chem*., **2004**, 564, 179.

[22] Bewick, A.; Fleischmann, M.; Thirsk, H.R. *Trans. Faraday Soc*., **1962**, 58, 2200.

[23] Fleischmann, M.; Thirsk, H.R. In Advances in Electrochemistry and Electrochemical Engineering, P. Delahay (Ed.), vol. 3, Wiley, 1963.

[24] Palomar-Pardavé, M.; González, I.; Soto, A.B.; Arce, E.M. *J. Electroanal. Chem*., **1998**, 443, 125.

[25] Randriamahazaka, H.; Noël, V.; Chevrot, C. *J. Electroanal. Chem*., **1999**, 472, 103.

[26] Philipp, R.; Dittrich, J.; Retter, U.: Müller, E. *J. Electroanal. Chem.,* **1988**, 250, 159.

[27] Wandlowski, Th.; Dretschkow, Th. *J. Electroanal. Chem.*, **1997**, 427 105.

[28] Guidelli, R.; Foresti, M.L.; Innocenti, M. *J. Phys. Chem*. **1996**, 100, 18491.

[29] Armstrong, R.D.; Harrison, J. A. *J. Electrochem. Soc*., **1969**, 116, 328.

[30] Rangarajan, S.K. *J. Electroanal. Chem.*, **1973**, 46, 124.

[31] Donner, C. ; Pohlmann, L. *Langmuir*, **1999**, 15, 4898.

[32] Donner, C. ; Pohlmann, L. *Langmuir*, **1999**, 15, 4907.

[33] Avrami, M. *J. Chem. Phys*., **1939**, 7, 1103.

[34] Avrami, M., *J. Chem. Phys*., **1940**, 8, 212.

[35] Avrami, M., *J. Chem. Phys*., **1941**, 9, 177.

[36] Noel, M.; Chandrasekaran, S.; Ahmed Basha, C. *J. Electroanal. Chem*., **1987**, 225, 93.

[37] Wandlowski, Th.; *J. Electroanal. Chem.* **1990**, 293, 219.

4.3. 2D PHASE TRANSITIONS IN THE ELECTROCHEMICAL STUDY OF ETHYL VIOLOGEN ON MERCURY IN IODIDE MEDIA

Abstract

This paper reports structural and kinetic information about a two-dimensional phase transition that takes place in the electrochemical study of ethyl viologen on mercury in the presence of iodide ions prior to reduction by diffusion of ethyl viologen dication. Unlike other viologens, it is the dication rather than the cation radical that seemingly forms the condensed phase in this case.

Introduction

Viologens, which are 1,1'-disubstituted 4,4'-bipyridils (V^{2+}), are of great electrochemical interest on account of their role in redox reactions involving stable free radicals that can be used as electrochemical mediators in homogeneous [1–9] and heterogeneous reactions [10–17].

A number of papers on the two-dimensional phases of the cation radical formed in the electrochemical reduction of viologen on various electrode surfaces such as Hg [18–25], Hg–Au [26], Pt [27], Au(111) [28–31], and highly oriented pyrolytic graphite [32,33] have been reported in recent years. Some of these studies including the influence of temperature, the reagent concentration and the type of anion present in the medium have focussed on cyclic voltammetry and capacitance measurements. On the other hand, kinetic and mechanistic studies have relied on chronoamperometric measurements.

These studies have exposed the influence of the length of the alkyl chain of viologen (*n*) on the properties of the phase transitions and their behaviour; such an influence should therefore be examined in greater depth. In this respect, the behaviour of viologens with *n* = 0 (Bpy), *n* = 1 (MV) and *n* = 7 (HV) has already been studied to some extent. There remains the need to examine the case of the viologen with *n* = 2 as the greatest differences are to be expected in short-chain rather than in long-chain viologens. However, ethyl viologen (EtV^{2+}) has only been the subject of general comparative studies

[32,34,35] not dealing in depth with mechanistic or kinetic aspects. In this work, a comprehensive study of the 2D phase formed by the EtV^{2+} dication and I^- anion on a mercury electrode in iodide media was performed and kinetic information derived in the light of recently developed models. Iodide anion was selected on account of the fact that it is one of the ions most readily giving phase transitions. Other interesting anions such as bromide, however, might also be examined in future work.

Experimental

1,1*N*-Diethyl-4,4*N*-bipyridinium dibromide (99 %) and KI (> 99.5 %) were supplied by Aldrich Chemical Co. and used as received. All solutions were prepared in Milli-Q water.

Electrochemical recordings were obtained by using an Autolab PGSTAT30 potentiostat/galvanostat equipped with SCAN-GEN and FRA2 modules in addition to an FI20 integration module controlled via general purpose electrochemical system (GPES) and frequency response analysis software. The working electrode was a Metrohm 663 V Stand HMDE with a surface area of 0.384 ± 0.005 mm^2, the auxiliary electrode Pt and the reference electrode Ag|AgCl (3.0 M KCl). All potentials given here are referred to this electrode. Electrochemical measurements were made in a nitrogen atmosphere and the temperature was measured to within ± 0.1 ºC in all instances.

Results and Discussion

Figure 1a shows the voltammograms for 1.3 mM EtV^{2+} in 0.1 M KI, obtained over an Hg electrode at a scan rate v = 100 mV/s at T = 3 ^{o}C. As can be seen, in the cathodic scan, EtV^{2+} exhibits a well-defined peak C which posseses the typical features of diffusion-controlled processes. In addition, the presence of peak K in the anodic scan, which is consistent with stripping of a precipitate, confirms that peak C is the result of two consecutive processes, namely: one-electron reduction of EtV^{2+} molecules reaching the electrode by diffusion and precipitation of the cation radical formed in this process with iodide anion as the counterion. This behaviour is similar to that previously observed in other viologens, so it is not dealt with in greater detail in this work.

In addition to peak C, the cathodic scan included four narrow, sharp peaks (A_1, B_1, D_1 and E_1) and the anodic scan the corresponding oxidation peaks (A_2, B_2, D_2 and E_2). These peaks are typical of electrode processes involving molecules immobilized at an electrode; only peaks A and B (see the reverse-scan voltammogram at –0.615 V in Fig. 1a), which were observed at temperatures below 9 ºC (see Fig. 1b at T = 15 ºC), were studied in this work.
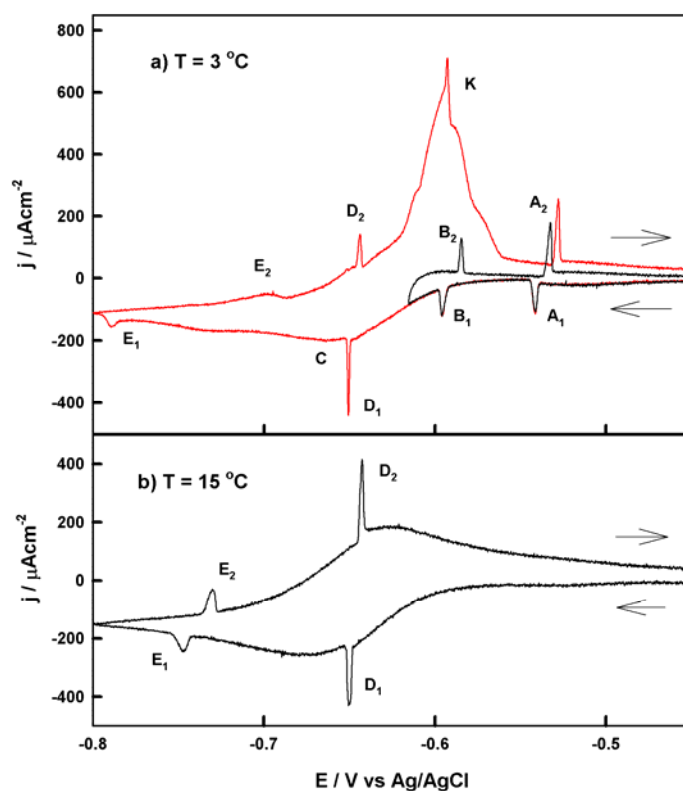
Figure 1. Voltammograms for a 1.3 mM solution of EtV^{2+} in 0.1 M KI at v = 100 mV/s obtained at (*a*) T = 3 ºC and (*b*) T = 15 ºC.

Figure 2 shows the variation of the peak potentials (E_p) with the logarithm of the I$^-$ ion concentration for peaks A$_1$ and B$_1$. The experimental conditions used where [EtV^{2+}] = 1 mM, v = 100 mV/s and T = 3 °C.
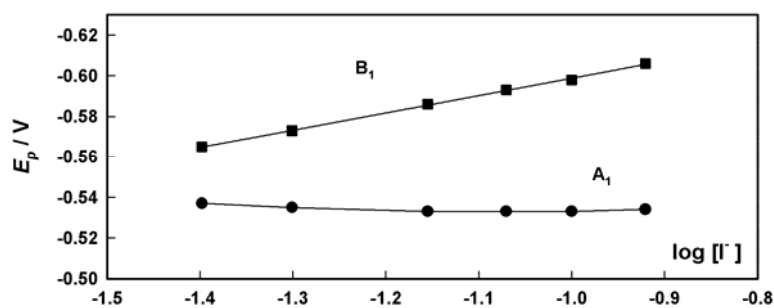
Figure 2. Plots of E_p vs log [I$^-$] for voltammetric peaks A$_1$ and B$_1$ obtained in 1 mM EtV^{2+} at T = 3 °C and v = 100 mV/s.

Peak B_1 shifted to more negative potentials and peak A_1 to slightly more positive potentials with increase in the salt concentration. Increasing the EtV^{2+} concentration while keeping all other variables constants (data not shown) had similar effects to raising the I^- concentration.

Assignation of voltammetric peaks. We analysed the nature of peaks A and B by examining the changes in peak currents (I_p) and peak widths at half-height (W) with the scan rate (v), for at least 10 voltammetric runs over the scan rate range 25–250 mV/s in each experiment. The plots of log I_p and log W against log v (not shown) were roughly linear for all peaks; their slopes are given in Table I. We also analysed the hysteresis or separation between peak potentials, $\Delta E_p = E_p(X_2) - E_p(X_1)$, where X denotes either peak (A or B). The plots of log ΔE_p *versus* log v were all linear; their slopes are listed in Table I.

Table I. Selected Q values and voltammetric data for the nucleation peaks as obtained at $T = 3$ °C. [EV^{2+}] ranged from 1 to 3 mM and [KI] from 0.06 to 0.12 M.

Peak	Q $(\mu C cm^{-2})$	$\partial E_p/\partial \log v$	$\partial \log I_p/\partial \log v$	$\partial \log W/\partial \log v$	$\partial \log \Delta E_p/\partial \log v$
A_1	3.5 ± 1	4.6 ± 0.2	0.55 ± 0.01	0.32 ± 0.02	0.36 ± 0.02
A_2	5.0 ± 1	–2.1 ± 0.2	0.64 ± 0.01	0.4 ± 0.02	0.36 ± 0.02
B_1	2.5 ± 0.2	1.6 ± 0.3	0.71 ± 0.01	0.35 ± 0.03	0.39 ± 0.01
B_2	2.3 ± 0.1	–4.6 ± 0.2	0.56 ± 0.01	0.46 ± 0.01	0.39 ± 0.01

The data in Table I are consistent with the theoretical values for 2D phase transitions on electrodes [36,37]. Thus, the log–log plots of I_p, W and ΔE_p as a function of v must all be linear and have slopes of x, $1 - x$ and $1 - x$, respectively, where $x \geq 0.6$. Accordingly, one can assign peaks A and B to 2D

phase transitions.

Peaks A_1 and A_2 correspond to the formation and destruction, respectively, of a 2D phase that will henceforth be referred to as "phase γ". The charge obtained by integrating the two peaks increased slightly with increasing concentration of EtV^{2+} (*e.g.* from 2 µC cm^{-2} at 1 mM to 4.5 µC cm^{-2} at 3.5 mM in 0.1 M KI media). Such small charge values relative to the reduction of other viologens to the corresponding cation radicals, *ca.* 10–24 µC cm^{-2}, must be associated to a purely capacitive phenomenon. Should they be due to a faradaic process, they would correspond to an area of *ca.* 650–360 Å^2, which is quite inconsistent with the maximum area one can expect for a face-on configuration of $EtV^{\cdot+}$ (*ca.* 130–150 Å^2) [32]. On the other hand, peaks B_1 and B_2 correspond to the destruction and formation of phase γ, respectively. The small charge obtained by integrating peaks B_1 and B_2, which remained virtually constant at about 2.5 µC cm^{-2} throughout the studied concentration range, must correspond to a purely capacitive phenomenon.

Structure and kinetics of phase γ. In order to derive further information about the region of occurrence of the phase, we ran capacitance–potential (*C*–*E*) curves under different conditions. Figure 3 shows the *C*–*E* curve obtained over the potential range from –0.51 to –0.70 V for a 1 mM EtV^{+2} solution containing 0.08 M KI at *T* = 3 °C (*a*), and the voltammogram obtained from the same EtV^{+2} solution at *v* = 100 mV s^{-1} (*b*). At potentials in between those of appearance of peaks A_1 (*E* ≈ –0.54 V) and B_1 (*E* ≈ –0.575 V), zone II in Fig 3*b*, the capacitance decreased sharply —even below that of the supporting

electrolyte. These capacitance "pits" are also characteristic of 2D phase transitions processes [38]. Figure 4 shows *C–E* curves obtained at variable concentrations of EtV^{+2} in 0.08 M KI at *T* = 3 °C. The capacitance in the pit was virtually independent of the concentration of EtV^{2+}. This was also the case at a variable concentration of I$^-$ (results not shown). Figures 3 and 4 were obtained at 77 Hz and were essentially similar to those found at other frequencies over the range 77–477 Hz.

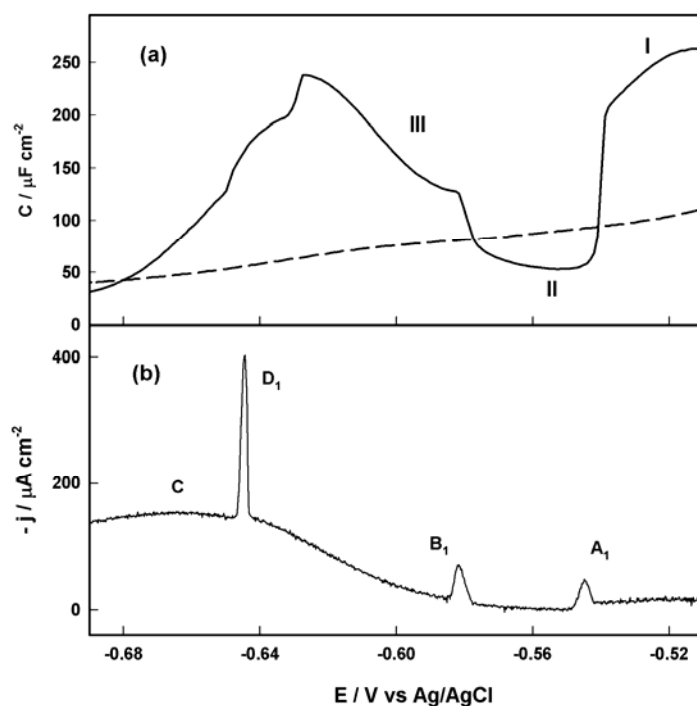Figure 3. Plots of *C* (*a*) and current density (*b*) as a function of *E*. *C* was measured by using a potential pulse of 10 mV, a potential step of 1 mV and a frequency of 77 Hz. The dashed line corresponds to a solution of 0.08 M KI containing no EtV^{2+} and the solid line to the same solution containing 1 mM EtV^{2+}. The voltammogram was obtained from the same EtV^{2+} solution at *v* = 100 mV/s. *T* = 3 °C
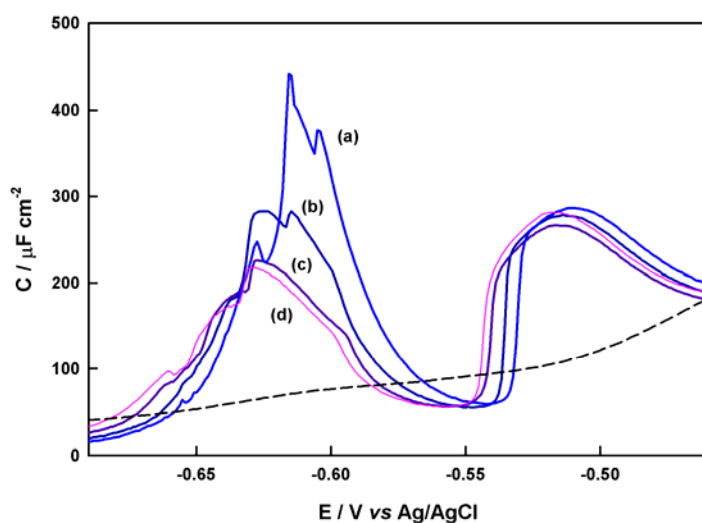
Figure 4. Plots of *C vs E* (solid lines) at variable concentrations of EtV^{2+}: (*a*) 2 mM, (*b*) 1.4 mM, (*c*) 1 mM, (*d*) 0.8 mM. The dashed line corresponds to a solution of 0.08 M KI containing no EtV^{2+}. All others conditions as in Fig. 3*a*.

The stability and composition of the 2D condensed phase γ formed by ethyl viologen dication on mercury electrode has been analysed in terms of the following equation [21]:

$$[\Delta E_\gamma]^2 = \text{ART} \ \ln\left[[EtV^{2+}]^n [X^-]^m\right] + \text{BT} + \text{C} \qquad (1)$$

where [EtV^{2+}]^n [X$^-$]^m is the product of the ethyl viologen dication molecule and counter-anion concentrations on the assumption of (EtV^{2+})$_n$(X$^-$)$_m$ structure; A, B and C are constants, and ΔE_γ, after Sridharan *et al.* [39], is defined as the difference between *E$^+$* and *E$^-$*, which are the positive and negative potential, respectively, by which the region where the condensed phase γ exists is bounded. Equation (1) is a slightly modified form of the original expression for neutral organic molecules [39-41].

Parameter ΔE_γ was determined from the distance between the peak potentials for A_1 and B_1, which entailed relating the peak potential for A_1 with E^+ and that for B_1 with E^-. The ΔE_γ values thus obtained were virtually identical with those found by measuring the distance between the standard potentials for the two peaks, $E^0_A - E^0_B$. This was the result of the shifts in the E_p–v curves being similar for peaks A1 and B1 on the one hand, and peaks A2 and B2 on the other (see Table I), which cancelled the influence of v in subtracting. This method for measuring ΔE_γ was used in previous work [21,42]. Also, we applied Eq. 1 to results from experiments where the peak potential for B_1 was distant enough from the standard reduction potential for the $EtV^{2+}/EtV^{\cdot+}$ couple (peak C) for the concentration of the dication around the electrode between peaks A_1 and B_1 to be assumed constant and equal to that of EtV^{2+} in the bulk solution.

At a constant temperature, plots of $(\Delta E_\gamma)^2$ *vs* ln $[EtV^{2+}]$ at constant $[I^-]$ and plots of $(\Delta E_\gamma)^2$ *vs* ln $[I^-]$ at constant $[EtV^{2+}]$ were found to be linear and have roughly the same slope, which suggests that $n = m$, *i.e.* the ratio of $[EtV^{2+}]$ to $[I^-]$ in the condensed phase γ must be about 1:1. Subsequently, the body of data conforming to these relations was used to determine constants A, B and C in Eq. 1 by numerical fitting of the experimental $(\Delta E_\gamma)^2$ values in the equation. The values thus obtained were A = $(1.3 \pm 0.3) \times 10^{-6}$ $V^2/J\cdot mol$, B = $(-5.5 \pm 0.5) \times 10^{-4}$ V^2/K and C = 0.181 ± 0.03 V^2. Figure 5 shows a plot of $(\Delta E_\gamma)^2$ *vs* {ART ln $([EtV^{2+}][I^-]) + BT + C$} obtained by using the previous A, B and C values. It was acceptably linear with a slope of unity, so Eq. 1 was reasonably well satisfied with $n = m = 1$.
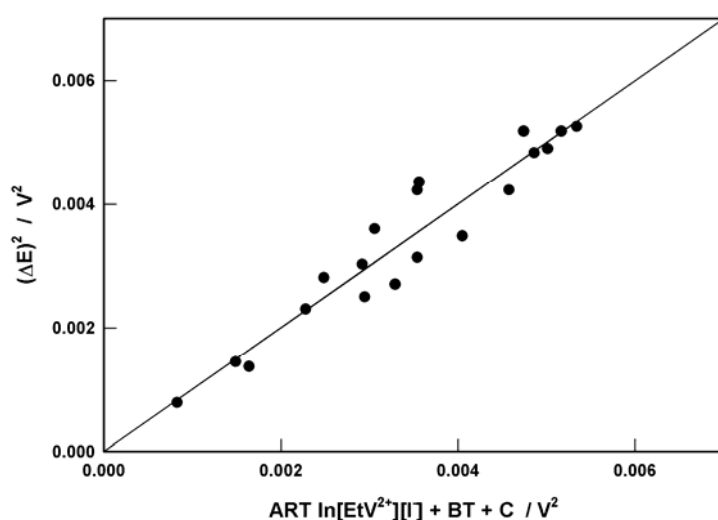
Figure 5. Plot of $(\Delta E_\gamma)^2$ *vs* {ART ln ([EtV^{2+}][I$^-$]) + BT + C}. $(\Delta E_\gamma)^2$ values were obtained by measuring the distance between the peak potentials for peaks A$_1$ and B$_1$. The solid line represents the predictions of Eq. 1 with A = (1.3 ± 0.3) × 10^{-6} V^2/J·mol, B = (−5.5 ± 0.5) × 10^{-4} V^2/K and C = 0.181 ± 0.03 V^2.

According to Wandlovski *et al.* [43], when ΔE_γ = 0 in Eq. 1 one can define the critical product K^*_C = [EtV^{2+}][I$^-$] = *exp*[(−B/AR) − (C/ART)] that must be reached for the phase to be formed; this can be taken as an interfacial analogue of the solubility product. We obtained K^*_C = 5.6 x 10^{-5} M^2.

Kinetic information for the processes corresponding to voltammetric peaks A and B can be obtained by using chronoamperometric technique [44, 45]. We ran potentiostatic curves for peaks A$_1$ and B$_1$. Figure 6 (symbols) shows selected experimental *j–t* curves for peak A$_1$ as obtained for a 2.5 mM solution of EtV^{2+} containing 0.1 M KI at *T* = 3 °C. These curves were experimentally obtained by applying a potential E_1 = −0.51 V preceding that of appearance of peak A$_1$ by 0.01 s, followed by a potential pulse up to a potential E_2 immediately following that of appearance of this peak. The curves exhibit typical maxima that

allow the nucleation processes involved to be characterized. The experimental data fit a simple mathematical nucleation–growth–collision (NGC) model such as the Bewick-Fleischmann-Thirsk (BFT) [44-46] for the instantaneous case, expressed as:

$$j_{2D}(t) = 2\beta q_m (t - t_r) \, \exp\left[- \beta(t - t_r)^2\right] \tag{2}$$

with q_m being the total charge involved in the phase transition, β a coefficient combining the rates of nucleation and growth and t_r the induction time, *i.e.*, the time delay needed for nuclei to form. The total current for the overall chronoamperometric process is

$$j(t) = j_{dl}(t) + j_{2D}(t) \tag{3}$$

where $j_{dl}(t)$ is the current due to the double layer charge, which, for simplicity, can be expressed as an exponential law:

$$j_{dl}(t) = k_1 e^{-k_2 t} \tag{4}$$

It should be noted that the inclusion of $j_{dl}(t)$ in Eq. 4 is only an approximation. Strictly, it is only applicable when the contribution of the double layer does not appreciably overlap with that of the nucleation processes [47, 48].

The solid line in Fig. 6 represents the simulated results provided by the model based on Eq. 3. By way of example, Fig. 7 shows the individual contributions of $j_{dl}(t)$ and $j_{2D}(t)$ to the total current density for the experimental curve of Fig. 6, obtained at $E_2 = -0.534$ V. Consistency between the

experimental and simulated data was quite good. Table II compiles the parameter values obtained in the simulations.
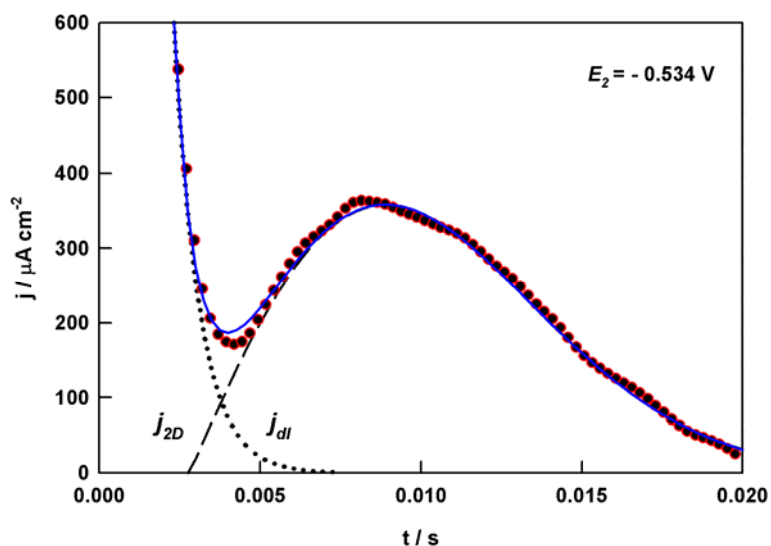
Figure 7. Individual contributions of $j_{dl}(t)$ and $j_{2D}(t)$ to the total current density for the experimental curve of Fig. 6, obtained at $E_2 = -0.534$ V.

Table II. Mathematical fitting of the experimental curves of Fig. 6 to the model based on Eq. 3.

E_f (mV)	q_m ($\mu C\ cm^{-2}$)	k_1 ($\mu A\ cm^{-2}$)	k_2 (s^{-1})	β (s^{-1})	t_r (s)
−534	3.6	10500	1250	13440	0.0028
−536	3.3	9000	1125	30480	0.0025
−538	3.3	13000	1360	43250	0.0017
−540	3.1	20000	1590	66120	0.0015

For peaks B_1, we use the double-pulse technique. Figure 8 (symbols) shows selected experimental j–t curves for peak B_1 obtained under the same experimental conditions as in Fig. 6, but $E_2 = -0.54$ V for a time $\tau = 0.03$ s and variable E_3 values. For clarity, only the second jump is shown and the onset has

been shifted to $t = 0$.

By way of example, Fig. 9 (circles) shows the j–t curve obtained from Fig. 8 at $E_3 = -0.607$ V following elimination of the contribution of the double layer, j_{dl} (t), by using Eq. 4. The results are consistent with the presence of two overlapped processes. These curves were analysed by using the mathematical model for consecutive 2D phase transitions [24].

Based on this model, the current density j_1 (t) for the first process will be given by

$$j_1(t) = q_1 \cdot F_1(t) \tag{5}$$

where q_1 is the amount of charge exchanged and $F_1(t)$ the function describing the nucleation mechanism for this process. We shall use S_1 to denote the surface fraction covered by domains of the phase in question. Once the initial domains have formed, the second nucleation process, with a different kinetics, described by F_2 (t), can start; the surface area available for growth will be S_1. We shall use S_2 to denote the surface fraction covered by the new phase. This phenomenon is mathematically equivalent to layer-by-layer 3D nucleation [49, 50], so its current density can be expressed as

$$j_2(t) = q_2 \int_0^t F_1(u) F_2(t-u) du \tag{6}$$

where q_2 is the amount of charge exchanged in the second process.

The possibility of the kinetics differing is the one feature of the consecutive 2D mechanism model that distinguishes it from that for layer-by-layer nucleation

[49], where, obviously, all layers grow via the same nucleation mechanism. In our system, the feasibility of the two kinetics differing can be easily inferred from the complexity of the experimental curves (Fig. 8 and 9), which cannot be fitted to a layer-by-layer nucleation model.

The total current for the overall chronoamperometric process will be

$$j(t) = j_{dl}(t) + j_1(t) + j_2(t) = j_{dl}(t) + j_{2D}(t) \tag{7}$$

$j_1(t)$ was calculated from the BFT model for the instantaneous nucleation case, Eq. 2, with $t_r = 0$. On the other hand, $j_2(t)$ was obtained in the light of the model based on the desorption–nucleation–reorientation mechanism [25], using to the following expression:

$$\frac{d\theta}{dt} = k_d(1 - S_2 - \theta) - k_i\theta - k_r\theta(1 - \theta) \tag{8}$$

where $\theta(t)$ is the time-dependent surface coverage by randomly adsorbed EtV^{2+}–counterion pairs; k_d and k_i are the rate constants of adsorption and desorption, respectively, of EtV^{2+} —counterion pairs—; and k_r is the reorientation rate constant for EtV^{2+}.

If overlap between neighbouring sites is assumed in accordance with the Avrami theorem [51-53], and so is that the surface will be covered by randomly adsorbed molecules as defined by Noel *et al.* [54], then

$$S_2 = (1 - \theta)(1 - \exp(-S_x)) \tag{9}$$

where S_x is the expanded area (*i.e.* that excluding overlap).
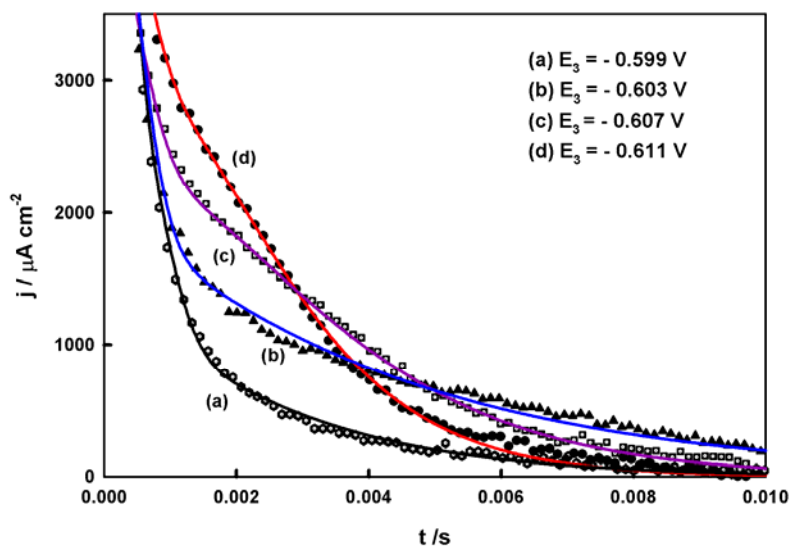
Figure 8. Experimental double-potential step j-t curves (circles) obtained under the same experimental conditions as in Fig. 6, but $E_2 = -0.54$ V for a time $\tau = 0.03$ s and variable E_3 values. For clarity, only the second jump is shown and the onset has been shifted to $t = 0$. Solid lines represent the simulated results provided by the model based on Eq. 7.
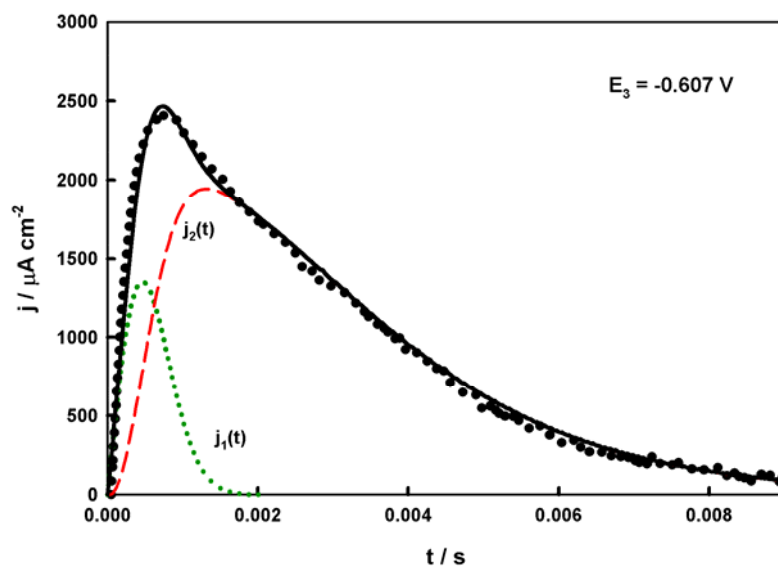
Figure 9. Circles represent the experimental curve of Fig. 8, obtained at $E_3 = -0.607$ V following elimination of the contribution of $j_{dl}(t)$. The solid line represents the simulated results provided by the model based on Eq. 2 for the first step, $j_1(t)$ (dotted line) and Eq. 8 and Eq. 10 for the second step, $j_2(t)$ (dashed line).

The current density per charge can be expressed as

$$\frac{j_2}{q_m} = \frac{dS_2}{dt} = (1-\theta)\frac{dS_x}{dt}e^{-S_x} - \frac{d\theta}{dt}(1-e^{-S_x}) \tag{10}$$

If we assume the instantaneous nucleation mechanism to prevail, then the following approximate analytical expression for S_x as shown in ref. 25 can be obtained:

$$S_x = \beta t^2 \tag{11}$$

$j_2(t)$ can be determined by simultaneously solving Eq. 8 and Eq. 10 numerically.

The solid lines in Fig. 8 show the results obtained by applying this consecutive phase formation model. The fit was almost perfect; at very short times, however, the model is not strictly applicable owing to the overlap between $j_{dl}(t)$ and $j_1(t)$, so the results for both terms should only be accepted tentatively. Table III lists the parameter values obtained in the simulations. As shown in previous work [25], k_d is not so significant as one can achieve good fitting provided $k_d \gg k_i$. In addition, β is also dependent on k_d, so the greater the latter is, the greater will be β.

By way of example, Fig. 9 shows the contributions of $j_1(t)$ and $j_2(t)$ to the total 2D current density, $j_{2D}(t)$, for the experimental curve obtained at $E_3 = -0.607$ V.

Table III. Mathematical fitting of the experimental curves of Fig. 8 to the model based on Eq. 7. k_d was fixed at $9000 \ s^{-1}$.

	$J_1(t)$		$J_2(t)$			
$E_f \ (mV)$	$q_m \ (\mu C \ cm^{-2})$	$k_1 \cdot 10^{-5} \ (\mu A \ cm^{-2})$	$q_m \ (\mu C \ cm^{-2})$	$k_i \ (s^{-1})$	$k_r \ (s^{-1})$	$\beta \cdot 10^{-7} \ (s^{-1})$
−603	1.1	33	7.8	235	20	6
−605	1.1	33	8.1	270	100	12
−607	0.8	30	8.1	290	200	30
−609	1.0	33	8.3	335	270	32
-611	0.8	33	7.8	380	370	38

Figure 10 shows the variation of constant k_r with the final potential of the potentiostatic pulse. Extrapolation to $k_r = 0$ allows one obtain [25] the standard potential for the second 2D phase transition process, E^0. As can be seen, $E^0 \approx -602.5$ mV.
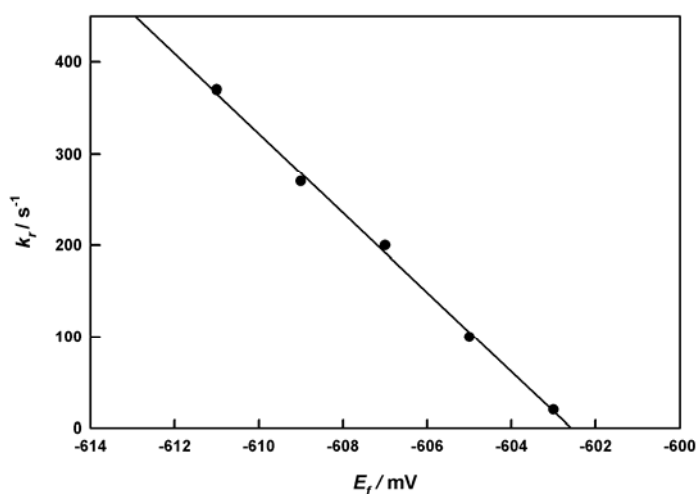

Figure 10. Plot of k_r against the final potential of the potentiostatic jump obtained from the simulated curves in Fig. 8.

We also analysed the j–t curves corresponding to the anodic peaks A_2 and B_2. For peak B_2, we used the multi-pulse technique. Figure 11 shows selected experimental j–t curves obtained under the same experimental conditions as in

Fig. 6, but E_3 = –0.605 V for a time τ = 0.05 s and variable E_4 values. For clarity, only the third jump (corresponding to peak B$_2$) is shown in Fig. 12 and the onset has been shifted to t = 0. As with peak A$_1$, the experimental data fit the simple BFT mathematical model [44-46] for the instantaneous case, defined by Eqs 2 and 3. Table IV compiles the parameter values obtained in the simulations.

Figure 11. Experimental multi-potential step j–t curves obtained under the same experimental conditions as in Fig. 8, but E_3 = –0.605 V for time τ = 0.05 s and variable E_4 values.

Table IV. Mathematical fitting of the experimental curves of Fig. 11 to the model based on Eq. 3. t_r = 0

E_f (mV)	q_m (μC cm^{-2})	k_1 (μA cm^{-2})	k_2 (s^{-1})	$\beta \cdot 10^{-3}$ (s^{-1})
–580	4.9	9600	1700	125
–582	5.0	8850	1580	95
–584	5.0	7680	1500	74
–586	5.0	7550	1500	56
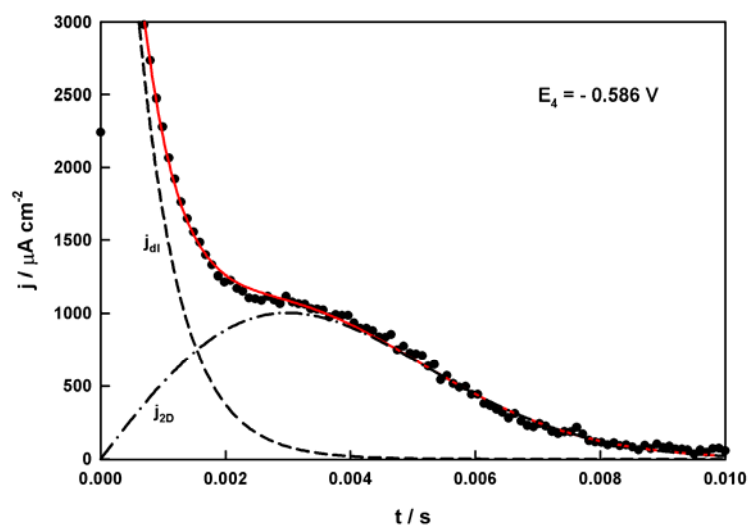
Figure 12. Individual contributions of $j_{dl}(t)$ and $j_{2D}(t)$ to the total current density for the experimental curve of Fig. 11, obtained at $E_4 = -0.586$ V. For clarity, only the third jump is shown and the onset has been shifted to $t = 0$. Circles represent experimental data.

For peaks A_2, we used the double-pulse technique. Figure 13 shows selected experimental j–t curves obtained under the same experimental conditions as in Fig. 6 but $E_2 = -0.54$ V for a time $\tau = 0.03$ s and variable E_3 values. For clarity, only the second jump (corresponding to peak A_2) is shown and the onset has been shifted to $t = 0$. In this case, the experimental data conform to a complex pattern that suggests the presence of various processes including desorption and/or reorientation of molecules adsorbed on the electrode, reduction of molecules diffusing to it —followed by precipitation of the resulting salt— and also, probably, the process that yields peak D_1. Available models did not allow us to unequivocally establish the mechanism for these processes. However, we continue our search for mathematical models that may provide an accurate explanation.
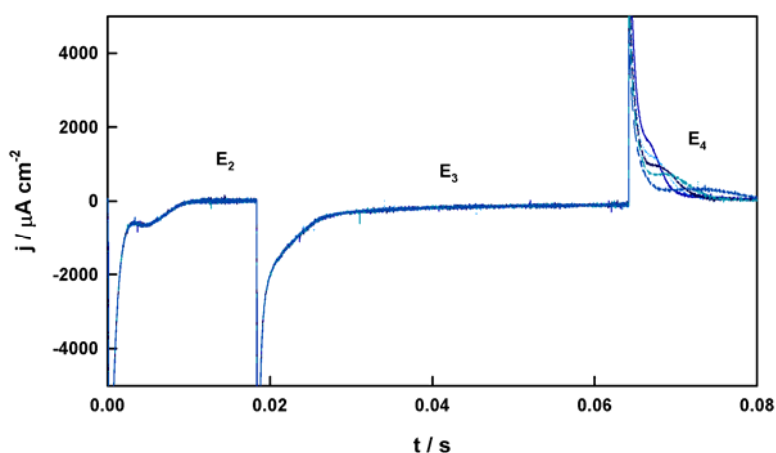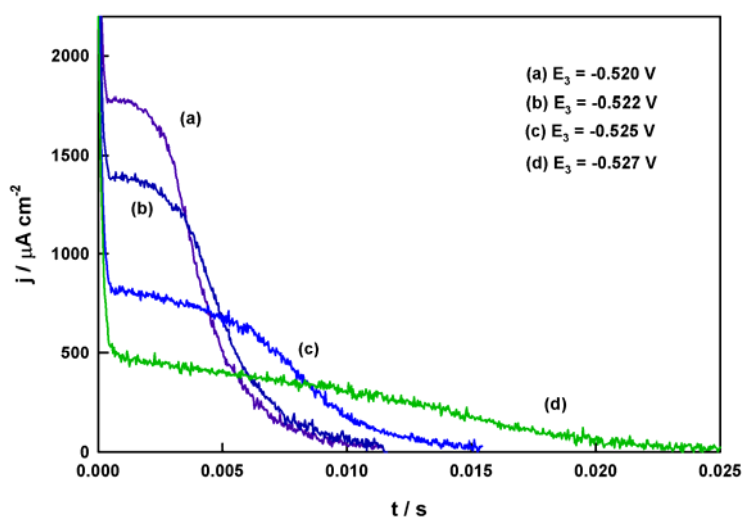
Figure 13. Experimental double-potential step j–t curves obtained under the same experimental conditions as in Fig. 6, but E_2 = –0.54 V for a time τ = 0.03 s and variable E_3 values. For clarity, only the second jump is shown and the onset has been shifted to t = 0.

Mechanism behind the formation and destruction of phase γ. Based on the previous results, we believe that, at potentials more positive than that of appearance of voltammetric peak A_1, the adsorption process must preferentially involve adsorption of I^- ions on the electrode, and random adsorption of EtV^{2+} molecules, as reflected in the fact that the capacitance in this zone is higher than that of the supporting electrolyte in the absence of EtV^{2+} (zone I in Fig. 3b). After peak A_1 appears, phase γ forms via a capacitive instantaneous 2D nucleation process that must include desorption of the molecules initially adsorbed on the electrode. However, the prior desorption does not seem to affect the shape of the j–t curve except for the induction time, t_r (*i.e.* the overall process is governed by nucleation). This phase appears to consist of some ion–pair formed between I^- and EtV^{2+} in a 1:1 ratio that results in a highly ordered

structure relative to the initial one. Although we have no spectroscopic evidence in support of the presence of EtV^{2+}, the possibility of the condensed phase consisting of the cation radical, similarly to other viologens, can be ruled out since, as noted earlier, the charge of peak A_1 is too small. The formation of the positively charged phase may be favoured by specific adsorption (i.e. non electrostatic) of this phase on Hg; any such interaction, however, must be weak as the phase never forms above 9 ºC.

The phase destruction process, which corresponds to voltammetric peak B_1, is strongly affected by the prior desorption of the molecules; in fact, the shape of the *j–t* curves is consistent with a more complex mechanism. Thus, voltammetric and *C–E* measurements revealed that phase γ is destroyed via a seemingly simple capacitive process involving cleavage of the ion-pair between I^- and EtV^{2+}. After phase γ is destroyed, EtV^{2+} molecules must be adsorbed on the electrode at potentials less positive than that of appearance of peak B_1 via an organized structure rather than in a random manner; Figure 3a shows that the capacitance values obtained immediately after peak B_1 (zone III) were lower than those preceding peak A_1 (zone I). However, the chronoamperometric study revealed that the destruction of phase γ is in fact a more complex process that involves two consecutive steps. First, as the applied potential becomes more negative, the concentration of I^- and/or EtV^{2+} on the electrode surface changes —the electrode probably releases I^- ions and adsorbs EtV^{2+} ions—; this results in rearrangement of the $EtV^{2+}–I^-$ structure (*i.e.* a capacitive phenomenon). At even more negative potentials, the ion-pair is destroyed and the EtV^{2+}

molecules released are adsorbed by the electrode and immediately reduced to the cation radical via either a prior desorption–nucleation process or direct slow reorientation (*i.e.* a Faradaic phenomenon). As can be seen from the onset of diffusion peak C in the voltammogram of Fig. 1a, direct reduction of EtV^{2+} molecules by diffusion is seemingly hindered by the formation of phase γ, so rupture of the phase is immediately followed by reduction.

One alternative explanation relies on the presence of peak D_1. Its charge, *ca.* 5-6 μC cm^{-2}, may fulfil the condition that the total charge of $A_1 + B_1 + D_1$ (≈ 12 μC cm^{-2}) would correspond to a *quasi*-monolayer amount of $EtV^{.+}$. This situation would be similar to that reported by Arihara and Kitamura [29], who obtained multiple spike peaks in the reductive phase transition of HV at an Au(111) electrode. This interpretation, however, must be excluded since, as shown in Fig. 1b, peak D_1 was in no way altered by the disappearance of processes A_1 and B_1. Clearly, therefore, these two processes are not independent (i.e. they do not seem to constitute two different steps in the formation of a condensed phase of the cation radical). Rather, peak D_1 appears to be related to E_1 via the formation–destruction of a new condensed phase of either the cation radical or the radical dimer. The fact that peaks D and E were overlapped with the diffusion process precluded the obtainment of more conclusive results in this respect.

Finally, we should note that EtV^{2+}/I^- is the first known system seemingly forming condensed phases of the viologen dication; in all previously studied systems, the condensed phase was formed by the cation radical resulting from

the electrochemical reduction of the dication.

Conclusions

The electrochemical study of ethyl viologen on mercury in iodide media results in the formation of a 2D phase prior to the reduction of the EtV^{2+} dication by diffusion. Such a phase is seemingly formed by an organized structure (an ion-pair between the EtV^{2+} dication and the I^- anion in the medium in a 1:1 ratio). The phase formation, which reflects in voltammetric peak A_1 or B_2, is a simple capacitive instantaneous 2D nucleation process probably involving desorption of the molecules initially adsorbed on the electrode. On the other hand, its destruction, which yields voltammetric peak A_2 or B_1, is a more intricate process the kinetics of which is complicated by the involvement of various phenomena.

Acknowledgements

References

[1] F.L. Rodkey and J.A. Donovan, *J. Biol. Chem.*, 234, 677 (1959).

[2] T. Kuwana and M. Ito, *J. Electroanal. Chem.*, 198, 415 (1972).

[3] F. Rauwel, *J. Electroanal. Chem.*, 75, 579 (1977).

[4] J.F. Castner and F.M. Hawkridge, *J. Electroanal. Chem.*, 143, 217 (1983).

[5] J. Hadjian, R. Pilard and P. Bianco, *J. Electroanal. Chem.*, 184, 391 (1985).

[6] J.F. Wei and M.D. Ryan, *Anal. Biochem.*, 106, 269 (1980).

[7] W.J. Albery, M.J.Eddowes, H.A.O.Hill and A.R. Hillman, *J. Am. Chem. Soc.*, 103, 3904 (1981).

[8] I. Taniguchi, K. Toyosawa, H. Yamaguchi, and K. Yasukouchi, *J. Chem. Soc., Chem. Comun.*, 1032 (1982).

[9] A.G. Evans, N.K. Dodson and N.H. Rees, *J. Chem. Soc, Perkin Trans. II*, 859 (1976).

[10] A.J. Bard and A. D. Abruña, *J. Am. Chem. Soc.*, 103, 6898 (1981).

[11] V.J. Razuman, A. V. Gudavicius and J. J. Kulys, *J. Electroanal. Chem.*, 198, 81 (1986).

[12] K.K. Park, C.W. Lee, S.Y. Oh and J. W. Park, *J. Chem. Soc., Perkin Trans. I*, 2356 (1990).

[13] J.W. Park, M.H. Choi and K. K. Park, *Tetrahedron Lett.*, 36, 2637 (1995).

[14] F.T. Liu, X.D. Yu, L.B. Feng and S. B. Li, *Eur. Poly, J.*, 31, 819 (1995).

[15] E.F. Bowden, F.M. Hawkridge and H. N. Blout, *Bioelectrochem. Bioeng.*, 447, 7 (1980).

[16] F.T. Liu, B.L. He, L.J. Liang and L. B. Feng, *Eur. Poly, J.* 33, 311 (1997).

[17] J.M. Zen, S.H. Jeng and H. J. Chen, *J. Electroanal. Chem*. 408, 157 (1996).

[18] J.I. Millán, M. Sánchez-Maestre, L. Camacho, J. J. Ruiz and R. Rodríguez-Amaro, *Langmuir*, 13, 3860 (1997).

[19] F. Kitamura, T. Osaka and K. Tokuda, *J. Electroanal. Chem.*, 347, 371 1993.

[20] J.I. Millán, R. Rodríguez-Amaro, J. J. Ruiz, and L. Camacho, *Langmuir*, 15, 618 (1999).

[21] J.I. Millán, R. Rodríguez-Amaro, J. J. Ruiz, and L. Camacho, *J. Phys. Chem. B* 103, 3699 (1999).

[22] K. Kobayashi, F. Fujisaki, T. Yoshimine and K. Niki, *Bull.Chem. Soc. Jpn.*, 59, 3715 (1986).

[23] R. Salas, M. Sánchez-Maestre, R. Rodríguez-Amaro, E. Muñoz, J. J. Ruiz and L. Camacho, *Langmuir*, 11, 1791 (1995).

[24] L. Gómez, J.J. Ruiz, L. Camacho and R. Rodríguez-Amaro, Langmuir 21,

369, (2005)

[25] J.I. Millán, J.J. Ruiz, L. Camacho and R. Rodríguez-Amaro, Langmuir 19, 2338, (2003)

[26] K. Arihara, F. Kitamura, T. Osaka, and K. Tokuda, *J. Electroanal. Chem*., 488, 117 (2000).

[27] A. Bewick, D. W. Cunningham and A. C. Lowe, *Makromol. Chem., Macromol. Symp.*, 8, 355 (1987).

[28] M. Tominaga, *Abstracts of the 36th Joint Meeting of Kyushu Divisions of Chemical Societies,* 4.63, 96 (1999).

[29] K. Arihara and F. Kitamura, *J. Electroanal. Chem*., 550–551, 149 (2003).

[30] D. Mayer, Th. Dretschkow, K. Ataka and Th. Wandlowski, *J. Electroanal. Chem*., 524–525, 20 (2002).

[31] Th. Wandlowski, K. Ataka, and D. Mayer, *Langmuir*, 18, 4331 (2002).

[32] K. Arihara, F. Kitamura, K. Nukanobu, T. Osaka and K. Tokuda, *J. Electroanal. Chem*., 473, 138 (1999).

[33] T. Sagara, S. Tanaka, Y. Fukuoka and N. Nakashima, *Langmuir*, 17, 1620 (2001).

[34] C. L.Bird and A. T. Huhn, *Chem. Soc. Rev.,* 10, 49 (1981).

[35] P.M.S. Monk, *The Viologens*, John Wiley & Sons, Chichester (1998).

[36] M. Sánchez-Maestre R. Rodríguez-Amaro E. Muñoz, J. J. Ruiz and L. Camacho, *J. Electroanal. Chem.*, 373, 31 (1994).

[37] I. Prieto, M. T. Martín, E. Muñoz, J. J. Ruiz and L. Camacho, *J. Electroanal. Chem.*, 424, 113 (1997).

[38] Th. Wandlowski and R. De Levie, *J. Electroanal. Chem.*, 349, 15 (1993).

[39] R. Sridharan, R. De Levie and S. K. Rangarajan, *Chem. Phys. Lett.*, 142, 43 (1987).

[40] U. Retter and H. Lohse, *J. Electroanal. Chem.*, 134, 243 (1982).

[41] P. Nikitas and S. Andoniou, *J. Electroanal. Chem.*, 375, 339 (1994).

[42] I. Prieto, M. T. Martín, E. Muñoz and L. Camacho, *J. Phys. Chem.*, 99, 14083 (1995).

[43] Th. Wandlowski, B. J. Geoffrey and R. De Levie, *J. Phys. Chem.*, 97, 10119 (1993).

[44] M. Fleischmann and H. R. Thirst, in *Advances in Electrochemistry and Electrochemical Engineering*: P. Delahay, Editor, Vol. 3, Interscience, New York, (1963).

[45] J. A. Harrison and H. R. Thirst, in *Electroanalytical Chemistry*: A. J. Bard, Editor, Vol. 5, p. 67, Marcel Dekker, New York, (1977).

[46] A. Bewick, M. Fleischmann and H. R. Thirsk, *Trans. Faraday Soc.*, 58, 2200 (1962).

[47] C. Donner and L. Pohlmann, *Langmuir*, 15, 4898 (1999).

[48] C. Donner and L. Pohlmann, *Langmuir*, 15, 4907 (1999).

[49] R.D. Armstrong and J. A. Harrison, *J. Electrochem. Soc.*, 116, 328 (1969)

[50] S. K. Rangarajan, *J. Electroanal. Chem.*, 46, 124 (1973).

[51] M. Avrami,. *J. Chem. Phys*., 7, 1103 (1939).

[52] M. Avrami, , *J. Chem. Phys*., 8, 212 (1940).

[53] M. Avrami, , *J. Chem. Phys*., 9, 177 (1941).

[54] M. Noel, S. Chandrasekaran and C. Ahmed Basha, *J. Electroanal. Chem*., 225, 93 (1987).

CAPÍTULO V:

TRANSICIONES DE FASE TRIDIMENSIONALES SOBRE ELECTRODO DE CARBÓN VITRIFICADO.

5.1. ELECTROCHEMICAL AND SPECTROELECTROCHEMICAL BEHAVIOR OF THE TCNQ$^{0/-}$ COUPLE ON A GLASSY CARBON ELECTRODE. LAYER-BY LAYER NUCLEATION AND GROWTH

Abstract

Based on the electrochemical results obtained for thin films of 7,7,8,8-tetracyanoquinodimethane (TCNQ) on a glassy carbon electrode, the reduction and oxidation of the [TCNQ]$^{0/-}$ couple in KCl aqueous media occurs via a mechanism involving layer-by-layer nucleation and growth. *In situ* recorded UV–visible spectroelectrochemical data allow two different crystal structures for the oxidized form of TCNQ to be discriminated.

Introduction.

7,7,8,8-Tetracyanoquinodimethane (TCNQ) forms organic conductors including radical and charge-transfer salts. In recent years, TCNQ has been the subject of many electrochemical and spectroscopic studies on account of its high potential for use in electrodes,[1–10] potentiometric sensors,[11,12] high-density molecular-based information storage media[13] and electrochromic devices.[14] Obviously, the performance of this compound depends strongly on its state of aggregation and is especially attractive in the solid state. Thus, solid TCNQ and its reduced salts have been used as single-crystal working electrodes;[1,2,10] mixed with carbon paste[15] or silicone oil;[5] coated on Nafion;[16] and attached to electrode surfaces by direct adhesion[7,17–20] or electrochemical deposition.[21,22]

The previous studies have revealed that the voltammetry of the $[TCNQ]^{0/-}$ couple is largely controled by a nucleation–growth mechanism. This conclusion has been confirmed by chronoamperometric tests.[10,17,19] However, the kinetics of these processes is complex and dependent on the amount of mass (layers) that is subjected to the redox cycle;[19] this makes it especially interesting to expand available knowledge on the formation mechanism for TCNQ organized films.

In this work, we conducted an electrochemical and spectroelectrochemical study on TCNQ adsorbed on the surface of a glassy carbon electrode. To this end, the compound was dissolved in an organic solvent and deposited onto the electrode surface by evaporating the solvent.

With a small amount of adsorbate (i.e., a thin film), the nucleation–growth processes involved in the reduction of $TCNQ^0$ to $TCNQ^-$ and its reoxidation to $TCNQ^0$ in the presence of KCl as electrolyte can be explained in the light of a recently reported mathematical model.

Experimental Section

Materials. 7,7,8,8-Tetracyanoquinodimethane (99%) and KCl (> 99.5%) were supplied by Aldrich Chemical Co. and used as received. Acetone was supplied by Merck in 99.5% purity. All aqueous solutions were made in Milli-Q water.

Instrumentation. Electrochemical recordings were obtained by using an AUTOLAB PGSTAT30 potentiostat/galvanostat equipped with SCAN-GEN and FRA2 modules in addition to an FI20 integration module controlled via GPES and FRA software. The working electrode was a glassy carbon disc with a surface area of 0.196 ± 0.005 cm^2, the auxiliary electrode Pt and the reference electrode Ag|AgCl (3.0 M KCl). All potentials given are referred to this electrode.

UV–visible spectra were obtained with an AVANTES SH2000 fiber optic spectrophotometer equipped with a CCD that enabled recording of instantaneous spectra of the electrode coating at intervals as short as 1 s.

In situ spectroelectrochemical measurements were made with the fiber optic spectroscopic probe normal to the surface of the working electrode.

The temperature was measured to within ± 0.1 °C in all instances.

Procedure. In order to maximize coating uniformity over the glassy carbon, we used a 3.5 mM solution of TCNQ in acetone, preparation of which required the application of ultrasound to ensure appropriate dissolution. A fresh solution was prepared on a daily basis in order to avoid potential stability problems. A mirror-like glassy carbon electrode surface was obtained by polishing with alumina in decreasing grain sizes from 1 μm to 0.05 μm. Then, the electrode was cleaned in an ultrasonic bath. Once the electrode and solution were prepared, a micropipette was used to deposit a 10 μl drop ($3 \cdot 10^{-8}$ mol) over the glassy carbon surface. A thin film of TCNQ thus formed as the acetone evaporated that was easily identified by its bright yellowish color. At that point, the modified electrode was ready for placement in the electrochemical cell.

The following procedure was adopted in order to prevent the initial double layer charging current from contributing to the experimental j–t transients: after the experimental current, j_{exp}, was measured in each experiment, a similar j–t transient in an adjacent potential region involving no electron transfer was also measured. This ensured that only the double layer charging current, j_{dl}, was measured. In this way, the resulting $j_T = j_{exp} - j_{dl}$ was fitted to the theoretical model described below. This procedure has proved more accurate than an exponential decay curve for fitting the initial j_{exp} points.

Results and discussion

Figure 1 shows a selected cyclic voltammogram for TCNQ in 0.1 M KCl obtained after 10 previous cycles over a glassy carbon electrode at a scan rate v = 1 mVs^{-1}, a temperature of 20 $^{\circ}$C and potentials over the range 0.4 to 0 V. As can be seen, the cathodic (forward) scan provided a single, narrow peak (A) and the anodic (reverse) scan its matching oxidation peak (B). The two peaks are similar in area, which suggests a high chemical reversibility; also, the voltammogram exhibits an "inert zone" (*viz.* a range of applied potential where no faradaic reaction occurs) that is typical of solid–solid phase transformation at a rate controlled by nucleation and growth.[16]
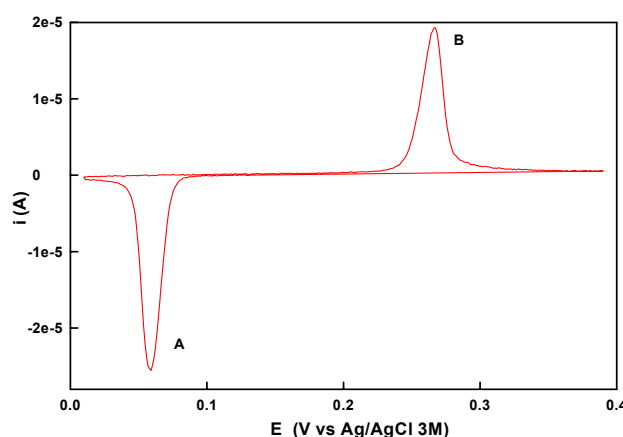
Figure 1. Steady-state cyclic voltammogram for TCNQ attached to a glassy carbon electrode in 0.1 M KCl as obtained at a scan rate v = 1 mVs^{-1} at 20 $^{\circ}$C after 10 cycles.

These peaks have previously been examined fairly extensively (particularly by Bond et al.[16,17,18,20]) and assigned to the following reaction:

$$TCNQ_{(solid)} + e^- + K^+_{(aq)} \leftrightarrow K^+(TCNQ)^-_{(solid)} \tag{1}$$

based on which the reduction process is accompanied by insertion of K$^+$ cations

from the electrolyte solution into the solid material in order to maintain charge neutrality. These voltammetric results were obtained after a series of redox cycles (usually 5 to 10); in fact, the first few cycles provided highly complex, irreproducible voltammograms exhibiting a "diffusion tail" that was more apparent in the cathodic process than in the anodic one. This was probably a result of the asymmetry in the electrode reaction with respect to the cation uptake (reduction) and loss (oxidation), and also of solubility differences between the reduced and oxidized forms.[18] Successive redox cycling reduced the current, but the principal features of the voltammogram were retained.
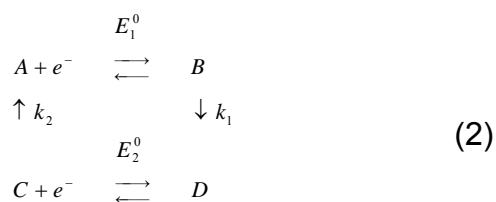
Raising the temperature favored reduction (peak A, which appeared at less negative potentials) at the expense of oxidation (peak B, which appeared at more positive potentials). Also, it resulted in faster loss of the electrode coating, probably through dissolution of the KTCNQ salt formed. A temperature of 20 °C was therefore adopted for subsequent work.

The large peak potential difference, $E_p(A) - E_p(B)$, observed (*ca.* 200 mV) can be explained by assuming the following square scheme:[19]

$$
\begin{array}{ccc}
 & E_1^0 & \\
A + e^- & \underset{\longleftarrow}{\overset{\longrightarrow}{\rightleftharpoons}} & B \\
\uparrow k_2 & & \downarrow k_1 \\
 & E_2^0 & \\
C + e^- & \underset{\longleftarrow}{\overset{\longrightarrow}{\rightleftharpoons}} & D
\end{array}
\qquad (2)
$$

with $E_1^0 < E_2^0$. k_1 and k_2 denote the rate constants of the chemical steps B → D and C → A, respectively.

The phases that grow and intersect in the scheme correspond to the two

redox states considered in eq. 1.

One way of characterizing nucleation is by analysing the variation of voltammetric peaks with the scan rate in the light of the theoretical model for 2D nucleation and growth previously developed by our group.[23,24] In this work, we analysed the nature of peaks A and B by examining changes in peak currents (I_p) and peak widths at half-height (W) with the scan rate (v) and found plots of log I_p and log W *versus* log v (not shown) to be roughly linear for both peaks; their slopes are given in Table 1. We also analysed hysteresis [*viz.* the separation between peak potentials, ΔE_p = E_p(A) − E_p(B)]. A plot of log ΔE_p *versus* log v was also near-linear (see slopes in Table 1).

Table 1. Voltammetric data for the nucleation peaks as obtained at T = 20 ºC and v values from 1 to 10 mVs^{-1}

Peak	∂log I_p/∂ log v	∂log W/∂ log v	∂log ΔE_p/∂ log v
A	0.65 ± 0.01	0.46 ± 0.02	0.1 ± 0.01
B	0.48 ± 0.05	0.30 ± 0.05	

Except for the hysteresis values, the data in Table 1 are close to the theoretical values for 2D phase transitions on electrodes. Consequently, log–log plots of I_p, W and ΔE_p as a function of v must all be linear and have slopes of x, 1 − x and 1 − x, respectively, where x is 0.6 in the ideal situation[23] (*viz.* a high nucleation rate and a low scan rate) or slightly greater than 0.6.[23,25,26] Therefore, peaks A and B must essentially be the result of 2D nucleation processes the rate-determining step of which is the incorporation of additional molecules to growing nuclei —the overall process, however, must be more

complex than this.

In order to extract additional information about the nature of these processes, we ran capacitance-potential curves. Figure 2 (solid line) shows the experimental curve obtained after 10 voltammetric cycles. As can be seen, it exhibits relative capacitance maxima at potentials corresponding to the appearance of both peak A and B, and arising from the faradaic component of the redox process. In the cathodic scan, the maximum is followed by a gradual decrease in capacitance to the baseline value; in the anodic scan, however, the maximum is followed by an abrupt drop in capacitance. In addition, the capacitance values in the region of occurrence of the oxidized form $TCNQ^0$ are even lower than those for the background electrolyte with a bare working electrode (no TCNQ attached, dashed line). This suggests that the oxidized form is structurally more compact than the reduced form.
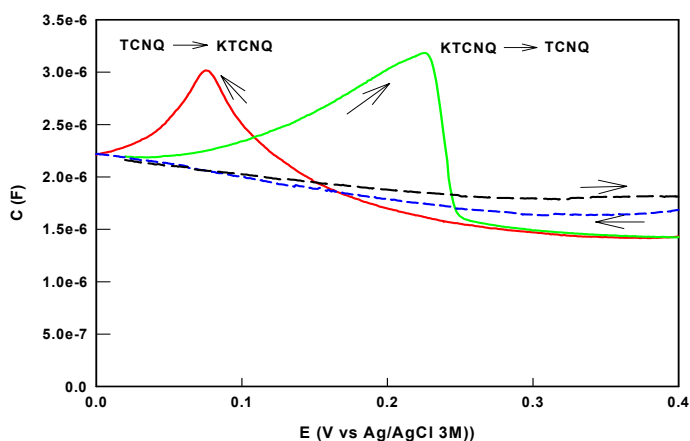

Figure 2. Plots of *C* as a function of *E*. *C* was measured by using a potential pulse of 10 mV, a potential step of 1 mV and a frequency of 77 Hz. The dashed line corresponds to a bare working electrode in a 0.1 M KCl solution and the solid line to TCNQ attached to a glassy carbon electrode in the same solution, after 10 voltammetric cycles.

Chronoamperometry

Kinetic information for the processes corresponding to voltammetric peaks A and B can be obtained chronoamperometrically.[27,28] Figure 3 shows selected experimental j–t curves for both peaks as obtained for aqueous solutions containing 0.5 M KCl at 20 °C. These experimental curves were obtained by applying a potential from E_1 = 180 mV to E_2 = 70 mV (peak A), or from E_3 = 150 mV to E_4 = 280 mV (peak B). Experimental data were collected following application of 10 cycles of the potential range.

Figure 3. Selected experimental j–t curves for peaks A and B as obtained for an aqueous solution containing 0.5 M KCl at 20 °C. These curves were experimentally obtained by applying a potential from E_1 = 180 mV to E_2 = 70 mV (peak A) or from E_3 = 150 mV to E_4 = 280 mV (peak B). Experimental data were collected after application of 10 cycles of the potential range.

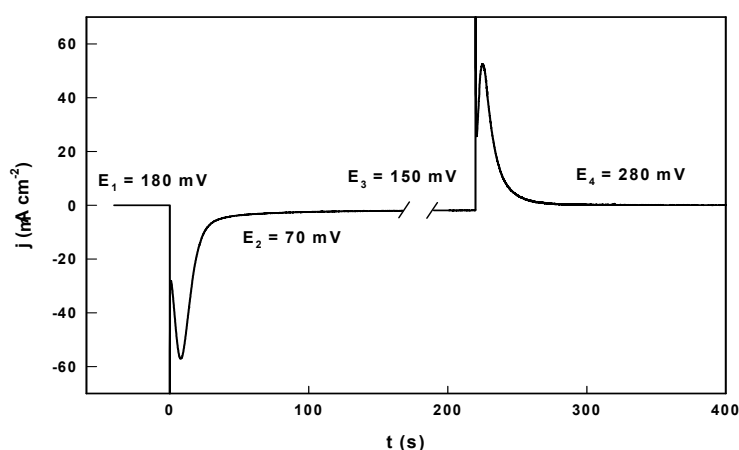Although both curves exhibit typical maxima that allow the underlying nucleation processes to be characterized, they possess a complex form that precludes fitting to simple 2D or 3D nucleation models. This problem was also encountered in some previous studies.[16,19]

Taking into account that processes A and B are associated with many equivalent monolayers of surface-attached material, nucleation and growth must occur via a 2D layer-by-layer (Frank–van der Merwe model) or 3D mechanism (Volver–Weber model).[29] With 2D growth, nuclei —which are often assumed to be circular discs— grow more quickly in the parallel direction within a monolayer than they do in the normal direction until they meet and overlap. With 3D growth, nuclei grow at comparable rates in the directions parallel and normal to the electrode surface. Whether a given system adopts 2D or 3D growth depends on the strength of the interaction between the substrate and deposited molecules.

The shape of the voltammetric peaks was found to depend strongly on the amount of TCNQ deposited onto the electrode. With fairly small amounts, the peaks were well-defined (see Fig. 1); as the amount adsorbed increased, however, the peaks became increasingly ill-defined and resembled those typical of an amorphous precipitate. This indicates a change in the mechanism or the combined action of several and is potentially consistent with a Stranski-Krastanov (2D + 3D) mechanism,[29] which combines 2D and 3D growth. As a result of the high interaction energy involved, layer-by-layer growth (FM model) will occur at the initial stage of deposition. However, if the size of the molecule and substrate are significantly different, lattice mismatch will increase with increasing number of adlayers. At some point, the FM model will no longer be favorable and 3D growth will start. This assumption is supported by the results of Chambers et al.[10] for electrodes prepared from needles of TTF-TCNQ single

crystals. In this system (macroscopic crystals), the current–time transients for the TCNQ$^{0/-}$ couple were much more consistent with 3D instantaneous nucleation and diffusion control of the growth process.

The mathematical model used here is based on that of Armstrong and Harrison,[30] who assumed 2D layer-by-layer growth. In their treatment, the current density for the first layer, j_0, is given by the Bewick–Fleischmann–Thirsk (BFT) model:[27,31]

$$j_0 = nq_m\beta_0 t^{n-1}e^{-\beta_0 t^n} \tag{3}$$

and that for successive layers by

$$j_i = n\beta_i \int_0^t (t-u)^{n-1} e^{-\beta_i(t-u)^n} j_{i-1}(u)du \qquad for\ i \geq 1 \tag{4}$$

where constants β_i are related to the growth rate for each layer —which can in theory differ between layers—, q_m is the charge involved in the nucleation process and usually corresponds to a monolayer; and n is a constant that depends on the nature of the nucleation process and is 2 for instantaneous nucleation and 3 for progressive nucleation.

The overall current density,

$$j_T = j_0 + \sum j_i \tag{5}$$

can be calculated by numerical desk calculator integration.

This model predicts a steady-state current at long times. As with the system described in ref. 32, however, the current density drops to zero owing to

the limited amount of substance covering the electrode, which can be ascribed to incomplete coverage by some monolayers in each step (reduction or oxidation) of the redox cycle. Thus, the nuclei formed in previous chronoamperometric cycles can be represented in a rough approximation as pyramids or cones. The drop in current density has been simulated by using the following mathematical expression:[32]

$$\theta_i = \frac{1}{1 + e^{a(i-m)}} \tag{6}$$

where a and m are two empirical parameters. If l is taken to be the number of full monolayers, then j_i will be given by eq. 4 at $i < l$; on the other hand, at $i \geq l$, the current density of monolayer j_i will be given by eq. 4 times the value of θ_i as defined in eq. 6.

Figures 4 and 5 show selected experimental (symbol) curves corresponding to voltammetric peaks A and peak B, respectively, as obtained at variable numbers of cycles —the overall charge decreased with cycling— following suppression of the initial charging current density term, j_{dl}.
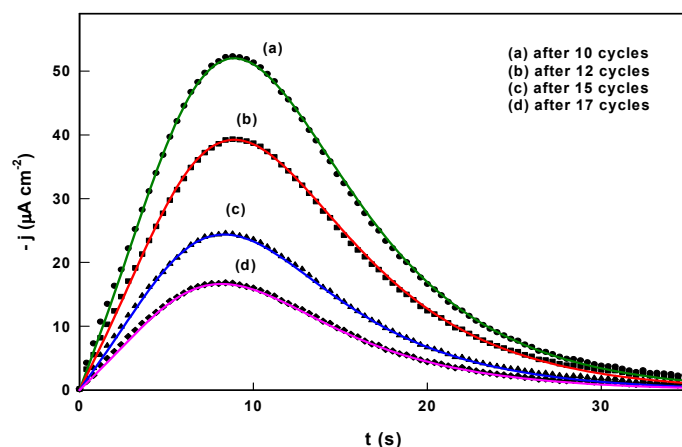
Figure 4. Selected experimental (symbols) j–t curves for the reduction process as obtained after a variable number of voltammetric cycles and suppression of the initial charging current term, j_{dl}. E_{in} was 180 mV and E_f 70 mV. Solid lines represent the simulated results provided by the model based on eq. 5.

Figure 5. Selected experimental (symbols) j–t curves for the oxidation process as obtained after a variable number of voltammetric cycles and suppression of the initial charging current term, j_{dl}. E_{in} was 150 mV and E_f 280 mV. Solid lines represent the simulated results provided by the model based on eq. 5.

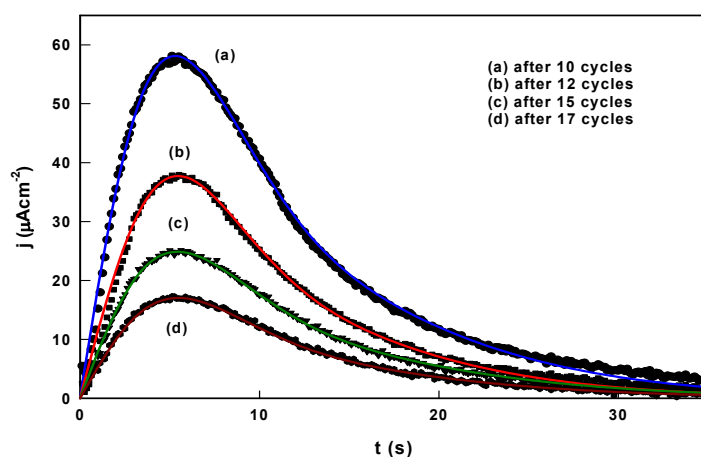In the initial portion ($t \rightarrow 0$), all log (j-j_{dl}) vs log t curves in Figs 4 and 5 are roughly linear and have a unity slope (data not shown). This suggests that nucleation is essentially two-dimensional and instantaneous (n = 2) at the

beginning.

The solid lines in Figures 4 and 5 are the simulated curves provided by the proposed mathematical model. As can be seen, the theoretical and experimental curves are quite consistent. Tables 2 and 3 show their figures of merit. As can be seen, both reduction and oxidation take place at a growth rate that is somewhat lower for the first layer (specially in the reduction process), but identical for all subsequent layers. Also, the growth rates for processes A and B are of the same order of magnitude, which suggests that diffusion of K through the crystal lattice is unfavourable both in the reduction (incorporation) process and the oxidation (release) process.

Table 2. Figures of merit of the mathematical fitting of the experimental curves of Fig. 4 to the proposed model, based on eq. 5. For all curves, $l = 1$, $a = 0.7$, $m = 1.7$ and $\beta_1 = \beta_2 = \ldots = \beta_i$

After cycle	q_m /µC cm^{-2}	$\beta_0 \times 10^4$ /s^{-1}	$\beta_i \times 10^4$ /s^{-1}
10	253	145	680
12	191	145	680
15	113	168	700
17	76	175	700

Table 3. Figures of merit of the mathematical fitting of the experimental curves of Fig. 5 to the proposed model, based on eq. 5 For all curves, $l = 1$, $a = 0.7$, $m = 1.7$ and $\beta_1 = \beta_2 = \ldots = \beta_i$

After cycle	q_m /µC cm^{-2}	$\beta_0 \times 10^4$ /s^{-1}	$\beta_i \times 10^4$ /s^{-1}
10	225	420	600
12	140	410	690
15	97	410	680
17	66	400	600

The application of the mathematical model to the studied system warrants some comment. Thus, strictly speaking, the BFT model can only be applied if the rate-determining step involves the exchange of ad-molecules at the periphery of expanding sites. Although this is reasonable for the first monolayer, it need not be for multiple layers, across which ions must be transported during redox processes. One possible explanation is that, only when the film is thick enough can the transport process be the rate-determining step; until then (initial layers), the model would be quite applicable. Also, the word "layer" should be used in its broadest sense here. Thus, based on Table 2, the charge for the first layer (*ca.* 150 µC cm^{-2} as intermediate value) must in fact correspond to a "crystal zone" exhibiting a uniform behaviour (*i.e.,* the word "layer" here should be used to designate a crystal zone or region of a given thickness).

Based on the unit cell volume per molecule of TCNQ reported by Bond et al.,[16] 280 Å^3, and assuming a monoclinic space group for TCNQ and its salt KTCNQ, the thickness of the layer can be estimated to be *ca*. 26 Å. Although this value should be taken cautiously because it relies on some approximations, each crystal zone or layer would in fact consist of about 3 monoclinic cells, which is consistent with the definition of thin layer used in the proposed mathematical model.

The effect to the step overpotential was also examined. Figure 6 (symbols) shows selected experimental *j–t* curves for peak A obtained from E_{in} = 180 mV to variable E_f values following suppression of the initial charging

current density term, j_{dl}. These simulated curves provided by the proposed model show that fitting to the experimental data worsens with increasing step overpotential. Thus, consistency between the predicted data (solid lines) and their experimental counterparts was very good at E_f values of 80, 70 and 60 mV (see Table 4); on the other hand, fitting of the data obtained at E_f values of 50 and 40 mV was incomplete.
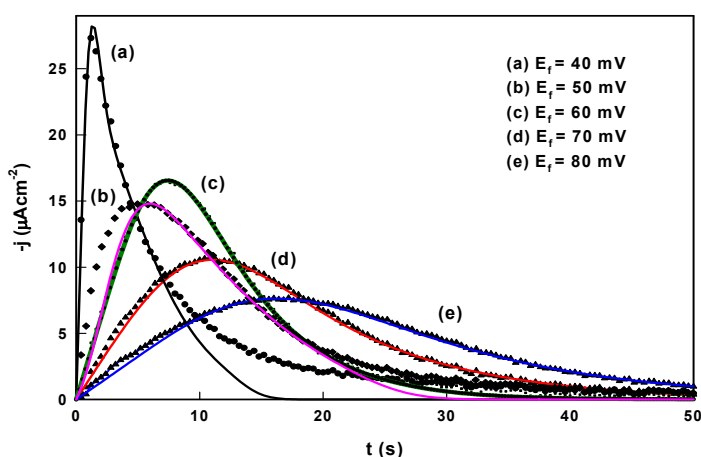

Figure 6. Selected experimental (symbols) j–t curves for the reduction process as obtained at variable E_f values following suppression of the initial charging current density term, j_{dl}. E_{in} was 180 mV. Solid lines represent the simulated results provided by the model based on eq. 5.

Table 4. Figures of merit of the mathematical fitting of selected experimental curves of Fig. 6 to the proposed model, based on eq. 5. For all curves, l = 1, a = 0.7, m = 1.7 and $\text{ß}_1 = \text{ß}_2 = \dots = \text{ß}_i$

E_f /mV	ß_0 x 10^4 /s^{-1}	ß_i/ß_0
60	215	3.5
70	89	3.5
80	45	3.5

These results show that changing the step overpotential alters the nucleation mechanism. Thus, at some overpotential values, the mechanism

remains virtually unchanged and the sole effect is acceleration of the process at increased overpotentials. As can be seen in Table 4, the β_i/β_0 ratio was virtually independent of the final step potential. On the other hand, above a given overpotential threshold, the nucleation–growth mechanism changed by effect of changes in ion mobility and the layer-by layer growth mechanism based on the 2D BFT model was no longer applicable.

The results obtained by changing the overpotential of the *j–t* curves for peak B (figure not shown) were similar to the previous ones. Thus, the model held over a certain overpotential range within which applying a higher overpotential only accelerated the overall process without altering the β_i/β_0 ratio. However, the process was complicated by an additional phenomenon: the lower the applied overpotential was, the faster was the loss of mass from the electrode —so much so that the whole coating disappeared within a few cycles.

Spectroelectrochemistry

One of the primary aims of this work was to obtain evidence confirming the presence of the species involved in eq. 2. To this end, we fitted a UV–visible spectrophotometer to our electrochemical cell.

Spectrum (a) in Fig. 7 shows the baseline used as reference to record subsequent spectra, which corresponds to the surface of the bare working electrode immersed in 0.5 M KCl. Spectrum (b) in the figure corresponded to TCNQ adsorbed on the electrode and immersed in the same solution. This spectrum is similar to that obtained by Chambers et al. [7] for 9-

AMACH(TCNQ)$_2$ on a gold-on-quartz OTE in the 200–450 nm region; however, both spectra differ above 450 nm. Spectrum (c) was obtained at 180 mV after 10 redox cycles in order to allow the system to reach steady state. As can be seen, the absorbance in the region 280–350 nm was higher, so measurements over the range 280 to 450 nm were virtually identical.
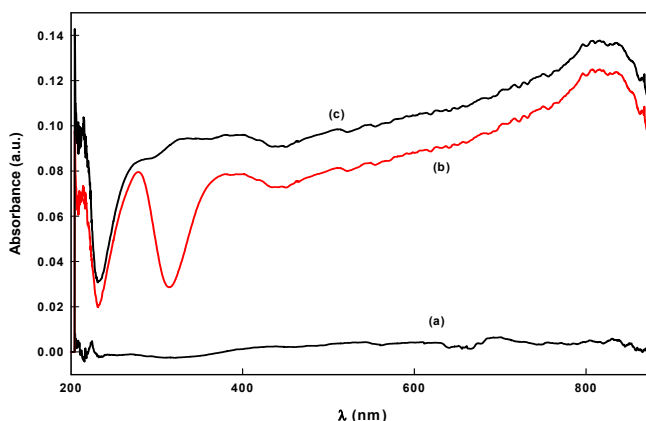

Figure 7. *In situ* recorded electronic absorption spectra obtained in 0.5 M KCl. (*a*) Spectrum obtained on the bare working electrode, which was used as reference (baseline) for the others. (*b*) Spectrum for TCNQ attached to a glassy carbon electrode. (c) Spectrum of the previous system as obtained after 10 voltammetric cycles at 180 mV.

Spectral changes with the potential were examined by using spectrum (c) in Fig. 7 as baseline; therefore, all other spectra reflect the absorbance differences from it. Thus, lowering the potential from 180 to 50 mV caused the reduction of TCNQ^0 to TCNQ$^-$, but the spectrum (not shown) remained unchanged even after maintaining the potential for quite a long time. If the potential was then raised to 280 mV, TCNQ$^-$ was oxidized to TCNQ^0 (peak B) and the resulting spectrum exhibited a new peak centered at about 400 nm and typical of neutral TCNQ.[33] If the potential was then maintained at 280 mV, the

absorbance of the new peak increased with time, τ, up to a maximum at 50 s. Then, the absorbance decreased up to τ ≥ 150 s, after which it levelled off. Figure 8 depicts these changes.
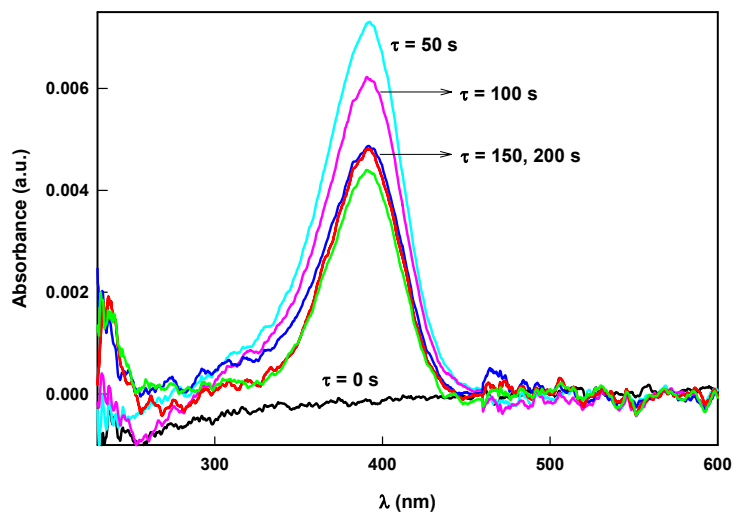

Figure 8. Variation of the spectra for the process giving peak B. Spectra were recorded at a potential of 280 mV and a variable time τ.

This peak must be related to the presence of a new solid structure of $TCNQ^0$. In fact, if the potential is now lowered from 280 to 180 mV (the value at the start of the cycle), the spectrum regains its initial shape (i.e., the baseline). With thin films of this nature, a slow loss of electrolyte or solvent may alter the spectra by effect of a change in pathlength or effective sample depth. In our case, such a possibility can be ruled out because the baseline remained constant throughout the electrochemical process. This is also supported by studies currently in progress involving other cations (Na, Rb) which have exposed various spectral changes related to the particular cation. Therefore, these results suggest a sort of equilibrium between two crystal forms of the

same oxidation state of $TCNQ^0$ one of which (C) is kinetically favorable and the other (A) thermodynamically favorable. Unfortunately, the presence of the reduced forms B and D for $TCNQ^-$ considered in eq. 2 cannot be confirmed in a similar manner as any such two forms exhibit an identical spectrum —at least under the working conditions used here.

Finally, one can expect the kinetics of the redox processes A and B to depend strongly on the particular cation in the background electrolyte as it must be incorporated into and released from the crystal forms; on the other hand, the electrolyte anion appears to be scarcely influential. Previous studies with M^+ alkali cations (see, for example, ref. 16) exposed a similar behavior for Na^+ and Rb^+, but a disparate one for Cs^+ by virtue of the different stoichiometry of its $TCNQ^-$ salt. Experiments in this direction currently under way in our laboratory may provide further useful knowledge with a view to obtaining perfectly structured thin films.

Conclusions

The electrochemical behavior of thin films of TCNQ on glassy carbon can be explained in the light of a mathematical model for layer-by-layer nucleation and growth. Oxidation of KTCNQ salt produces a crystal form of TCNQ that is kinetically favorable and evolves to another crystal form that is thermodynamically favorable. The transformation can be monitored *in situ* as the two forms exhibit disparate visible spectra. The formation of salt (reduction process) probably occurs similarly; however, the potential crystal forms involved

cannot be discriminated by spectroscopic means.

Acknowledgements

References

[1] Jaeger, C. D.; Bard, A. J. *Journal of the American Chemical Society* **1979**, *101*, 1690.

[2] Jaeger, C. D.; Bard, A. J. *Journal of the American Chemical Society* **1980**, *102*, 5435.

[3] Bartlett, P. N. *Journal of Electroanalytical Chemistry* **1991**, *300*, 175.

[4] Freund, M. S.; Brajtertoth, A.; Ward, M. D. *Journal of Electroanalytical Chemistry* **1990**, *289*, 127.

[5] Zhao, S.; Korell, U.; Cuccia, L.; Lennox, R. B. *Journal of Physical Chemistry* **1992**, *96*, 5641.

[6] Albery, W. J.; Bartlett, P. N.; Craston, D. H. *Journal of Electroanalytical Chemistry* **1985**, *194*, 223.

[7] Mounts, R. D.; Widlund, K.; Gunadi, H.; Pérez, J.; Pech, B.; Chambers, J. Q. *Journal of Electroanalytical Chemistry* **1992**, *340*, 227.

[8] Evans, C. D.; Chambers, J. Q. *Journal of the American Chemical Society*

1994, *116*, 11052.

[9] Evans, C. D.; Chambers, J. Q. *Chemistry of Materials* **1994**, *6*, 454.

[10] Scaboo, K. M.; Chambers, J. Q. *Electrochimica Acta* **1998**, *43*, 3257.

[11] Ruzicka, J.; Lamm, C. G. *Analytica Chimica Acta* **1971**, *54*, 1.

[12] Sharp, M. *Analytica Chimica Acta* **1976**, *85*, 17.

[13] Yamaguchi, S.; Potember, R. S. *Synthetic Metals* **1996**, *78*, 117.

[14] Yasuda, A.; Seto, J. *Journal of Electroanalytical Chemistry* **1988**, *247*, 193.

[15] Elkacemi, K.; Lamache, M. *Electrochimica Acta* **1986**, *31*, 1197.

[16] Bond, A. M.; Fletcher, S.; Symons, P. G. *Analyst* **1998**, *123*, 1891.

[17] Bond, A. M.; Fletcher, S.; Marken, F.; Shaw, S. J.; Symons, P. G. *Journal of the Chemical Society–Faraday Transactions* **1996**, *92*, 3925.

[18] Suárez, M. F.; Bond, A. M.; Compton, R. G. *Journal of Solid State Electrochemistry* **1999**, *4*, 24.

[19] Chambers, J. Q.; Scaboo, K.; Evans, C. D. *Journal of the Electrochemical Society* **1996**, *143*, 3039.

[20] Bond, A. M.; Fiedler, D. A. *Journal of the Electrochemical Society* **1997**, *144*, 1566.

[21] Oyama, M.; Webster, R. D.; Suárez, M.; Marken, F.; Compton, R. G.; Okazaki, S. *Journal of Physical Chemistry B* **1998**, *102*, 6588.

[22] Neufeld, A. K.; Madsen, I.; Bond, A. M.; Hogan, C. F. *Chemistry of Materials* **2003**, *15*, 3573.

[23] Sánchez-Maestre, M.; Rodríguez-Amaro, R.; Muñoz, E.; Ruiz, J. J.; Camacho, L. *Journal of Electroanalytical Chemistry* **1994**, 373, 31.

[24] Prieto, I.; Martín, M. T.; Muñoz, E.; Ruiz, J. J.; Camacho, L. *Journal of Electroanalytical Chemistry* **1997**, 424, 113.

[25] Demir, U; Shannon, C. *Langmuir* **1996**, 12, 6091.

[26] Hatchett, DW; Uibel, RH; Stevenson, KJ; Harris, JM; White, HS *Journal of the American Chemical Society* **1998**, 120, 1062.

[27] Fleischmann, M.; Thirst, H. R. In *Advances in Electrochemistry and Electrochemical Engineering*; Delahay, P. Ed.; Interscience: New York, 1963; Vol. 3.

[28] Harrison, J. A.; Thirst, H. R. In *Electroanalytical Chemistry*; Bard, A. J. Ed.; Marcel Dekker: New York, 1977; Vol. 5, p. 67.

[29] Budevski, E; Staikov, G.; Lorenz, W.J. *Electrochemical Phase Formation– An Introduction to the Initial Stages of Metal Deposition*; VCH, Weinheim, 1996.

[30] Armstromg, R.D.; Harrison, J.A., *Journal of the Electrochemical Society* **1980**, 116, 328.

[31] Bewick, A.; Fleischmann, M.; Thirsk, H.R.; *Transactions of the Faraday Society* **1962**, 58, 2200.

[32] Millán, J.I.; Ruiz, J.J.; Camacho, L.; Rodríguez-Amaro, R.; *Journal of the Electrochemical Society* **2002**, 149, E440.

[33] Ballester, L.; Gutiérrez, A.; Perpinan, M. F.; Azcondo, M. T. *Coordination Chemistry Reviews* **1999**, 192, 447.

5.2. STUDY OF THE OVERALL BEHAVIOUR OF THIN FILMS OF THE TCNQ$^{0/-}$ COUPLE ON GLASSY CARBON ELECTRODES IN THE PRESENCE OF CESIUM ION.

Abstract

The overall electrochemistry of 7,7,8,8-tetracyanoquinodimethane (TCNQ) thin films on glassy carbon electrodes in media containing Cs$^+$ ions is explained in the light of a layer-by-layer nucleation and growth model, and kinetic data for the processes involved is reported. Using *in situ* UV–visible spectroelectrochemistry allowed available mechanistic knowledge on such processes to be expanded and the presence of various intermediates in the redox reactions confirmed.

Introduction

7,7,8,8-Tetracyanoquinodimethane (TCNQ) has been widely studied on account of its ability to form radical and charge-transfer salts capable of acting as powerful electron acceptors towards the formation of organic conductors [1–12]. Much of the interest aroused by these materials has focused on their solid-state conductivity and related properties. Thus, solid TCNQ and its reduced salts have been used as single-crystal working electrodes [1,2,10]; mixed with carbon paste [13] or silicone oil [5]; coated on Nafion [14]; and attached to electrode surfaces by direct adhesion [7,15–19] or electrochemical deposition [20,21]. A necessary condition for this kind of compounds to have at least interesting conducting properties is that there is not a full charge transfer between the components of the salt. Then, mixed - valence salts are revealed as specially interenting compounds. By contrast, those with full charge transfer or monovalent are less attractive, due to its insulator nature [9].

Voltammetry and chronoamperometry studies [10,14-17,19] have shown that the electrochemical behaviour of the $[TCNQ]^{0/-}$ couple over a glassy carbon electrode surface in solutions of Group I cations is largely controlled by a nucleation–growth mechanism conforming to the following general equation:

$$xTCNQ_{(solid)} + yM^+_{(aq)} + ye^- \rightleftharpoons (M^+)_y(TCNQ^-)_y(TCNQ)_{x-}{}_{(solid)} \qquad (1)$$
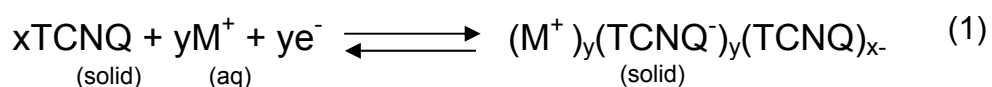
In the reduction reaction, the cation in solution is incorporated into the TCNQ film deposited over the electrode surface; in the oxidation reaction, the

cation is returned to the solution. As can be seen in eq 1, In this kind of processes, and depending on the cation present in solution, it is possible to obtain mixed–valence compounds, what makes this method an interesting way of obtaining TCNQ derivatives.

The kinetics of this process is rather complex and dependent on the amount of mass that is subjected to the redox cycle and the specific cation present in solution. Thus, all TCNQ in media containing Na^+, K^+ or Rb^+ ions is reduced in a single step [10,14–17,19]; bringing about the formation of monovalence compounds, MTCNQ. By contrast, TCNQ in a Cs^+ containing medium [15] is reduced in two well-defined steps that give two different compounds, Cs_2TCNQ_3 (mixed–valence) first, and CsTCNQ (monovalence) after the reduction of the remaining $TCNQ^0$. This versatility makes the study of TCNQ in Cs^+ media very attractive, not only for the different electrochemical behaviour of both compounds, but also for the enhancement in the understanding of this kind of systems. Although the reason for the disparate behaviour of TCNQ in Cs^+ respect to the other alkaline cations remains unclear, it must somehow be related to the fact that ingress–egress of the cation during the phase transformation is invariably accompanied by significant structural rearrangement dependent on the size of the particular cation.

In recent work [19], we explained the redox behaviour of the $[TCNQ]^{0/-}$ couple in KCl aqueous media in the light of a mechanism involving layer-by-layer nucleation and growth. Accurate fitting of experimental chronoamperometric curves allowed major kinetic data such as nucleation rate,

and layer shape and dimensions, among others, to be determined. This suggested the possibility of improving available knowledge about TCNQ organized films, which was the primary aim of this work. We believed the disparate behaviour of such films in Cs^+ and K^+ containing media would help us expand our current understanding of these processes and confirm the suitability of the 2D layer-by-layer model for their investigation and its potential use for controlling the behavior of this kind of organic films over the glassy carbon surface.

In addition, using *in situ* UV spectroelectrochemistry allowed us to obtain experimental evidence of the presence of intermediate compounds in these redox processes.

Experimental Section

Materials. 7,7,8,8-Tetracyanoquinodimethane over 98% pure and CsCl over 99.9% pure were supplied by Fluka and used as received. Acetone over 99.5% pure was supplied by Aldrich. All aqueous solutions were prepared in Milli-Q water.

Instrumentation. Chronoamperometric and voltammetric measurements were made on an AUTOLAB PGSTAT30 potentiostat/galvanostat equipped with SCAN-GEN and FRA2 modules in addition to an FI20 integration module that was controlled via GPES and FRA software. The working electrode was a glassy carbon disc with a surface area of 0.196 ± 0.005 cm^2, the auxiliary electrode Pt, and the reference electrode, to which all potentials given here are

referred, Ag|AgCl (3.0 M KCl).

For *in situ* spectroelectrochemical measurements, the AUTOLAB PGSTAT30 was coupled to an AVANTES SH2000 fibre-optic spectrophotometer equipped with a CCD that afforded recording of instantaneous spectra for the electrode coating at intervals as short as 1 s. The fibre-optic probe was fitted inside the electrochemical cell with normal incidence to the surface of the working electrode. The temperature was measured to within ± 0.1 ºC in all instances.

Procedure. TCNQ thin films were prepared by following a procedure described elsewhere [19]. To this end, TCNQ was dissolved to a 3.5 mM concentration in acetone and the resulting solution deposited onto the electrode surface. A mirror-like glassy carbon electrode surface was obtained by polishing with alumina in decreasing grain sizes from 1 µm to 0.05 µm. Then, the electrode was cleaned in an ultrasonic bath for 5 min. In these conditions the glassy carbon surface has optimal features both for electrochemical and spectroelectrochemical measurements. Once the electrode and solution were prepared, a micropipette was used to deposit a 10 µl drop ($3·10^{-8}$ mol) over the glassy carbon surface. The thin film of TCNQ thus obtained as the acetone evaporated was easily identified by its bright yellowish colour.

After the experimental current, j_{exp}, was measured in each chronoamperometric run, a similar j–t transient was also measured in a neighbouring potential region involving no electron transfer. This ensured that

only the double layer charging current, j_{dl}, would be measured. In this way, the resulting overall current, $j_T = j_{exp} - j_{dl}$, fitted the proposed theoretical model.

Results and discussion

Figure 1 shows a selected cyclic voltammogram for TCNQ in 0.5 M CsCl as obtained after 10 previous cycles over a glassy carbon electrode at a scan rate $v = 1$ mVs^{-1} at 5 ^{o}C. As can be seen in Figure 1a, the cathodic (forward) scan provided two single, narrow peaks (A$_1$ and A$_2$) and the anodic (reverse) scan another two (B$_1$ and B$_2$). Only A$_1$ and B$_1$ were observed if the voltammogram sweep was finished at −0.05V (Figure 1b), however, their position and charge coinciding with those of Figure 1a.
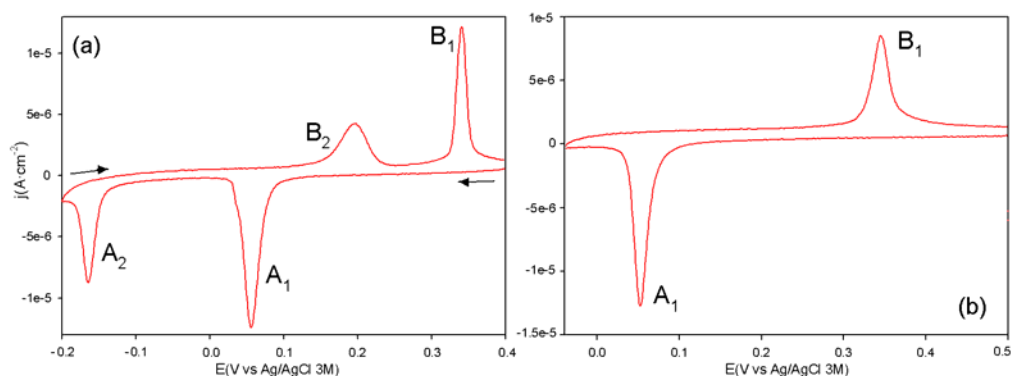

Figure 1. Steady-state cyclic voltammograms for TCNQ attached to a glassy carbon electrode in 0.5 M CsCl as obtained at a scan rate $v = 1$ mVs^{-1} at 20 ^{o}C after 10 cycles. Voltage range: (a) 0.4V to –0.2V, (b) 0.5V to –0.05V.

The area of peak A$_1$ was nearly twice that of A$_2$. In this process two third parts of TCNQ initially deposited were reduced. This is consistent with previous results of Bond et al. [15,16], so peaks A$_1$ and B$_1$ can be assigned to the following processes:

$$3TCNQ + 2Cs^+ \xrightleftharpoons[B_1]{A_1} Cs_2TCNQ \tag{2}$$
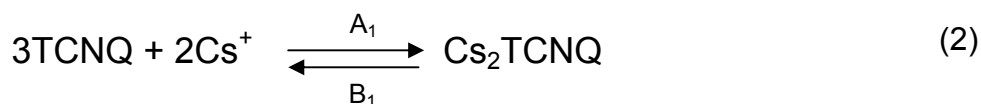
However, none of the previous studies addressed structure and composition after the processes behind peaks A_2 and B_2. Roughly one-third the amount of TCNQ initially deposited was reduced during A_2, which caused its complete reduction. Therefore, peaks A_2 and B_2 should be assigned to the following processes:

$$Cs_2TCNQ_3 + Cs^+ + e^- \xrightleftharpoons[B_2]{A_2} 3CsTCNQ \tag{3}$$
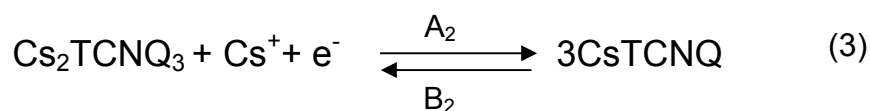
Raising the temperature favoured reduction (peaks A_1 and A_2 appeared at less negative potentials) at the expense of oxidation (peaks B_1 and B_2 were observed at more positive potentials). Also, it resulted in faster loss of the electrode coating, probably through dissolution of the cesium salts formed. A temperature of 5 °C was therefore adopted for subsequent work.

The variation of voltammetric peaks with the scan rate (v) provides a means for characterizing nucleation processes [22,23]. We found logarithmic plots of the peak currents (I_p) and peak widths at half-height (W) versus log v to be roughly linear for A_1 and B_1 (results not shown); the slopes of such plots are given in Table 1. We also investigated potential hysteresis [*viz.* the separation between peak potentials, $\Delta E_p = E_p(A_1) - E_p(B_1)$] and found a plot of log ΔE_p *versus* log v to be near-linear as well (see slopes in Table 1).

Table 1. Voltammetric data for the nucleation peaks A_1 and B_1 as obtained at $T = 5$ ºC and v values from 1 to 10 mVs^{-1}

Peak	$\partial\log I_p / \partial \log v$	$\partial\log W / \partial \log v$	$\partial\log \Delta E_p / \partial \log v$
A_1	0.78 ± 0.01	0.24 ± 0.02	
			0.09 ± 0.01
B_1	0.67 ± 0.05	0.13 ± 0.05	

The results obtained for log I_p and log W were similar to the theoretical values for 2D nucleation (≥ 0.6 and ≤ 0.4, respectively) [22,24,25], but the hysteresis curve could not be fitted. Therefore, the overall kinetics must be more complex than that for a 2D nucleation and growth process; however, the incorporation of additional molecules to growing nuclei, which was the rate-determining step for peaks A_1 and B_1, must essentially be the result of 2D nucleation processes.

Peaks B_1 and B_2 overlapped at higher rates, which precluded application of the previous characterization criteria.

Capacitance–potential curves provided additional information about the nature of the processes. The curves were run after 10 voltammetric cycles. Figure 2 (solid line) shows the experimental curve. In the cathodic scan, the capacitance exhibited a marked increase at potentials corresponding to the appearance of peak A_1, which led to the formation of a less compact compound than the initial TCNQ over the electrode. We should note that the capacitance in the anodic scan was lower than that obtained over the same potential range in the cathodic scan until peak B_2 appeared. This suggests that A_2 involves the

formation of a new species structurally more compact than that previously formed in A_1. After B_2, the capacitance slowly decreased until B_1 appeared and then exhibited a pronounced step.
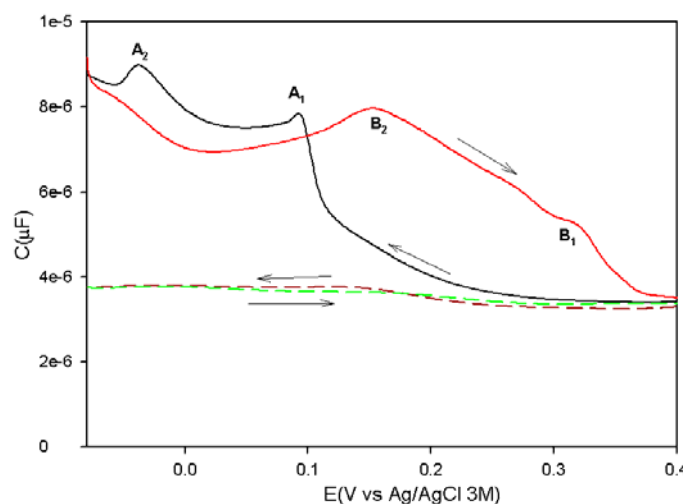

Figure 2. Plots of *C* as measured by using a potential pulse of 10 mV, a potential step of 1 mV and a frequency of 77 Hz *vs E*. The dashed line corresponds to a bare working electrode in 0.5 M CsCl and the solid line to a TCNQ thin film attached to a glassy carbon electrode in the same solution, after 10 voltammetric cycles. The initial double layer term has been suppressed.
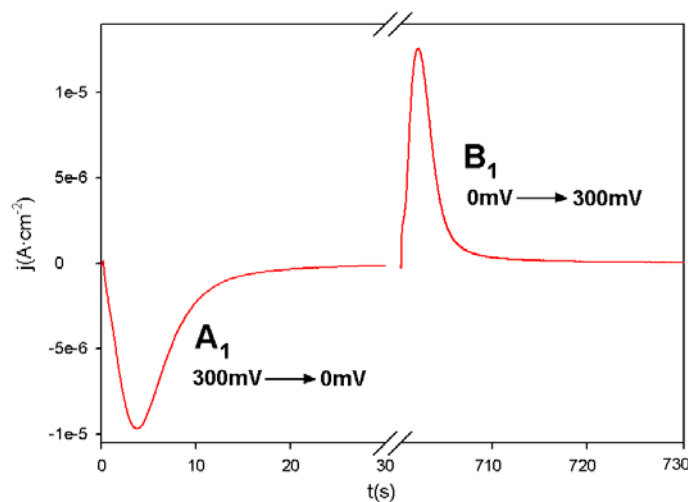

Figure 3. Selected experimental *j–t* curves for peaks A_1 and B_1 as obtained for an aqueous solution containing 0.5 M CsCl at 5 °C. The curves were experimentally obtained by applying a potential from 300 mV to 0 mV (peak A_1) or from 0 mV to 300 mV (peak B_1). Experimental data were acquired after application of 10 cycles of the potential range.

Chronoamperometry. Chronoamperometry is a very useful technique to obtain kinetic information about nucleation-growth processes [26,27]. We initially studied the processes corresponding to peaks A_1 and B_1. To this end, we obtained the experimental j–t curves of Figure 3 by using steps from 300 mV to 0 mV for reduction (peak A_1) and back from 0 mV to 300 mV (peak B_1) for oxidation.

No separate data for processes A_2 and B_2 could be obtained since the TCNQ thin film failed to exist long enough owing to the high solubility of the compound formed after B_2. In order to avoid its formation, we performed a series of chronoamperometric steps (Fig. 4) involving one for A_1, another for A_2 and a third for $B_1 + B_2$.
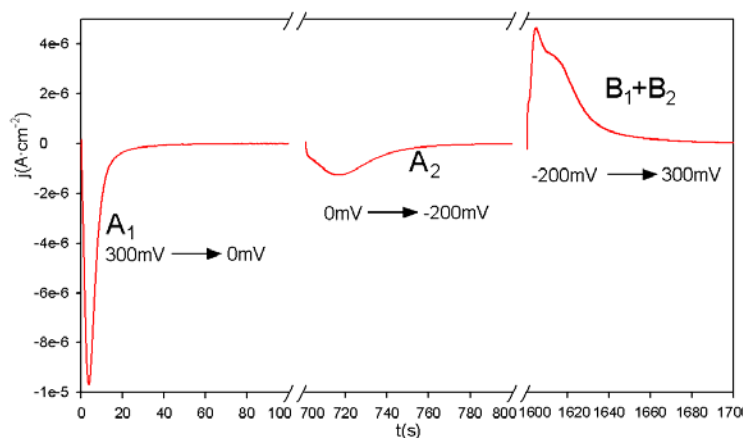

Figure 4. Selected experimental j–t curves for peaks A and B in an aqueous solution containing 0.5 M KCl at 5 °C. The curves were experimentally obtained by applying a potential from 300 mV to 0 mV (peak A_1), 0 mV to −200 mV (peak B_1), and −200mV to 300mV (peaks $B_1 + B_2$). Experimental data were acquired after application of 10 cycles of the potential range.

Taking into account that processes A_i and B_i were associated to an equivalent number of monolayers, we considered a Stranski–Krastanov mechanism [28], which combines 2D and 3D growth. With a small number of adlayers, the molecule and substrate interact with a high energy, so layer-by-layer growth (Frank-van der Merwe model) initially prevails. However, as the number of adlayers increases, so does lattice mismatch and, at some point, the FM model is no longer favourable and 3D growth takes over. This assumption is supported by previous results obtained in K^+ containing media [19].

The mathematical model used here is based on that of Armstrong and Harrison [29], who assumed 2D layer-by-layer growth. In their treatment, the current density for the first layer, j_0, is given by the Bewick–Fleischmann–Thirsk (BFT) equation [26,30]:

$$j_0 = n q_m \beta_0 t^{n-1} e^{-\beta_0 t^n} \quad (4)$$

and the current for successive layers by

$$j_i = n \beta_i \int_0^t (t-u)^{n-1} e^{-\beta_i (t-u)^n} j_{i-1}(u) du \qquad \text{for } i \geq 1 \tag{5}$$

where constants β_i are related to the growth rate for each layer —which can in theory differ between layers—, q_m is the charge involved in the nucleation process and n a constant dependent on its nature which equals 2 for instantaneous nucleation and 3 for progressive nucleation.

The overall current density,

$$j_T = j_0 + \sum j_i \tag{6}$$

can be calculated by numerical desk calculator integration.

As in a system described elsewhere [31], the current density dropped to

zero owing to the limited amount of substance covering the electrode, which can be ascribed to incomplete coverage by some monolayers in each step (reduction or oxidation) of the redox cycle. Thus, the nuclei formed in previous chronoamperometric cycles can be roughly approximated to pyramids or cones. The drop in current density has been simulated by using the following mathematical expression [31]:

$$\theta_i = \frac{1}{1 + e^{a(i-m)}} \tag{7}$$

where *a* and *m* are two empirical parameters, *l* is the number of full monolayers (therefore, if $i < l$, j_i will be given by eq 5 and, if $i \geq l$, j_i will be given by the product of eq 5 and θ_i as defined in eq 7).

In applying this mathematical model to our system we assumed the word "layer" to refer to a crystal zone or region of a given thickness where transport would not be a rate-determining step [19]. Thus, based on the charge for the first layer (*ca.* 283 μC cm^{-2} as intermediate value, Table 2), the unit cell volume per molecule of Cs_2TCNQ_3 reported by Bond et al. [14], 277 Å^3, on the assumption of a monoclinic space group for TCNQ and its salt Cs_2TCNQ_3, we estimated the thickness of the layer to be *ca*. 49 Å. Although this value should be taken cautiously because it relies on some approximations, each crystal zone or layer would in fact consist of about 5–6 monoclinic cells, which is consistent with the definition of thin layer used in the proposed mathematical model.

Figure 5 shows selected experimental (solid) curves corresponding to voltammetric peak A_1 as obtained after variable numbers of cycles —the overall charge decreased with cycling— following suppression of the initial charging current density term, j_{dl}.

In the initial portion ($t{\to}0$), all log (j-j_{dl}) vs log t curves in Figure 5 were roughly linear and had a unity slope (data not shown). This suggests that nucleation was essentially two-dimensional and instantaneous (n = 2) at the beginning.
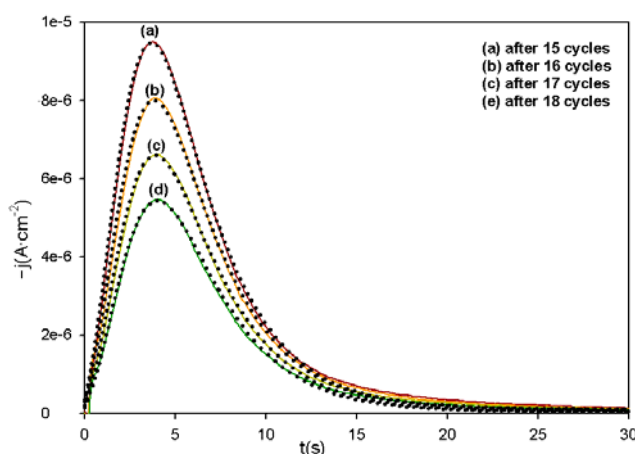

Figure 5. Selected experimental (solid lines) j–t curves for process A_1 as obtained after a variable number of voltammetric cycles and suppression of the initial charging current term, j_{dl}. E_{in} was 300 mV and E_f 0 mV. The dotted lines represent the simulated results provided by the model based on eq 6.

The theoretical, simulated curves provided by the proposed mathematical model (dotted lines in Figure 5), and the experimental curves (solidd lines), are quite consistent. Table 2 shows their figures of merit. It should be noted that the growth rate for the first layer (β_0) was lower than that for all subsequent layers (β_i), and that only the first layer (l = 1) was full.

Table 2. Figures of merit of the mathematical fitting of the experimental curves for process A_1 in Fig. 5 to the proposed model, based on eq 6. For all curves, $l = 1$, $a = 0.3$, $m = 2.2$ and $ß_1 = ß_2 = \ldots = ß_i$

After cycle	q_m /μC cm^{-2}	$ß_0 \times 10^2$ /s^{-1}	$ß_i \times 10^2$ /s^{-1}
10	352	9	137
11	306	8.5	132
12	258	8	132
13	216	7.5	131

The curves for peak B_1, not shown, were very similar and their figures of merit almost identical except for $ß_i$, which were approximately 2.5 times higher than the values for A_1. These results are similar to those obtained in K^+ containing media [19], which suggests that the nature of the redox processes A_1 and B_1 is not affected by the size of the cation.

The experimental curves for A_2 exhibited two major differences in relation to A_1 and B_1. Thus, the current density obtained by suppressing the double layer term was not zero at the beginning; also, after reduction was finished, j decreased slowly until a zero current was reached. One possible explanation for these differences is that, after a stable enough crystalline compound such as Cs_2TCNQ_3 was obtained, ingress of further Cs^+ cations in the structure was hindered by the large radius of Cs^+ ion and electrostatic repulsions between the new Cs^+ ions and those present in the crystal. At an appropriate potential (peak A_2), however, Cs^+ cation was able to enter the layer at the time the remaining $TCNQ^0$ was reduced, thus causing the crystal rearrangement needed for the film to house additional Cs^+ cations in order to produce CsTCNQ. This assumption is supported by reported data [32] which have confirmed that

CsTCNQ and Cs_2TCNQ_3 differ in crystal structure; therefore, any phase conversion between them must have an associated phase transition within the framework of a structural change in the crystal network.

This phenomenon generates additional, non-faradaic resistance to the incorporation of new Cs^+. If the thin layer over the electrode is assumed to be equivalent to a capacitor, then this "non-faradaic term", j_{nf} , can be expressed as follows:

$$j_{nf} = \frac{\Delta E}{R \cdot S} \cdot e^{-\frac{t}{R \cdot C}} = k_3 \cdot e^{-(k_4 \cdot t)}$$
(8)

where ΔE , R, C and S are the potential, resistance, capacitance and surface area of the electrode, respectively. Therefore, the overall theoretical current density is

$$j_T = j_0 + \sum j_i + j_{nf}$$
(9)

As can be seen in Figure 6, the sum of the theoretical faradaic, $\sum j_i$, and non faradaic, j_{nf}, terms is consistent with the experimental curves. The non-faradaic term decreases as the thin films dissolves (Table 3).
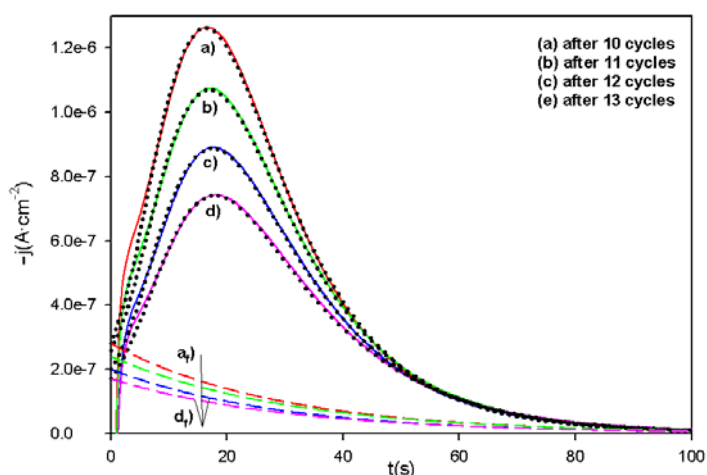
Figure 6. Selected experimental (solid line) j–t curves for process A$_2$ as obtained after a variable number of voltammetric cycles and suppression of the initial charging current term, j_{dl}. E_{in} = 0 mV and E_f = −200 mV. The dotted lines represent the simulated results provided by the model based on eq 8 and the dashed lines the non-faradaic term.

Table 3. Figures of merit of the mathematical fitting of the experimental curves for process A$_2$ in Figure 6 to the proposed model, based on eq 9. For all curves, l = 1, a = 0.3, m = 2.2, ß$_1$ = ß$_2$ = … = ß$_i$ and k$_4$ = 0.03 s^{-1}

After cycle	q_m /μC cm^{-2}	ß$_0$ ×10^3 /s^{-1}	ß$_i$ × 10^2 /s^{-1}	k$_3$ /s^{-1}
10	167.2	4.2	75.6	1.16
11	146.71	3.9	70.2	1.044
12	127	3.83	61.3	0.812
13	112.5	3.6	50.4	0.7

Process B$_2$ could not be examined individually, so it had to be studied in parallel with B$_1$. The resulting curve for these processes is shown in Figure 7. It was a complex curve exhibiting two well-defined maxima after suppression of the double layer term. Based on the voltammograms of Figure 1a, we can assume the two processes to occur separately, and also that the first maximum corresponds to B$_2$ and the second to B$_1$.

Similarly to the simulation of B_1, we also considered the non-faradaic phenomenon in simulating the experimental curves. The most appropriate way of simulating the two processes was by using the mathematical model of "consecutive phase transitions" [33], based on which A_2 would only occur after the solid over the electrode had undergone B_2. The above-described layer-by-layer model can explain single processes but has never to date been used to explain two consecutive layer-by-layer processes. Thus, although it is an approximation, we assumed the two processes to be independent of each other, which provided the results of Figures 7 and 8, and Table 4.

Figure 7. Selected experimental (solid line) *j–t* curves for the overall oxidation process as obtained after 11 voltammetric cycles and suppression of the initial charging current term, j_{dl}. E_{in} = −200 mV and E_f = 300 mV. The dashed lines (a) and (b) represent the simulated results for B_1 and B_2, respectively, provided by the model based on eq 8; (c) represents the non-faradaic term; and the dotted line represents the simulated curve obtained by combining (a), (b) and (c).
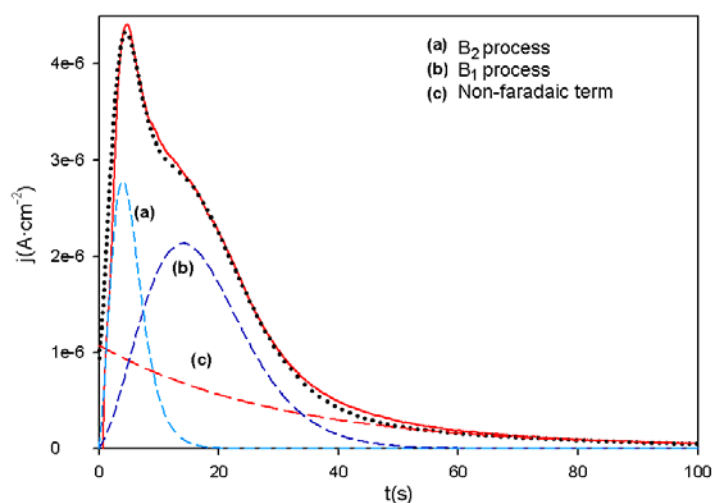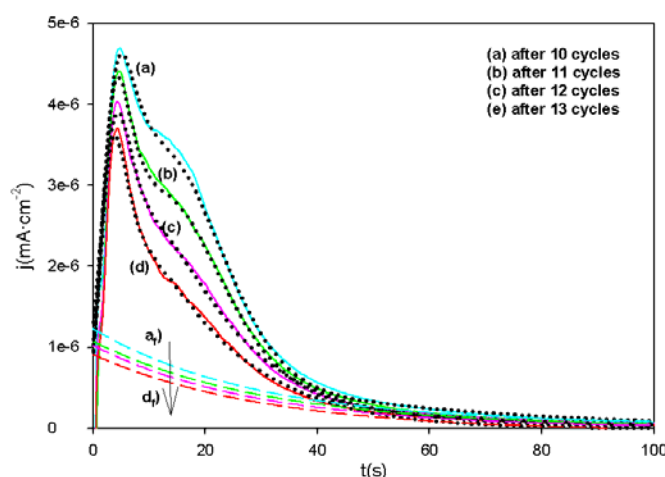
Figure 8. Selected experimental (solid line) j–t curves for the overall oxidation process as obtained after a variable number of voltammetric cycles and suppression of the initial charging current term, j_{dl}. E_{in} = −200 mV and E_f = 300 mV. The dotted lines represent the simulated results provided by the model based on eq 8 and the dashed lines the non-faradaic term.

Table 4. Figures of merit of the mathematical fitting of the experimental curves of Figure 8 to the proposed model, based on eq 8. For all curves, l = 1, a = 0.3, m = 2.2, $ß_1 = ß_2 = \ldots = ß_i$ and k_4 = 0.03 s^{-1}

After cycle	$q_m(B_2)$ /µC cm^{-2}	$q_m(B_1)$ /µC cm^{-2}	$ß_0 (B_2)$ ×10^3/s^{-1}	$ß_0 (B_1)$ x10^2 /s^{-1}	$ß_i (B_2)$ /s^{-1}	$ß_i (B_1)$ /s^{-1}	k_3 /s^{-1}
10	130.45	325	6.2	4	1.55	0.96	1.31
11	114.71	293.71	7.2	5.4	2.16	0.297	1.2
12	99.29	248.24	7.3	8	2.19	0.112	1.13
13	86.18	194.7	9	9.2	2.7	0.073	0.9

The effect of the step overpotential for processes A$_1$, A$_2$ and B$_1$ was also examined. Figure 9 shows selected experimental j–t curves for peak A$_1$ as obtained from E_{in} = 300 mV to variable E_f values, following suppression of the initial charging current density term, j_{dl}. As can be seen from the simulated curves provided by the proposed model, fitting to the experimental data

worsened with increasing step overpotential. Thus, consistency between predicted data (solid lines) and their experimental counterparts was very good at E_f values of 20, 0, and −10mV (Table 5); on the other hand, fitting of the data obtained at E_f values of 50 and 40mV was incomplete.
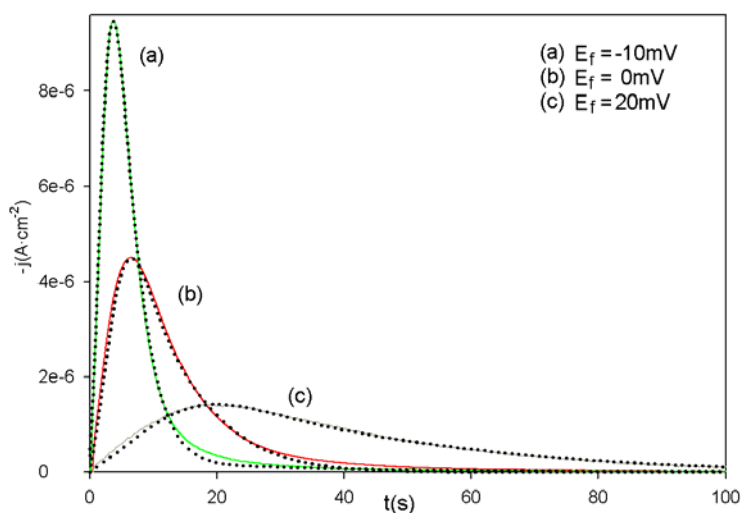

Figure 9. Selected experimental (solid lines) j–t curves for the reduction process A_1 as obtained at variable E_f values following suppression of the initial charging current density term, j_{dl}. E_{in} was 300 mV. The dotted lines represent the simulated results provided by the model based on eq 6.

Table 5. Figures of merit of the mathematical fitting of selected experimental curves of Figure 9 to the proposed model, based on eq 6. For all curves, $l = 1$, $a = 0.3$, $m = 2.2$, $\text{ß}_1 = \text{ß}_2 = \ldots = \text{ß}_i$.

E_f /mV	$\text{ß}_0 \times 10^3$ /s^{-1}	$\text{ß}_i / \text{ß}_0$
20mV	3.5	3.9
0mV	30	7.2
−10mV	90	15.1

The results obtained for the reduction process A_2 (Figure 10) were essentially the same except for the non-faradaic contribution, which increased with increasing overpotential.
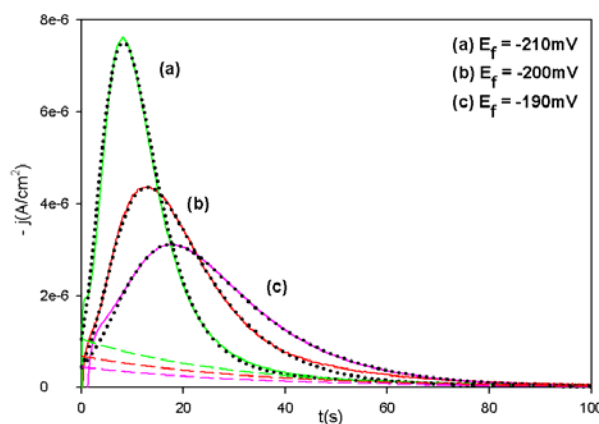

Figure 10. Selected experimental (solid lines) j–t curves for the reduction process A_2 as obtained at variable E_f values following suppression of the initial charging current density term, j_{dl}. E_{in} was 0 mV. The dotted lines represent the simulated results provided by the model based on eq 9 and the dashed lines the non-faradaic term.

Table 6. Figures of merit of the mathematical fitting of selected experimental curves of Figure 10 to the proposed model, based on eq 9. For all curves, $l = 1$, $a = 0.3$, $m = 2.2$, $ß_1 = ß_2 = … = ß_i$ and $k_4 = 0.03$ s^{-1}.

E_f /mV	$ß_0 \times 10^3$ /s^{-1}	$ß_i/ß_0$	k_3 / s^{-1}
−190mV	3.7	15	0.35
−200mV	7	18	0.55
−210mV	17	23	1.05

The same routine was used with peak B_1 (results not shown), which behaved almost identically with A_1. The sole difference between the two was in the ratio $ß_i/ß_0$, which was roughly 2.5 times higher for B_1.

It was impossible to study the influence of this parameter on the combined peak $B_1 + B_2$. Although all curves were similar in shape, the relationship between $\beta_0 (B_2)$ and $\beta_0 (B_1)$ was not reproducible enough, so no well-defined pattern for the variation of this process with the overpotential could be established.

Based on these results, the mechanism remains virtually unchanged over a wide overpotential range and the sole effect of the overpotential is accelerating the process at increased values for all layers. However, we should note that the β_i/β_0 ratio, Tables 5 and 6, was dependent on the final step potential, which departs from the behaviour observed in potassium ion.[19] Moreover, the β_i/β_0 ratio increased with increasing overpotential, which can be ascribed to more favourable formation of the successive layers rather than to the formation of the first layer. This is consistent with the assumption of the formation of compact crystal structures hindering ingress–egress of the cation, the effect increases as the size of the cation becomes higher.

Applied overpotentials outside the previous range altered the nucleation process; thus, above a given overpotential threshold, the nucleation–growth mechanism changed by effect of an altered ion mobility which was not fast enough; this precluded application of our mathematical model. Therefore, the proposed model only holds over a specific overpotential range for each peak.

Spectroelectrochemistry. Spectroelectrochemistry has been proved as a useful tool with a view to obtaining evidence for the presence of intermediate species involved in the above-described mechanism [19].

The baseline for each chronoamperometric cycle was the spectrum obtained at time zero (E = 300 mV), once electrochemical recordings were reproducible as shown in Figures 5 and 6. Interestingly, all studied spectral series exhibited a constant baseline; therefore, spectral changes during each chronoamperometric cycle cannot be ascribed to a change in path length caused by the varying conditions during the tests.

As in previous studies on KTCNQ [19] and other alkaline TCNQ salts (unpublished results), in which no crystal rearrangement occurs it could not be observed any spectral changes in A_1, therefore the detection of the presence of any intermediates in the reduction of TCNQ to Cs_2TCNQ_3 was precluded. However, the reduction of Cs_2TCNQ_3 to CsTCNQ (process A_2), that is accompanied by a crystal rearrangement, provided a spectrum such as that of Figure 11, with two well-defined peaks at 305 nm and 415 nm in addition to a band from 600 to 900 nm typical of $TCNQ^-$ [34]. The entire spectrum grew to a maximum at $\tau \approx 100$ s. Then, the spectrum gradually decreased and eventually disappeared at $\tau = 600$ s. This spectral series exposed the presence of two different solid structures which must be related to two different crystal forms of CsTCNQ, one (I) being kinetically favourable and the other (T) thermodynamically favourable. No similar spectral change was previously observed in other alkaline salts, which undergo phase transitions involving no

crystalline rearrangement in the way process A_1 does. However, the phase transition occurring in A_2 can be expected to induce a marked spectral change such as that described above.
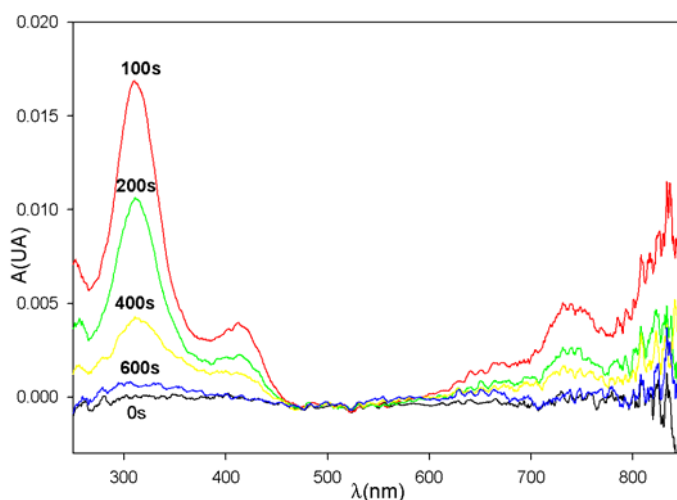

Figure 11. Variation of the spectra for process A_2 as recorded at a potential of −200 mV for variable lengths of time, τ.

The oxidation of CsTCNQ to $TCNQ^0$ (B_1+B_2 process) exhibited the spectrum shown in Figure 12. The spectrum contained a peak at about 400 nm typical of neutral TCNQ [33] which must be related to the presence of a new solid structure of $TCNQ^0$ [19] The absorbance of the peak increased with time up to a maximum at $\tau \geq 100$ s and then slowly decreased up to $\tau \geq 700$ s, after which the peak disappeared.

As the 400 nm peak disappeared, a new band was observed between 450 and 600 nm which disappeared 700 s after the 300 mV step was applied.
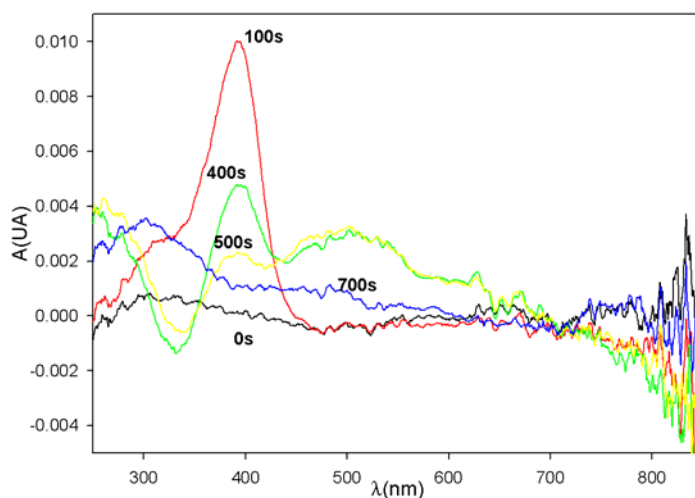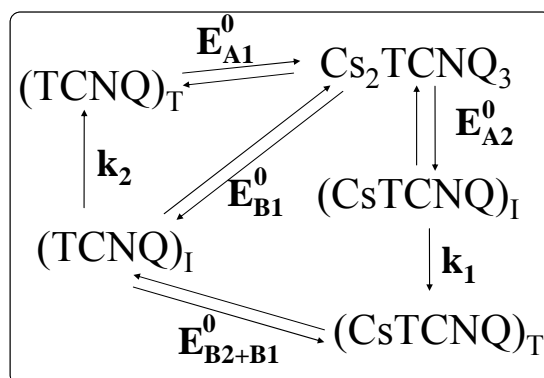
Figure 12. Variation of the spectra for the process giving peak B_1 + B_2 as recorded at a potential of 300 mV for a variable length of time τ.

The oxidation of Cs_2TCNQ_3 to $TCNQ^0$ (peak B_1) exhibited a very similar behaviour to that giving peak B_1 + B_2 (results not shown). However, the band in the 450–600 nm region was absent here, so the shape of the spectrum and its variation with time were almost identical with those for the oxidation of $TCNQ^-$ in K^+ containing media [19]. These results are quite consistent with the potential presence of two crystal forms of TCNQ, one kinetically favourable (I) and the other thermodynamically favourable (T), similarly as in K^+ containing media. This latter assumption might be supported on the basis of the nucleation-growth model with a phase miscibility gap [35] due to the large separation between $E_{p,ox}$ and $E_{p,red}$.

Based on the previous results, we can propose the following overall redox mechanism for TCNQ in Cs^+ containing media:

$$(TCNQ)_T \xrightarrow{E^0_{A1}} Cs_2TCNQ_3 \xrightarrow{E^0_{A2}} (CsTCNQ)_I$$

$$k_2 \quad E^0_{B1} \quad k_1$$

$$(TCNQ)_I \xrightarrow{E^0_{B2+B1}} (CsTCNQ)_T$$

where the species in brackets and subscripted with the letter I are intermediate species and subscript T denotes stable species.

Conclusions

A recently developed mathematical model for layer-by-layer nucleation and growth was found to explain the behaviour of thin films of various TCNQ cesium salts over glassy carbon electrodes. Also, kinetic information about the electrochemical formation and destruction of the CsTCNQ salt is for the first time reported.

One can obtain two different types of stable structures for Cs-TCNQ salts, namely: CsTCNQ and Cs_2TCNQ_3. The phase transition leading from CsTCNQ to Cs_2TCNQ_3 involves crystal rearrangement as confirmed by experimental electrochemical and spectroelectrochemical evidence. The rearrangement produces a bulky Cs^+ cation that hinders ingress–egress of crystalline structures, thereby posing additional, non-faradaic resistance.

Acknowledgements

References

[1] Jaeger, C. D.; Bard, A. J. *Journal of the American Chemical Society* **1979**, *101*, 1690.

[2] Jaeger, C. D.; Bard, A. J. *Journal of the American Chemical Society* **1980**, *102*, 5435.

[3] Bartlett, P. N. *Journal of Electroanalytical Chemistry* **1991**, *300*, 175.

[4] Freund, M. S.; Brajtertoth, A.; Ward, M. D. *Journal of Electroanalytical Chemistry* **1990**, *289*, 127.

[5] Zhao, S.; Korell, U.; Cuccia, L.; Lennox, R. B. *Journal of Physical Chemistry* **1992**, *96*, 5641.

[6] Albery, W. J.; Bartlett, P. N.; Craston, D. H. *Journal of Electroanalytical Chemistry* **1985**, *194*, 223.

[7] Mounts, R. D.; Widlund, K.; Gunadi, H.; Pérez, J.; Pech, B.; Chambers, J. Q. *Journal of Electroanalytical Chemistry* **1992**, *340*, 227.

[8] Evans, C. D.; Chambers, J. Q. *Journal of the American Chemical Society* **1994**, *116*, 11052.

[9] Torrance, J.B.; Scott, B.A.; Kaufman, F.B. *Solid State Communications*,

1975, *17*, 1369.

[10] Scaboo, K. M.; Chambers, J. Q. *Electrochimica Acta* **1998**, *43*, 3257.

[11] Yamaguchi, S.; Potember, R. S. *Synthetic Metals* **1996**, *78*, 117.

[12] Yasuda, A.; Seto, J. *Journal of Electroanalytical Chemistry* **1988**, *247*, 193.

[13] Elkacemi, K.; Lamache, M. *Electrochimica Acta* **1986**, *31*, 1197.

[14] Bond, A. M.; Fletcher, S.; Symons, P. G. *Analyst* **1998**, *123*, 1891.

[15] Bond, A. M.; Fletcher, S.; Marken, F.; Shaw, S. J.; Symons, P. G. *Journal of the Chemical Society–Faraday Transactions* **1996**, *92*, 3925.

[16] Suárez, M. F.; Bond, A. M.; Compton, R. G. *Journal of Solid State Electrochemistry* **1999**, *4*, 24.

[17] Chambers, J. Q.; Scaboo, K.; Evans, C. D. *Journal of the Electrochemical Society* **1996**, *143*, 3039.

[18] Bond, A. M.; Fiedler, D. A. *Journal of the Electrochemical Society* **1997**, *144*, 1566.

[19] Gómez, L.; Rodríguez-Amaro, R.; *Langmuir* **2006**, 22, 7431.

[20] Oyama, M.; Webster, R. D.; Suárez, M.; Marken, F.; Compton, R. G.; Okazaki, S. *Journal of Physical Chemistry B* **1998**, *102*, 6588.

[21] Neufeld, A. K.; Madsen, I.; Bond, A. M.; Hogan, C. F. *Chemistry of Materials* **2003**, *15*, 3573.

[22] Sánchez-Maestre, M.; Rodríguez-Amaro, R.; Muñoz, E.; Ruiz, J. J.; Camacho, L. *Journal of Electroanalytical Chemistry* **1994**, 373, 31.

[23] Prieto, I.; Martín, M. T.; Muñoz, E.; Ruiz, J. J.; Camacho, L. *Journal of Electroanalytical Chemistry* **1997**, 424, 113.

[24] Demir, U; Shannon, C. *Langmuir* **1996**, 12, 6091.

[25] Hatchett, DW; Uibel, RH; Stevenson, KJ; Harris, JM; White, HS *Journal of the American Chemical Society* **1998**, 120, 1062.

[26] Fleischmann, M.; Thirst, H. R. In *Advances in Electrochemistry and Electrochemical Engineering*; Delahay, P. Ed.; Interscience: New York, 1963; Vol. 3.

[27] Harrison, J. A.; Thirst, H. R. In *Electroanalytical Chemistry*; Bard, A. J. Ed.; Marcel Dekker: New York, 1977; Vol. 5, p. 67.

[28] Budevski, E; Staikov, G.; Lorenz, W.J. *Electrochemical Phase Formation–An Introduction to the Initial Stages of Metal Deposition*; VCH, Weinheim, 1996.

[29] Armstromg, R.D.; Harrison, J.A., *Journal of the Electrochemical Society* **1980**, 116, 328.

[30] Bewick, A.; Fleischmann, M.; Thirsk, H.R.; *Transactions of the Faraday Society* **1962**, 58, 2200.

[31] Millán, J.I.; Ruiz, J.J.; Camacho, L.; Rodríguez-Amaro, R.; *Journal of the Electrochemical Society* **2002**, 149, E440.

[32] Shirotani, I; Sakai, N, *Journal of Solid State chemistry* **1976**, 18, 17.

[33] Gómez, L.; Ruiz, J.J.; Camacho, L.; Rodríguez-Amaro, R.; *Langmuir* **2005**, 21, 369.

[34] Ballester, L.; Gutiérrez, A.; Perpinan, M. F.; Azcondo, M. T. *Coordination Chemistry Reviews* **1999**, 192, 447.

[35] Scholz, F.; Lovric, M.; Stojek, Z. *Journal of Solid State Electrochemistry* **1997**, 1, 134.

5.3. NUCLEATION AND GROWTH OF THIN FILMS OF THE ORGANIC CONDUCTOR TTF-IODIDE OVER GLASSY CARBON. ELECTROCHEMICAL AND SPECTROELECTROCHEMICAL STUDY.

Abstract

Based on the electrochemical and spectroelectrochemical behavior of thin films of TTF over a glassy carbon electrode in iodide media, a new, more complete mechanism for the electrode processes involved is proposed. The voltammetric and chronoamperometric results for the films can be explained in the light of a recently developed nucleation–growth model involving a layer-by-layer mechanism. Also, their *in situ* UV–Vis spectral data expand available knowledge about the overall mechanism and the nature of the compound formed over the glassy carbon electrode.

Introduction

TTF (Tetrathiafulvalene, 2,2′-bi-1,3-dithiole) is a powerful π-electron donor capable of forming radical and charge-transfer complex compounds. Its cation radical salts have been extensively studied over the past three decades as the organic conducting and superconducting compounds they form [1–4]. It has been shown that the conductivity of the organic salt is significant only when charge transfer between the salt components is partial [1,2]. In the search for partial charge transfer compounds, the high electric conductivity of mixed valence TTF–halide salts —which approaches that of TTF–TCNQ in some cases[4]— has aroused much interest [1–3] and promoted the development of new methods for their synthesis. These TTF-halide salts have usually been obtained by using complex methods [1]; more recently, however, Bond et al. [3] have found that the voltammetric and chronoamperometric properties of these conducting materials provide an attractive method for their synthesis based on the following reaction:

$$TTF^0 + 0.7X^- \leftrightarrow (TTF^+)_{0.7}(TTF^0)_{0.3}(X^-)_{0.7} + 0.7e^- \qquad (1)$$
$$\text{(solid)} \qquad \text{(aq)} \qquad\qquad \text{(solid)}$$
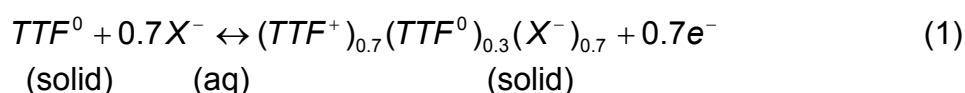
In the oxidation reaction, a solid TTF film is partially oxidized in a single step[3] involving the ingress of the halide ion present in solution into the TTF to form a solid film consisting of a mixed-valence compound, $TTF^0(TTF^+)_{0.7}(X^-)_{0.7}$; in the reduction, the anion returns to the bulk solution. Similarly as reported in previous studies on TCNQ [5–7], the electrochemistry of the $[TTF]^{0/+}$ couple over a glassy carbon electrode surface in an halide anion solution is largely controlled by a nucleation–growth mechanism [3]. However, no mechanistic

approach has to date provided a proper explanation for its electrochemical behavior.

In this paper, we provide an accurate explanation for the chronoamperometric behavior of the $[TTF]^{0/+}$ couple in KI aqueous media. Fitting experimental curves to the proposed theoretical model allowed us to obtain major kinetic information such as nucleation rate or layer shape and dimensions. Also, *in situ* UV spectroelectrochemistry provided experimental evidence for the presence of intermediate compounds in the redox processes involved.

These results allow one to improve the available knowledge about TTF organized films with a view to preparing new organic conducting materials by exploiting such special electrochemical properties to obtain thin films of this organic conductor over glassy carbon surfaces.

Experimental Section

Tetrathiafulvalene (Fluka) over 98%, KI (Fluka) over 99.9% and Methanol over 98% pure (Aldrich) were used as received. All aqueous solutions were prepared in Milli-Q water.

An AUTOLAB PGSTAT30 potentiostat was used for electrochemical measurements. A 0.785 ± 0.005 cm^2 glassy carbon disc was used as working electrode in addition to a Pt auxiliary electrode and an Ag|AgCl (3.0 M KCl) reference electrode.

In order to obtain appropriate TTF thin films, a 10 µl drop of a 3.5 mM solution in methanol was deposited onto a glassy carbon electrode the surface of which was made mirror-like by polishing with alumina in decreasing grain sizes from 1 µm to 0.05 µm, followed by sonication for 5 min. Immediately, the methanol evaporated and a visible yellow layer appeared over the electrode surface.

A fiber optic probe inserted in the electrochemical cell with normal incidence to the working electrode allowed in situ spectroelectrochemical measurements with an AVANTES SH2000 spectrophotometer synchronized with the potentiostat in order to ensure that all spectral measurements would accurately correspond to a specific point in the time and on the potential scale. The good reflectivity and negligible absorption of UV–Vis light by the mirror-like surface of glassy carbon has facilitated the use of this electrode as a substrate for spectroelectrochemical measurements. The temperature was measured to within ± 0.1 ºC in all instances.

Results and discussion

Electrochemistry

The cyclic voltammograms obtained after 10 cycles at 1 mVs^{-1} for TTF over glassy carbon in KI media (Figure 1a) were stable and exhibited two narrow peaks of similar charge one corresponding to the anodic process (A) and the other to the cathodic process (B). During the first voltammetric cycles at low rates, the solid passed from a heterogeneous state to a crystal state, which reflected in growing symmetry in the voltammetric peaks. In order to confirm the stoichiometry proposed in eq 1 by Bond *et al.* [3], an accurately known amount of TTF was deposited over the electrode surface. Although the peaks obtained in the first cycle were asymmetric, the charge for peak A in the first voltammogram was highly reproducible between runs and corresponded to the oxidation of 70 ± 2% the amount of TTF deposited over the electrode.

The potential of both peaks, A and B, was shifted to more negative values as the temperature was raised; however, the temperature had no influence on their separation. We thus chose 5 ºC for use in subsequent tests in order to minimize dissolution of the compounds covering the electrode. Although increasing the electrolyte concentration resulted in sharper peaks for both processes, the separation between their peak potentials remained virtually unchanged. A concentration of 0.5 M was thus adopted in order to ensure that the peaks would be as narrow as possible [3].

Nucleation processes can be finely characterized via the variation of the peak current (I_P), width at half-height (W) and hysteresis ($\Delta E_p = E_{p,A1} - E_{p,B1}$) of

voltammetric peaks with the scan rate (v) [8,9]. As can be seen in Table 1, logarithmic plots of these parameters against log v were all linear, and the slopes for log I_P and log W fitted to their theoretical values [6,8,10] (≥ 0.6 and ≤ 0.4, respectively); on the other hand, the hysteresis also varied linearly, but departed from its theoretical counterpart (≤ 0.4). Therefore, as with TCNQ, [7] the underlying process is more complex than a 2D nucleation–growth process; however, the rate-determining step, which is the ingress of additional molecules to growing nuclei, must be the result of 2D nucleation.
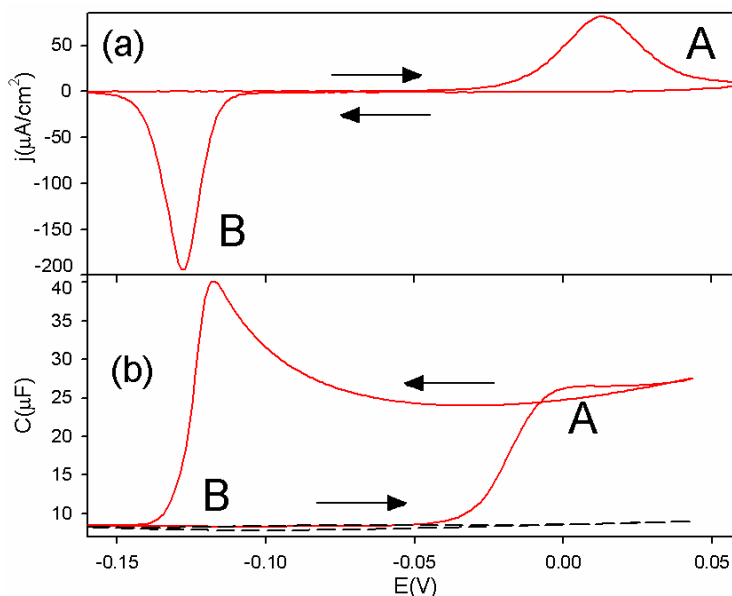

Figure 1. (a) Steady-state cyclic voltammogram obtained after 10 cycles at 1 mVs^{-1}. (b) Capacitance vs E plot for a TTF thin film over glassy carbon (solid) and the bare glassy carbon (dashed) in 0.5 M KI, both obtained after 10 cycles. Conditions for the capacitance measurements: potential pulse, 10 mV; potential step, 1 mV; frequency, 77 Hz.

Table 1. Voltammetric data for peaks A and B as obtained at T = 5 ºC and v values from 1 to 10 mVs^{-1}

Peak	∂log I_p/∂ log v	∂log W/∂ log v	∂log $\Delta E_p/\partial$ log v
A	0.87 ± 0.05	0.24 ± 0.01	0.16 ± 0.01
B	0.65 ± 0.02	0.31 ± 0.03	

After 10 voltammetric cycles, the experimental curve (Figure 1b) exhibited a constant capacitance up to the onset of peak A, where it rose markedly; this suggests the formation of a less compact compound (TTFI$_{0.7}$) than the starting TTF^0. Subsequently, the capacitance increased slowly during the cathodic scan, leading to a less compact TTFI$_{0.7}$ form with time. In peak B, a dramatic drop in capacitance led to the initial state and the capacitance levelled off until a new oxidation cycle started.

Chronoamperometry is a very useful tool for obtaining kinetic information about nucleation–growth processes [11,12]. In what follows, all chronoamperometric curves shown exclude the double layer contribution (j_{dl}), which was avoided by introducing a similar j–t transient in a potential region adjacent to that of the experimental curves, but involving no electron transfer. The resulting overall current, $j_T = j_{exp} – j_{dl}$, was suitable for a possible fitting to the proposed theoretical model, as can be seen in Figure 2 for the oxidation (A) and the reduction (B) curves. We introduced two chronoamperometric jumps in each cycle: one of 600 s at 40 mV for process A and another of 800 s at 40 mV for process B. This ensured reproducibility in the curves and attainment of equilibrium before each chronoamperometric jump.
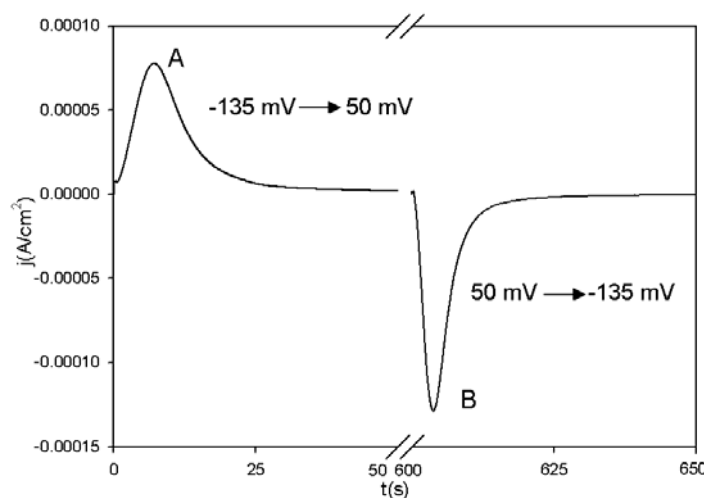
Figure 2. Experimental *j–t* curves for peaks A and B after 10 voltammetric cycles in aqueous 0.5 M KI. The applied potentials are stated beside the curves.

Since processes A and B are associated to a large number of equivalent monolayers of surface-attached material, nucleation and growth must occur via a 2D layer-by-layer (Frank–van der Merwe, FM, model) [13] or 3D (Volver–Weber, VW, model) [14] mechanisms, as, whether a given system grows in two or three dimensions will depend on how strong the interaction between the substrate and deposited molecules is [15].

The shape of the voltammetric peaks was found to depend strongly on the amount of TTF deposited onto the electrode. With fairly small amounts, the peaks were well-defined (see Figure 1a); as the amount adsorbed increased, however, the peaks were increasingly ill-defined and resembled those typical of an amorphous precipitate. This indicates a change in mechanism or the combined action of several and is potentially consistent with a Stranski–Krastanov (2D + 3D) mechanism [16], which combines 2D and 3D growth. As a result of the high interaction energy involved, layer-by-layer growth (FM model)

will occur at the initial stage of deposition. However, if the size of the molecule and substrate are significantly different, lattice mismatch will increase with increasing number of adlayers. At some point, the FM model will no longer be favorable and 3D growth starts.

Based on the model of Armstrong and Harrison [17] for 2D layer-by-layer nucleation and growth and on the Bewick–Fleischmann–Thirsk (BFT) equation for a single 2D layer [18,19], the current density for the whole process, j_T, can be given expressed as [6,7]:

$$j_T = j_0 + \sum j_i \theta_i = nq_m \beta_0 t^{n-1} e^{-\beta_0 t^n} + \sum \theta_i \cdot n\beta_i \int_0^t (t-u)^{n-1} e^{-\beta_i (t-u)^n} j_{i-1}(u) du \quad (2)$$

where constants β_i relate to the growth rate for each layer, q_m is the charge for the first layer ($i = 0$), and n equals to 2 for instantaneous nucleation and 3 for progressive nucleation.

However, the application of the mathematical model to the studied system warrants some comment [7]. Thus, strictly speaking, the BFT model is only applicable provided the rate-determining step involves the exchange of ad-molecules at the periphery of expanding sites. Although this is to be expected for the first monolayer, it need not for multiple layers, across which ions must be transferred during redox processes. One possible explanation is that, only when the film is thick enough, can the transfer process be the rate-determining step; until then (initial layers), the model will be quite applicable. Also, the word "layer" should be used in its broadest sense here. Thus, the charge for the first layer (*ca.* 100 µC cm^{-2} as intermediate value) must in fact correspond to a "crystal zone" exhibiting a uniform behaviour (*i.e.*, "layer" should be used to

designate a crystal zone or region of a given thickness). Moreover, based on the TTFI$_{0.7}$ (monoclinic) cell volume reported by Scott et al. [1], 916 Å^3, each layer must consist of 5–6 monoclinic cells and thus be a thin layer indeed.
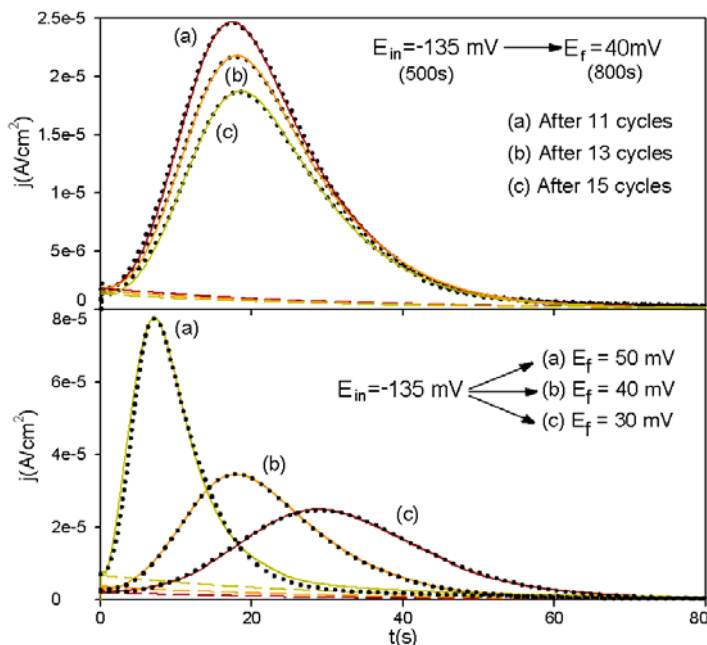

Figure 3. Experimental (solid) and simulated (dotted) j–t curves for process A as obtained after a variable number of voltammetric cycles (top) at variable step overpotentials (bottom). E_{in} and E_f are shown beside each curve. The dashed lines represent the nonfaradaic term. For all simulations, $l = 1$, $a = 0.45$, $m = 3$ and k$_4$ = 0.035 s^{-1} based on eq 5.

Owing to the limited amount of substance covering the electrode, the surface of each layer was always equal to or less than that of the inner layer; therefore, the solid formed after several redox processes was assumed to be roughly pyramidal or conical in shape, which was simulated by multiplying j_i by $θ_i$ for each layer [20]:

$$\theta_i = \frac{1}{1 + e^{a(i-m)}} \tag{3}$$

where a and m are two empirical parameters. If l (an adjustable parameter) is taken to be the number of full layers, then, for $i < l$, the layer will be full and $\theta_i = 1$.

As shown in Figure 3, j was not zero at the onset of the experimental curves; also, even after the oxidation process had finished, it decreased slowly to zero. This phenomenon has previously been reported [6], and a plausible explanation for this result is that TTF^0 is more compact than $TTF_{0.7}$, which is consistent with the capacitance measurements. Therefore, TTF^0 must be somewhat more resistant to the ingress of bulky I^- ions and an additional, nonfaradic term, j_{nf}, which decreases as the film dissolves should be considered. If the thin film over the electrode is likened to a capacitor, then j_{nf} can be expressed as:

$$j_{nf} = \frac{\Delta E}{R \cdot S} \cdot e^{-\frac{t}{R \cdot C}} = k_3 \cdot e^{-k_4 \cdot t} \tag{4}$$

where ΔE, R, C and S are the potential, resistance, capacitance and surface area of the electrode, respectively. Therefore, the overall theoretical current density will be

$$j_T = j_0 + \sum \theta_i j_i + j_{nf} \tag{5}$$

The simulated and experimental curves for process A (Figure 3) are quite consistent with progressive nucleation ($n = 3$). In all subsequent simulations, we assumed that only the first layer would be full ($l = 1$), and that parameters a, m and k_4 would be constant and equal to 0.45, 3 and 0.035 s^{-1}, respectively. The only variable factors used were q_m, k_3 and β_i; the last, however, was identical for

all layers except the first ($\beta_1 = \beta_2 = \ldots = \beta_i \neq \beta_0$), which invariably exhibited a smaller value.

Overall (see Table 2), q_m and k_3 decreased by about 5% through dissolution of the coating between successive cycles; therefore, the contribution of j_{nf} to j_T remained unchanged. β_i also remained virtually constant, but β_0 decreased slightly (0.5%) in each cycle.

Table 2. Figures of merit of the mathematical fitting of the experimental curves for process A in Figure 3 (top) to the proposed model, based on eq 5. For all curves, $l = 1$, $a = 0.45$, $m = 3$, $\beta_1 = \beta_2 = \ldots = \beta$, $k_4 = 0.035$ s^{-1}.

After cycle	q_m /μC cm^{-2}	$\beta_0 \times 10^4$ /s^{-1}	$\beta_i \times 10^2$ /s^{-1}	k_3 / μAcm^{-2}
11	145	2.8	2.1	1
13	131	2.5	2.2	0.94
15	114	2.3	2.3	0.89

Regarding the effect of the step overpotential (Figure 3, bottom), we can conclude that the mechanism remained virtually unchanged over a wide range of overpotential and that the main effect of this variable was accelerating β_0 and β_i —up to three orders of magnitude in β_0, and less markedly so for β_i as shown in Table 3. The contribution of j_{nf} also increased with increasing overpotential. Although there was a clear influence, we could establish no definite relationship between the applied overpotential and each parameter used in the simulations (k_3, β_0 and β_i).

Table 3. Figures of merit of the mathematical fitting of selected experimental curves of Figure 3 (bottom) to the proposed model, based on eq 5. For all curves, $l = 1$, $a = 0.45$, $m = 3$, $\beta_1 = \beta_2 = \ldots = \beta_i$, $k_4 = 0.035$ s^{-1}

E_f /mV	$\beta_0 \times 10^5$ /s^{-1}	$\beta_i \times 10^2$ /s^{-1}	β_i/β_0	k_3 / µAcm^{-2}
50	430	15.9	37	2.5
40	25	2.2	87	1
30	5.7	1.7	300	0.7

Process B (results not shown) only exhibited two salient differences from A. First, the β_i/β_0 ratio remained constant at 30 ± 10 throughout; by contrast, in process A the ratio increased with increasing overpotential and number of cycles. Second, the absence of a nonfaradic contribution is consistent with the increased compaction of the solids —if ingress of I$^-$ was hindered in process A, then I$^-$ egress should have been favored in the opposite process, B.

At low and moderate overpotentials, fitting (Figure 3) was acceptable. Consistency between predicted and experimental data was very good for both processes (Tables 2 and 3). However, our mathematical model cannot be applied above a threshold overpotential of *ca*. −145 mV (data not shown) — probably as a result of some change in ion mobility, which was not high enough—, so the underlying mechanism for the process was altered.

Spectroelectrochemistry

Spectroelectrochemistry proved high useful with a view to extracting valuable mechanistic information from this type of process. UV–Vis light was transferred to the electrode surface by a fiber optic probe. The light was focused sheer over the TTF thin film, passed over it and reflected back to the fiber optic probe, which carried it to the detector. The resulting spectral changes were exclusively due to the absorption of light by the thin film and this led us to use absorbance measurements as the most suitable form of spectral data for the intended purpose.

Recordings were made once the chronoamperometric curves became reproducible (see Figure 3, top). Spectra were recorded at 10 s intervals immediately after the chronoamperometric jumps for processes A and B; this allowed any significant changes in the film over the electrode to be detected. Under these conditions, the spectral baselines (*i.e.* the spectrum a $\tau = 0$) were identical in successive cycles, which suggests that the solid over the electrode underwent no substantial reorganization between cycles. Therefore, the spectral changes observed during the redox cycle can only be ascribed to changes in electronic configuration of the molecules forming the film. This also avoided inaccuracies in the measurements such as those arising from relating spectral changes to changes in path length or composition of the supporting electrolyte between runs.

Figure 4 shows the spectra for processes A and B. Correct interpretation of the resulting peaks was facilitated by reference to the spectra previously

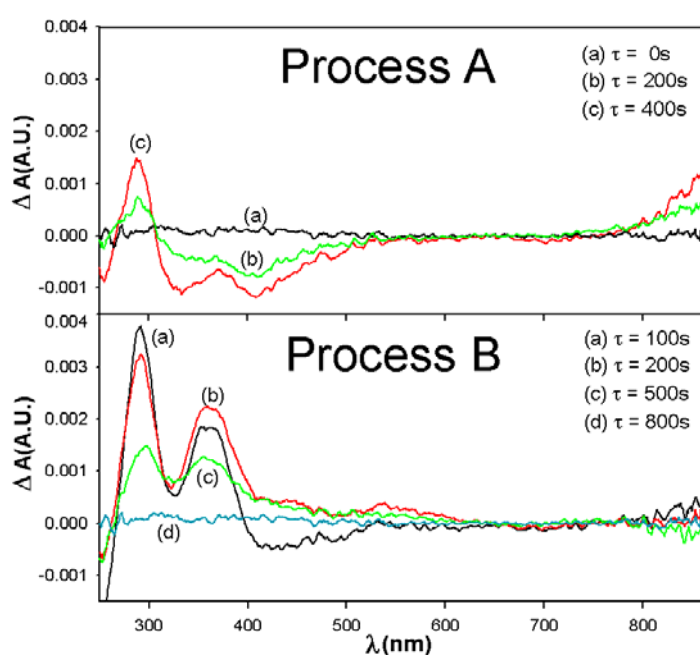reported by Torrance *et al.*[2] for TTF^0 and $TTFI_{0.7}$, which are shown in Fig. 5.

Figure 4. Variation of the spectra at 50mV (process A) and -135mV (process B) as recorded for variable lengths of time, τ.
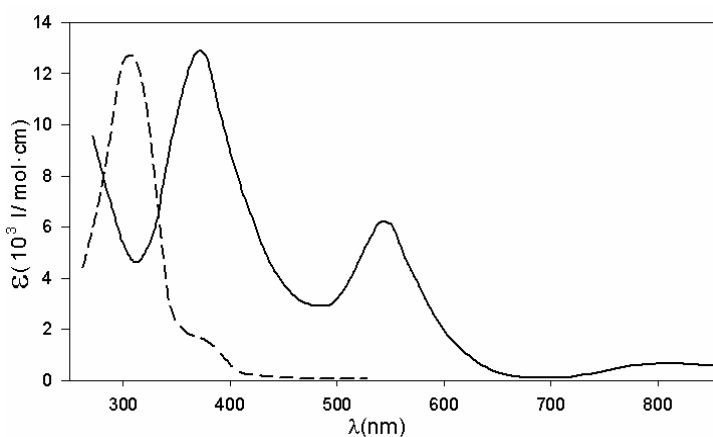

Figure 5. Spectra reported by Torrance *et al.*[2] for TTF^0 in acetonitrile (dashed line) and solid $TTFI_{0.7}$ in KBr powder (solid) as multiplied by a factor of 4.

The broad band between 250 and 500 nm (Figure 4, top), typical of TTF^0 in solution [2], decreased as the species TTF^0 was oxidized. The presence of two well-defined peaks at 300 nm and 375 confirms that of intramolecular

interactions[2] in TTF$^+$, which typically fall in the region from 250 to 600 nm. Although the peak at 375 nm had previously been observed,[2] that at 300 nm had not; also, the absence of peaks at 560 nm is suggestive of differences between this salt and that previously obtained [2].

Regarding intermolecular interactions, the band above 780 nm corresponds to a charge transfer (CT) process between two neighbouring TTF$^+$ molecules [2]. The entire spectrum grew to a maximum at $\tau \approx 400$ s and then levelled off, which precluded detection of any intermediates.

In the reduction reaction (Figure 4, bottom), however, the spectrum progressed for 800 s and then returned to its initial state (before oxidation). As regards individual signals, the CT band disappeared at *ca.* 30 s; on the other hand, the TTF^0 band rose slowly between 250 and 500 nm. All intramolecular interaction bands increased up to a maximum at $\tau = 100$ s; also, a shoulder appeared at 560 nm probably corresponding to the above-mentioned missing intramolecular band for process A. All these bands decreased beyond $\tau = 100$ s and eventually disappeared after 800 s.

These results are consistent with the potential presence of two TTF^0 crystal forms, as expected for a nucleation–growth model with a phase miscibility gap [21] due to the large separation between $E_{p,ox}$ and $E_{p,red}$. In this respect, we can hypothesize the presence of two crystalline forms, namely: a thermodynamically favorable form designated $(TTF)_T$ and a kinetically favorable one designated $(TTF)_I$ and exhibiting enhanced intramolecular interactions relative to $TTFI_{0.7}$.

Based on the above-described results, the following overall redox mechanism is proposed:

$$(TTF)_I \xrightarrow{k_B} (TTF)_T \xrightarrow{E_A^0} TTF\text{-}X_{0.7} \xrightarrow{E_B^0} (TTF)_I$$
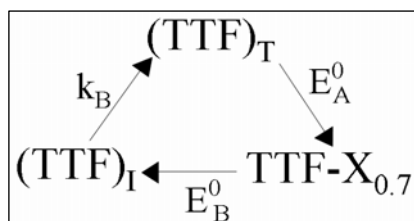
Conclusions

With a view to acquiring a deeper knowledge of the electrochemistry of TTF thin films over glassy carbon in halide media, the proposed electrochemical method for preparing $TTFI_{0.7}$ provides a very simple, reproducible, attractive tool for obtaining thin films of potentially conducting organic compounds. Although preliminary results for other halides have exposed a similar behavior, the outcome of the electrochemical process is clearly influenced by the different anions present. In any case, the TTF–Iodide system has proved as a useful model for starting studies on this type of system.

Also, the recently developed layer-by-layer nucleation–growth mathematical model has for the first time allowed the kinetics and electrochemistry of TTF thin films to be explained. In contrast to the instantaneous nucleation mechanism ($n = 2$) previously established for TCNQ [6,7], the TTF–Iodide system nucleates and grows via a progressive mechanism ($n = 3$). This confirms the flexibility of the model in that it can predict the behavior of various types of thin films formed by nucleation and growth over

electrodes.

Finally, *in situ* spectroelectrochemistry has improved available knowledge about the nature of the compounds formed, and provided evidence for the presence of at least one intermediate during the reduction process.

Acknowledgements

References:

[1] Scott, B. A.; LaPlaca, S. J.; Torrance, J.B.; Silverman, B. D.; Weber B. *J. Am. Chem. Soc.* **1977**, 99, 6631.

[2] Torrance, J. B.; Scott, B. A.; Weber, B.; Kaufman, F. B.; Seiden, P. E. *Phys. Rev. B* **1979**, 19, 730.

[3] Shaw, S. J.; Marken, F.; Bond, A. M. *Electroanalysis* **1996**, 8, 732

[4] Jaeger, C. D.; Bard, A. J. *J. Am. Chem. Soc.* **1979**, 101, 1690.

[5] Bond, A. M.; Fletcher, S.; Marken, F.; Shaw, S. J.; Symons, P. G. *J. Chem. Soc., Faraday Trans.* **1996**, *92*, 3925.

[6] Gómez L.; Rodríguez-Amaro R. *Langmuir* **2008**, *24*, 11246

[7] Gómez, L.; Rodríguez-Amaro, R. *Langmuir* **2006,** 22, 7431.

[8] Sánchez-Maestre, M.; Rodríguez-Amaro, R.; Muñoz, E.; Ruiz, J. J.;

Camacho, L. *J. Electroanal. Chem.* **1994**, 373, 31.

[9] Prieto, I.; Martín, M. T.; Muñoz, E.; Ruiz, J. J.; Camacho, L. *J. Electroanal. Chem.* **1997**, 424, 113.

[10] Hatchett, D.W.; Uibel, R.H.; Stevenson, K.J.; Harris, J.M.; White, H.S. *J. Am. Chem. Soc.* **1998**, 120, 1062.

[11] Demir, U.; Shannon, C. *Langmuir* **1996**, 12, 6091.

[12] Harrison, J. A.; Thirst, H. R. *In Electroanalytical Chemistry*, Bard, A. J., Vol. 5, Marcel Dekker, New York, **1977**.

[13] Frank, F.C.; Van der Merwe, J.H. *Proc. Roy. Soc* **1949** A198, 205

[14] Volmer, M. ; Weber, A. *Z. Physik. Chem.* **1926,** 119, 277

[15] Milchev, A.; *Electrocrystallization.* Kluwer Academic Publishers, Massachusetts. **2002**

[16] Budevski, E.; Staikov, G.; Lorenz, W.J. *Electrochemical Phase Formation– An Introduction to the Initial Stages of Metal Deposition*, VCH, Weinheim, **1996**.

[17] Armstromg, R.D.; Harrison, J. A. *J. Electrochem. Soc.* **1980**, 116, 328.

[18] Fleischmann, M.; Thirst, H. R. In *Advances in Electrochemistry and Electrochemical Engineering*; Delahay, P. Ed.; Interscience: New York, **1963**; Vol. 3.

[19] Bewick, A.; Fleischmann, M.; Thirsk, H.R. *Trans. Faraday Soc.* **1962**, 58, 2200.

[20] Millán, J. I.; Ruiz J. J.; Camacho L.; Rodríguez-Amaro, R. *J. Electrochem. Soc.* **2002**; 149, E440.

[21] Scholz, F.; Lovric, M.; Stojek, Z. *J. Solid State Electrochem.* **1997**, 1, 134.

CAPÍTULO VII
CONCLUSIONES

Del trabajo de investigación realizado en la presente se pueden obtener una serie de conclusiones:

1. En medio ácido con yoduro como contraion, el comportamiento electroquímico de la bipiridina es fuertemente dependiente de la temperatura. El primer proceso de reducción de la bipiridina ($BpyH_2^{2+}/BpyH_2^{\cdot+}$) sobre electrodo de mercurio, por debajo de 18 ºC, da lugar a tres pares de picos voltamétricos estrechos (A_1/A_2, B_1/B_2 y D_1/D_2), debidos a la formación/destrucción de fases condensadas. Estos procesos presentan comportamiento virtualmente independiente, al ocurrir la formación de la segunda fase mucho más lentamente que la primera.

2. El comportamiento cronoamperométrico del proceso A_1 para la bipiridina es explicado mediante el modelo matemático de desorción – nucleación recientemente desarrollado, el cual supone un mecanismo que lleva consigo una reorientación molecular. Esta reorientación tiene una fuerte contribución en la formación de la fase condensada, lo que se traduce en un incremento en la fuerza con la que el anión es adsorbido a la superficie electródica.

3. Una fase nueva y más compacta que la formada en A_1 tiene lugar en el proceso B_1 para la bipiridina, la cual puede ser explicada mediante el modelo clásico BFT de nucleación y crecimiento instantáneos.

4. Por encima de 18 ºC, los procesos A_1/A_2 y B_1/B_2 se presentan como un solo par de picos voltamétricos, C_1/C_2. Este comportamiento es adecuadamente

explicado mediante el nuevo modelo matemático de "transiciones de fase 2D consecutivas". Dicho modelo considera que el crecimiento de la segunda fase, B_1, sólo puede ocurrir en zonas en las que la primera, A_1, ya ha sido previamente formada (*i.e.* para fases 2D consecutivas). La cinética de cada uno de los procesos implicados en esta sucesión de transiciones de fase es similar a la de cada una de ellas por separado, a temperaturas menores de 18ºC.

5.   El comportamiento electroquímico del etilviológeno sobre electrodo de mercurio da como resultado la formación de una fase 2D condensada previa a la reducción del EtV^{2+} por difusión. Tal fase es aparentemente formada por una estructura organizada (un par iónico entre el EtV^{2+} y el anión I^- en una proporción 1:1). La formación de la fase, que se ve reflejada en los picos voltametricos A_1 y B_2, es un simple proceso capacitativo de nucleación instantánea, el cual probablemente lleva consigo la desorción de las moléculas inicialmente adsorbidas sobre el electrodo. Por otro lado, su destrucción, que se muestra en los picos A_2 y B_1, es un proceso más complejo, cuya cinética es complicada por incluir varios fenómenos.

6. El modelo matemático recientemente desarrollado de nucleación y crecimiento capa a capa ha permitido, por primera vez, explicar la cinética y la electroquímica de las películas delgadas de compuestos orgánicos potencialmente útiles para la formación de sales orgánicas conductoras. Este modelo se muestra flexible, pudiéndose aplicar tanto a sistemas con nucleación y crecimiento instantáneo (TCNQ en medio alcalino), como progresivo (TTF en medio haluro).

7. Se ha conseguido implantar la técnica de espectroelectroquímica UV-Vis *in situ* para el estudio de los procesos de nucleación y crecimiento sobre el electrodo de carbón vitrificado. De esta manera, se consiguen obtener evidencias experimentales de la presencia de intermedios de reacción en estos procesos.

8. En la oxidación de KTCNQ para obtener TCNQ se ha conseguido detectar la presencia de un intermedio cinéticamente favorable $(TCNQ)^I$ para dar lugar a una forma cristalina termodinámicamente favorable,$(TCNQ)^0$. La formación de la sal (proceso de reducción) ocurre, probablemente, de manera similar; sin embargo, este cambio no puede demostrarse mediante espectroelectroquímica.

9. En la reducción de TCNQ para dar sales con el catión Cs^+ se observan dos tipos diferentes de estructuras estables de sales de TCNQ: CsTCNQ y Cs_2TCNQ_3. La transición de fase ocurrida que produce CsTCNQ a partir de Cs_2TCNQ_3 está acompañada de una reestructuración cristalina. Esta reestructuración se puede confirmar experimentalmente a través de la espectroelectroquímica UV-Vis, la cual también da evidencias de la presencia de un intermedio de reacción. Este reordenamiento cristalino está acompañado de un impedimento a la entrada-salida de los iones reflejado en una resistencia no faradaica. El proceso de oxidación de ambas sales llevan consigo la formación de al menos un intermedio de reacción, así como una nueva reestructuración del cristal para volver al estado inicial.

10. El estudio espectroelectroquímico de la reducción del $TTFI_{0.7}$ a TTF sobre

carbón vitrificado muestra la presencia de, al menos, un intermedio de reacción cinéticamente favorable, que evoluciona posteriormente hacia una forma cristalina termodinámicamente favorable.

11. El procedimiento propuesto para la preparación de $TTFI_{0.7}$ proporciona una herramienta simple, reproducible y atractiva para la obtención de compuestos orgánicos potencialmente conductores.

12. Aunque los resultados preliminares para otros haluros presentes en disolución dan resultados similares, éste proceso está claramente influenciado por la naturaleza del anión. En cualquier caso, el sistema yoduro-TTF se muestra como un modelo adecuado como punto de partida para el estudio de este tipo de sistemas.